

Dynamic Domains in Strongly Driven Ferromagnetic Films

A dissertation accepted by
the Department of Physics of
Darmstadt University of Technology

for the degree of
Doktor der Naturwissenschaften
(Dr. rer. nat.)

by

Katherine Mayes, B.A., M.Sc.
from Dublin

Main Supervisor: Prof. Dr. H. Sauer
Second Supervisor: Prof. Dr. B. Drossel

Date of submission: 4th December 2002
Date of examination: 27th January 2003

Darmstadt 2002

D17

Contents

1	Introduction	4
2	The Landau-Lifshitz Equation	8
2.1	Effective Magnetic Field	9
2.2	Rotating Reference Frame	10
I	Numerical Simulation	12
3	Notes on Computation and Representation	13
4	Numerical Dynamic Domains	17
4.1	Homogeneous State	17
4.2	Stripes and Bubbles	18
4.3	Wall Structure	20
4.4	Bistability and Hysteresis	23
4.5	Nature of Critical Thresholds	24
II	Analytical Investigation	27
5	Homogeneous Solution	28
5.1	Calculation of Homogeneous Solution	28
5.2	Linear Stability Analysis	30
6	Domain Features far from the Wall	37
6.1	Magnetization far from the Wall	37
6.2	Linear Stability Analysis	41
7	Dynamic Domain Wall Structure	49
7.1	Planar Domain Walls without Damping	50
7.2	Effect of Wall Curvature	52
7.3	Approximate Wall Solution for $\Gamma \ll 1$	56

8	A Stability Criterion for Dynamic Domains	59
8.1	Comparison with Undriven System	59
8.2	Linearized Equations of Motion	60
8.3	First Order Solution	66
8.4	Second Order Solution	67
8.5	Secular Condition	69
9	Comparison of Results	73
9.1	Homogeneous Solution	73
9.2	Domain Features far from the Wall	74
9.3	Wall Structure	75
10	Conclusions	78
A	Numerical Linear Stability Analysis	82
B	Evaluation of Integrals	85
C	Bloch Wall Dynamics	86
D	Eigenstates of \mathcal{D} and T	89
E	Higher Order Secular Condition	92
	Bibliography	95

Chapter 1

Introduction

Regular patterns and structures, both equilibrium and nonequilibrium, are found in a wide variety of physical and chemical systems, systems as diverse as type I superconductors, ferrofluids confined between two glass plates, fluids undergoing a Rayleigh-Bénard instability, and domains in ferromagnetic garnet films [SeAn]. These macroscopic patterns have periods on widely different length scales (from $10\mu\text{m}$ for superconductor and magnetic garnet patterns, to 1cm for ferrofluids and convective patterns), but all exhibit a simple regularity that, in the two-dimensional examples mentioned above, includes stripes and bubbles.

The last of the four examples above, magnetic systems, provides a classic case of equilibrium pattern formation. The concept of *static domains*, macroscopic regions of uniform magnetization within a magnetic material, was introduced by Weiss already at the beginning of the last century to explain why such materials can be in a state of zero (or very weak) total magnetization while having a non-zero local magnetization. This hypothesis has been since confirmed by experiment many times over, by optical methods exploiting the Faraday or Kerr effects, or by the Bitter-pattern method where suspensions of magnetic particles are spread over the surface of the probe [MaSl]. The theory is also well understood. Magnetic domains are a consequence of the competition between two effects: the short-range exchange interaction acts to promote the homogeneous state, while the long-range dipolar interaction destabilizes it. The balance of the exchange and anisotropy effects means that the transition from one domain to the next is not abrupt, typically taking place over several hundred lattice constants, and the theory of domain walls is also well-developed [Hube]. Depending on the orientation of the magnetization as it passes from one domain to the next, domain walls are called Bloch walls (the magnetization rotates in the plane of the wall) or Néel walls (the magnetization rotates in the direction normal to the wall)¹.

¹The name “Bloch wall” can also be used in a wider sense to describe all walls between static domains, regardless of their orientation.

In the 1970's, encouraged by technical advances in digital data storage, interest in domain structure in magnetic garnet films grew [Wige84]. For many years, vertical Bloch lines (where differently orientated domain walls meet) were expected to be of great technological importance and this interest also pushed forward advances in the theory of static domains [Slon]. Of particular interest are the dynamic properties of 180° walls (where the magnetization rotates from \mathbf{e}_z in one domain to $-\mathbf{e}_z$ in the next) when a *static* magnetic field is applied in the \mathbf{e}_z direction parallel to the easy axis of a ferromagnet [Thie, ScWa]. The review by de Leeuw and coworkers provides a good overview of this area [deLe]. Application of the static theory to two and three dimensions has also been investigated [Kose, IvSh].

Ferromagnetic systems *driven by external magnetic fields* have also been under investigation for many years [Damo]. Early work by Suhl already showed that there is a threshold where the uniform state becomes unstable to homogeneous driving fields [Suhl]. Driven magnetic systems are a physicist's playground for spatio-temporal nonequilibrium effects [Wige94]. Now when the difference between the pump field and its critical value is small (the weakly nonlinear case), the pattern formation in such a system can be described by amplitude equations. The case where the driving field is perpendicular to the external static magnetic field (transverse pump) has been investigated in detail [MaSa, Völg], as has the parallel pump case, particularly for the case of films [Rieg].

However, when the probe is *strongly* driven, such perturbative procedures break down. One-dimensional numerical simulations have predicted *dynamic domains* for model including a transversely rotating field [Elme]. Dynamic domains are stable solutions to the equations of motion. In the reference frame rotating with the driving field they exhibit a stationary domain structure, like that known from static domains, yet in the lab frame their position is stationary while the magnetization within the domains rotates at different angles (see the sketch in Figure 1.1). Plefka also obtained dynamic domains in one dimension by numerical simulation and was able to explain characteristic elements of the structure analytically [Plef95].

Using a simple model, Flesch predicted theoretically dynamic domains in one dimension [Fles]. Crucially, this model neglected the effect of the wall between the domains and so could only make statements about the magnetization within the domains themselves, giving only a rough estimate of the regions in parameter space where they might be expected to be found.

Experimentally, the difficulties involved with large pump amplitudes were solved already 20 years ago [Doet]. Renewed interest in this topic has led to recent work where, using the Faraday effect, dynamic domains were observed in garnet films driven by high power inhomogeneous driving fields [Wöbe98, Wöbe99].

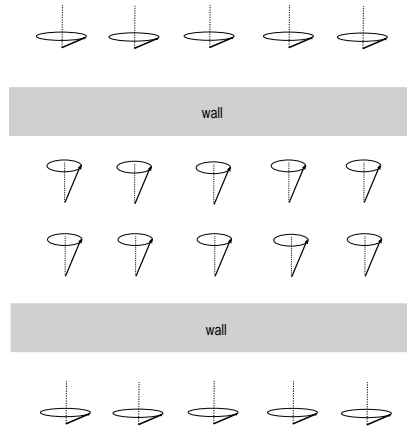


Figure 1.1: Sketch of a dynamic domain state. The magnetization rotates in locally homogeneous regions separated by a wall of finite width

In this work we investigate dynamic domains in ferromagnetic films. We use the Landau-Lifshitz equation including damping to model the dynamics of the magnetization within the film. The film is assumed to be infinitely extended in two dimensions. The model includes a (saturating) static field in the direction normal to the film (z direction) and a homogeneous transverse driving field in the plane of the film. The model also includes an easy axis anisotropy in the z direction, the exchange interaction and the long-range (demagnetizing) part of the dipole effect. This model and the different effects included are discussed in detail in Chapter 2.

The work is divided into two parts. Part I is the numerical investigation. Firstly, in Chapter 3, we discuss how the numerical simulations were carried out, while Chapter 4 considers in detail the numerical solutions found. We see that homogeneous (where all the spins in the probe rotate in phase) and dynamic domain solutions are found. The dynamic domains are observed in the form of stripes and bubbles. In addition we look at the regions in parameter space that the different solutions are found and investigate the critical thresholds of the driving field amplitude where the various solutions vanish.

In Part II the analytical investigation is carried out. In Chapter 5 we discuss the homogeneous solutions and, by means of a linear stability analysis, the regions in parameter space where such solutions are stable. In Chapter 6 we use a simple model to investigate the features of dynamic domains far from the domain wall. Again a linear stability analysis discusses necessary conditions for the stability of such solutions.

In Chapter 7 we look at the wall between the dynamic domains. We see that dynamic domain fixpoints of the equation of motion can only be obtained exactly

in the limiting case of no damping in the system. We therefore carry out a perturbation calculation and obtain approximate solutions for the case of small damping. We also consider where this perturbation calculation is valid and where it breaks down. Chapter 7 also contains an investigation into the effect of the wall curvature on dynamic domain solutions and hence looks at the differences between stripe domains and bubble domains. We consider only the situation where the curvature of the domain wall is small.

Now, it is known that when a saturating static field is applied parallel to the easy axis of a probe containing a *static* domain structure, the domain walls move towards each other and collide, leaving the probe in a homogeneous spin-up state ([ScWa] and Appendix C). However, in our case, there is also a transverse pump field present. The question arises of whether and under which circumstances the transverse pump field can call a halt to the travelling of domain walls and permit the presence of a stable dynamical domain state. This is the subject of Chapter 8, where, by linearizing the equations of motion around the Bloch wall, we investigate a stability criterion that must be satisfied for dynamic domain solutions to be found.

Chapter 9 compares the numerical results with those obtained by analytical methods. We also discuss in what regions of parameter space the various approximate analytical theories are valid. Finally, Chapter 10 provides a summary of the calculations and results.

Chapter 2

The Landau-Lifshitz Equation

In this work we investigate spatio-temporal pattern formation in ferromagnetic films. The length scales of the patterns we are interested in are large compared to the atomic distance of such substances and so the relevant quantity is a macroscopic variable, the local magnetization $\mathbf{m}(\mathbf{r}, t)$. The dynamics of $\mathbf{m}(\mathbf{r}, t)$ are described by the Landau-Lifshitz equation:

$$\partial_t \mathbf{m} = -\mathbf{m} \times \mathbf{h}_{\text{eff}} - \Gamma \mathbf{m} \times (\mathbf{m} \times \mathbf{h}_{\text{eff}}) \quad . \quad (2.1)$$

Equation (2.1) is a dimensionless equation, made so by scaling with the magnitude of the saturation magnetization of the probe and the gyromagnetic ratio.

The first term in equation (2.1) describes the precession of the magnetization around an effective magnetic field \mathbf{h}_{eff} , while the second term is a damping term. This damping term was first introduced phenomenologically by Landau and Lifshitz in 1935 [LaLi] and describes relaxation of the magnetization towards the effective field. Scalar multiplying equation (2.1) by \mathbf{m} , we obtain

$$\mathbf{m} \cdot \partial_t \mathbf{m} = \frac{1}{2} \partial_t (\mathbf{m}^2) = 0 \quad .$$

Therefore the magnitude of the magnetization vector $|\mathbf{m}|$ is a conserved quantity of the motion, and the Landau-Lifshitz equation (2.1) describes only the variation in direction of the vector \mathbf{m} .

Equation (2.1) has also been derived from the microscopic electron spin dynamics [Plef93, Gara], where its validity for ferromagnets below the Curie temperature was shown. In this region the magnitude of the magnetization does indeed remain approximately constant, and so the alternative Bloch damping, which describes a relaxation of the magnitude of the magnetization to the saturation magnetization, may be neglected compared to the Landau-Lifshitz damping above.

2.1 Effective Magnetic Field

The effective magnetic field is made up of both external and internal magnetic fields:

$$\mathbf{h}_{\text{eff}} = H\mathbf{e}_z + h(\cos(\omega t)\mathbf{e}_x + \sin(\omega t)\mathbf{e}_y) + J\nabla^2\mathbf{m} - \bar{m}_z\mathbf{e}_z + Km_z\mathbf{e}_z \quad . \quad (2.2)$$

The two external fields in this expression are as follows:

- A static field normal to the film of magnitude H . This field is generally taken to be saturating, i.e. $H > |\mathbf{m}| = 1$.
- A driving field perpendicular to the static field in the x - y plane of magnitude h and frequency ω . The probe is then said to be transversally pumped. Throughout the numerical part of this work we consider a resonant driving field, in dimensionless form $H = \omega$.

The three internal fields taken into account are:

- A strong isotropic exchange field with magnitude J . This describes the short-range exchange interaction between the electron spins and is quantum mechanical in origin. Taking the continuum limit of a nearest-neighbor interaction leads to the second spatial derivative [Akhi]. The exchange energy is thus described classically and is associated with magnetic inhomogeneity in the probe. For a ferromagnet $J > 0$.
- The dipolar field, a nonlocal field satisfying the solutions of magnetostatics:

$$\begin{aligned} \nabla \cdot (\mathbf{h}_{\text{dip}}(\mathbf{r}) + \mathbf{m}(\mathbf{r})) &= 0 \\ \nabla \times \mathbf{h}_{\text{dip}}(\mathbf{r}) &= 0 \end{aligned} \quad (2.3)$$

Initially¹ we only discuss the long-range ($k = 0$) part of the dipolar term, called the demagnetizing term, where

$$\mathbf{h}_{\text{dip}}(\mathbf{r}) = -\nabla(\bar{\mathbf{m}} \cdot \nabla) \int \frac{d\mathbf{r}'}{|\mathbf{r} - \mathbf{r}'|} = -N\bar{\mathbf{m}} \quad ,$$

where $\bar{\mathbf{m}}$ is the average of the magnetization over the probe. The ferromagnetic film described in this work is assumed to be infinitely extended in the x - y plane and of zero thickness in the z direction. This is motivated by experimental efforts using the Faraday effect which can only resolve patterns in the plane of the film and cannot detect any structure throughout the

¹The full dipolar field including $k \neq 0$ terms is discussed in Chapter 3.

film's thickness. Hence the system is treated as a spatially two-dimensional bulk system and boundary effects are neglected.

In the case of ellipsoids, the demagnetizing field is uniform. (The integral is a quadratic function of the coordinates, and so its second derivative is constant [Akhi]). The demagnetizing tensor N contains the shape of the probe. In the case of an oblate ellipsoid of infinite extent in the x and y directions (a film) the only non-zero component of N is $N_{zz} = -1$. Thus we have $\mathbf{h}_{\text{dip}} = -\overline{m}_z \mathbf{e}_z$, where \overline{m}_z , the z -component of the magnetic field averaged over the probe may be written as:

$$\overline{m}_z = \frac{1}{4L^2} \int_{-L}^L \int_{-L}^L m_z(x, y) dx dy$$

for a film of side $2L$, or for an infinitely extended film with a magnetization pattern which repeats itself with periodicity $2L$ in both the x and y directions.

- A uniaxial anisotropy in the z direction of magnitude K . This interaction may be derived from the spin-orbit Hamiltonian [Akhi] and for the easy axis case considered in this work ($K > 0$), the anisotropy energy is a minimum when the magnetization is aligned parallel to the z axis.

Unless otherwise stated, the quantities H, h, J, K are all large and may not be neglected.

2.2 Rotating Reference Frame

The Landau-Lifshitz model equation (2.1) with effective field (2.2) as it stands is explicitly time dependent. We can remove the explicit time dependence and attain an autonomous equation by carrying out a transformation to a reference frame rotating in the x - y plane with frequency ω , i.e. with the driving field. This transformation is as follows:

$$\mathbf{m}_{\text{rrf}} = (e^{-\omega t \mathbf{e}_z \times}) \mathbf{m}_{\text{lab}} \quad (2.4)$$

The expression $e^{-\omega t \mathbf{e}_z \times}$ is a rotation operator (or *versor* [Laga]) defining a rotation about the \mathbf{e}_z axis by an angle $-\omega t$. This operator leaves vectors in the \mathbf{e}_z direction unaffected and its action on vectors in the x - y plane is defined via the power series expansion of the operator:

$$\begin{aligned} (e^{-\omega t \mathbf{e}_z \times}) \mathbf{e}_y &= \cos \omega t \mathbf{e}_y + \sin \omega t \mathbf{e}_x \\ (e^{-\omega t \mathbf{e}_z \times}) \mathbf{e}_x &= \cos \omega t \mathbf{e}_x - \sin \omega t \mathbf{e}_y \end{aligned}$$

In order to obtain the Landau-Lifshitz equation in the rotating reference frame we replace $\mathbf{m} \equiv \mathbf{m}_{\text{lab}}$ in equation (2.1) with the inverse of definition (2.4):

$$\mathbf{m}_{\text{lab}} = (e^{+\omega t \mathbf{e}_z \times}) \mathbf{m}_{\text{rrf}}$$

After cancelling out the operator $e^{-\omega t \mathbf{e}_z \times}$ (or, more precisely, applying $e^{\omega t \mathbf{e}_z \times}$ from the left and noting that the operators $e^{\omega t \mathbf{e}_z \times}$ and $\mathbf{e}_z \times$ commute), equation (2.1) yields:

$$\partial_t \mathbf{m}_{\text{rrf}} = -\mathbf{m}_{\text{rrf}} \times (\mathbf{h}_{\text{eff,rrf}} - \omega \mathbf{e}_z) - \Gamma \mathbf{m}_{\text{rrf}} \times (\mathbf{m}_{\text{rrf}} \times \mathbf{h}_{\text{eff,rrf}}) \quad (2.5)$$

where

$$\begin{aligned} \mathbf{h}_{\text{eff,rrf}} &:= (e^{-\omega t \mathbf{e}_z \times}) \mathbf{h}_{\text{eff,lab}} \\ &= H \mathbf{e}_z + h \mathbf{e}_x + J \nabla^2 \mathbf{m}_{\text{rrf}} - \bar{m}_z \mathbf{e}_z + K m_z \mathbf{e}_z \end{aligned} \quad (2.6)$$

The additional term $\omega \mathbf{m}_{\text{rrf}} \times \mathbf{e}_z$ on the right-hand side of equation (2.5) is due to the time derivative of the rotation operator.

Hence steady state solutions obtained in the rotating reference frame correspond to precession of these solutions with frequency ω in the x - y plane in the lab frame. This fact must be borne in mind when viewing the results in the following chapters that have been calculated (either numerically or analytically) in the rotating reference frame. (In what follows, the subscript rrf will generally be neglected when performing calculations in the rotating reference frame.)

Multiplying equation (2.5) from the left by $\Gamma \mathbf{m} \times$ and recalling that $\mathbf{m} \cdot \mathbf{m} = 1$, we obtain

$$\Gamma \mathbf{m} \times \partial_t \mathbf{m} = -\Gamma \mathbf{m} \times (\mathbf{m} \times \mathbf{h}_{\text{eff}}) + \Gamma \omega \mathbf{m} \times (\mathbf{m} \times \mathbf{e}_z) + \Gamma^2 \mathbf{m} \times \mathbf{h}_{\text{eff}}$$

The term $\Gamma \mathbf{m} \times (\mathbf{m} \times \mathbf{h}_{\text{eff}})$ can be replaced with the help of equation (2.5), and after some sorting, we obtain the Gilbert form of the Landau-Lifshitz equation:

$$\partial_t \mathbf{m} - \Gamma \mathbf{m} \times \partial_t \mathbf{m} = -(1 + \Gamma^2) \mathbf{m} \times \left(\mathbf{h}_{\text{eff}} - \frac{\omega}{1 + \Gamma^2} \mathbf{e}_z + \frac{\Gamma \omega}{1 + \Gamma^2} \mathbf{m} \times \mathbf{e}_z \right) \quad (2.7)$$

The damping coefficient Γ is the same in both the Gilbert form of the Landau-Lifshitz equation (2.7) and the common form (2.5).

Part I

Numerical Simulation

Chapter 3

Notes on Computation and Representation

The time-independent Landau-Lifshitz equation (2.5) with (2.6) was simulated on the vector-parallel supercomputer *heiping*, a Fujitsu/SNI-VPP300. The source code of the program is based on a Fortran routine written by Matthäus and extended by Plefka [MaPl].

Spectral Approach

The numerical simulations of the partial differential equation (2.1) are carried out on a two-dimensional spatial grid with $n \times n$ mesh points. The boundary conditions are periodic. When the number of mesh points in each direction n is large enough it is expected that the boundary conditions have no effect on the structures within the probe¹.

Rather than dealing with the exchange term (second spatial derivative in x and y directions) using a finite difference method or similar, a *spectral approach* is chosen. The internal field contributions to the effective magnetic field (exchange, demagnetizing, anisotropy) are transformed into Fourier space. This has the advantage that in k -space the $n \times n$ difference equations that would otherwise be coupled via the short-range exchange and the long-range dipolar interaction are decoupled. This also allows the vector nature of the supercomputer to be exploited more fully.

¹This was indeed confirmed by performing the simulations also with unpinned spins ($\partial\mathbf{m}/\partial\xi = 0$ at the edge of the film, where ξ is the coordinate normal to the edge of the film [RaWe]) and it was seen that the same results were obtained, sometimes shifted slightly so that a domain wall never appeared at the edge of the probe.

The second order central finite difference representation of the Laplace term yields a term in Fourier space of the form

$$\cos \frac{2\pi k_x}{N_x} + \cos \frac{2\pi k_y}{N_y} - 2$$

correct up to errors of the order (Δ^2) , while the fourth order difference representation in Fourier space of the Laplace term is

$$- \cos \frac{4\pi k_x}{N_x} + 16 \cos \frac{2\pi k_x}{N_x} - \cos \frac{4\pi k_y}{N_y} + 16 \cos \frac{2\pi k_y}{N_y} - 30$$

correct up to errors of the order (Δ^4) . Here N_x and N_y are the number of mesh points in the x and y directions respectively (in simulations $N_x = N_y = n$), while Δ is the spacing between the grid points.

Throughout the simulation results presented here, only part of the dipole field included initially is the long-range ($k = 0$) part:

$$m_{0z} = -1 \quad \text{and} \quad m_{kz} = 0 \quad \text{for} \quad k \neq 0$$

For completeness, the effect of the full dipole field including $k \neq 0$ terms can also be included in the simulations². In Fourier space this is written as [Wige94]:

$$\mathbf{h}_{\text{dip}k} = - \frac{\mathbf{m}_k \cdot \mathbf{k}}{k^2} \quad ,$$

with $\mathbf{k} = k_x \mathbf{e}_x + k_y \mathbf{e}_y$ for this two-dimensional system. It was seen that including the full dipole field had little effect on the final domain structures found in the parameter regions observed, and so only the $k = 0$ demagnetizing part was retained.

Additional Damping Term

Throughout the course of a simulation we require that the magnitude of the magnetization $|\mathbf{m}|$ remain constant at one. However, the accumulation of numerical errors means that this is not the case, and the magnetization tends to drift away from the value one in time. Therefore we add an additional Bloch-like damping term to the equation of motion (2.5) that recalls the length of the magnetization vector back to one at each time step. This Bloch damping is purely a reaction to a numerical artifact.

²In this case the transformation to the rotating reference frame cannot be carried out and the time-dependent Landau-Lifshitz equation (2.1) with (2.2) must be simulated

Numerical Parameters

The number of mesh points was varied up to a maximum of 128×128 , bearing in mind that a fast Fourier transform is more efficient when performed on a list of length 2^n . The grid size of 64×64 chosen for all simulation results presented here was extracted from a compromise between speed and the necessity of being able to recognize structures. The magnitude of the exchange term $J/(2L)^2$, where $2L = 32$ is the system length, was varied such that a domain wall had an approximate “width” of 6-8 grid points, allowing the structure of the wall to be seen clearly. In general a second-order spatial differencing scheme was used as in the parameter regimes investigated little difference in results was found compared to fourth order.

Three different types of time integration were implemented and compared: Euler integration (first order) and Runge-Kutta second and fourth order. In the parameter regimes investigated, a time-step size of $dt \approx 0.01$ was found to suffice. In general a Euler time integration scheme was used. No difference in results between this scheme and a Runge-Kutta scheme could be observed in the parameter regions investigated, and the Runge-Kutta scheme required considerably more time to compute.

The total simulation time required to obtain a final solution varied depending on the proximity of a change in the stability of a solution (critical slowing-down phenomenon). Far from a critical value of h (denoted h_{c1} , h_{c2} and h_{c3} in subsequent chapters) a time of $5T$, where $T = 2\pi/\omega$, the period of the driving field, was typically required for the final stable state to form. Close to a critical value of h , times of up to $60T$ were needed before the final stable state formed.

Physical Parameters

The physical parameters in the system are Γ , the damping³; H , the static field in z -direction; h , the amplitude of the transverse driving field; ω , the frequency of the driving field; J , the exchange parameter; and K , the anisotropy. Throughout the numerical investigation into dynamic domains, the parameter varied was h , the amplitude of the driving field. All other physical parameters in the simulations shown are held constant: $\Gamma = 0.1$, $H = \omega = 3$ (system at resonance), $J = 10$ (and so $J/(2L)^2 = 0.01$ for $2L = 32$), $K = 5$.

³The damping constant Γ can be determined from the linewidth in magnetic resonance experiments and is found to be very small $\sim 10^{-4}$ in the particular example of yttrium-iron garnet films with smooth surfaces. The larger value $\Gamma = 0.1$ was chosen for numerical simulations to reduce the time taken for transient behavior to die away.

Stroboscopic Representation

Of course it would also be possible to simulate the *time-dependent* Landau-Lifshitz equation (2.1) with (2.2) in the lab frame. The results are equivalent, as was indeed confirmed by simulation of the transformed time-dependent Landau-Lifshitz equation (2.1) for a large variety of parameter values. A result that is *statically* stable in the rotating reference frame will appear *dynamically* stable in the lab frame if we view the simulation once per period T . Thus the results in the rotating reference frame can be thought of as a *stroboscopic* view of the results in the lab frame.

Chapter 4

Numerical Dynamic Domains

To investigate systematically the presence of dynamically stable structures, all numerical and physical parameters except the amplitude of the driving field were kept constant ($H = \omega = 3$, $K = 5$, $J = 10$, $\Gamma = 0.1$), while h was varied from $h = 0$ upwards. Depending on the initial states and on the value of h , different dynamically stable solutions are found.

We recall that the results presented in this chapter are shown in the rotating reference frame. This is equivalent to a stroboscopic view of the situation in the lab frame, where the magnetization in the probe is not static as appears in the figures, but actually rotates around the z axis with frequency ω .

4.1 Homogeneous State

The solution found most frequently in numerical simulations is the homogeneous or uniform solution. In this case, all the spins throughout the probe rotate at the same frequency, in phase, and with the same constant m_z . Figure 4.1 shows the m_x , m_y and m_z components of the magnetic field in homogeneous dynamically stable states for different values of the driving field h .

The dynamically stable homogeneous state is found numerically for values of h below a certain critical value $h_{c1} \approx 3.7$ and above another critical value $h_{c2} \approx 5$.

A macroscopic parameter describing the state is \overline{m}_z , the magnitude of the demagnetizing field in the film. In the homogeneous case this is simply m_z , and it varies from $\overline{m}_z = +1$ at $h = 0$ (the entire probe in the spin up state) to $\overline{m}_z \rightarrow 0$ for $h \rightarrow \infty$, when the spins rotate essentially in the x - y plane because the amplitude of the rotating field is much larger than that of the static field in z direction.

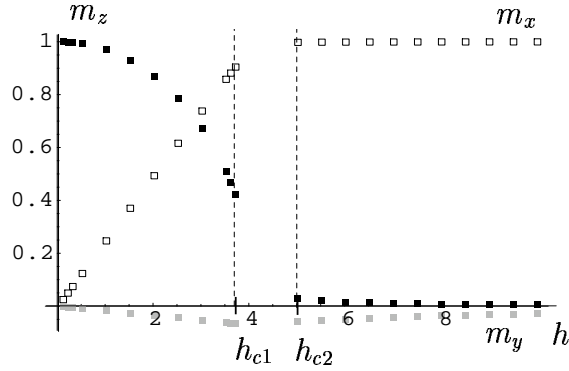


Figure 4.1: Dynamically stable homogeneous states obtained at the parameter values: $J = 10$, $\omega = H = 3$, $K = 5$ for different values of h . The open squares are the m_x components, the gray squares the m_y components and the black squares the m_z components of the magnetization. No dynamically stable homogeneous states are found between $h_{c1} \approx 3.7$ and $h_{c2} \approx 5$

4.2 Stripes and Bubbles

Some of the two-domain dynamically stable structures also found are shown in Figure 4.2. This is a shaded contour plot of the m_z component of the magnetization throughout the probe. The dark areas depicted are those where $m_z < 0$ while the light areas imply $m_z > 0$. Figure 4.2 makes no statement about the x and y components of the magnetization, which (apart from at the wall) are spatially homogeneous and vary periodically in time with period ω . This implies that the spins within the domains rotate in the x - y plane in phase and at the same frequency.

The simulations were performed with a great many different initial conditions. The results shown in Figure 4.2 are characteristic of *all* the dynamic domain results obtained, i.e. dynamically stable domain states either have either translational symmetry (**b**, **c** and **d**) or rotational symmetry (**a**, **e** and **f**). In particular simulations were performed with initial conditions in the shape of an oval and a square. The oval was seen to stretch in time, eventually forming a stable stripe solution, while the square resulted in a stable bubble solution.

The m_z component of the magnetization in each co-existing dynamic domain is shown in Figure 4.3 for different values of h . It is observed that dynamically stable domain states only exist between two values of the driving field, called h_{c3} and h_{c4} . As we approach the upper bound h_{c4} the domain states become ever more flattened out, until eventually at h_{c4} the domain state merges into the homogeneous state. This continuous transition is in direct contrast to the lower bound h_{c3} where a well-defined domain state suddenly no longer exists. The bounds $h_{c3} \approx 0.2$ and $h_{c4} \approx 5$ are clearly visible in Figure 4.3. The values

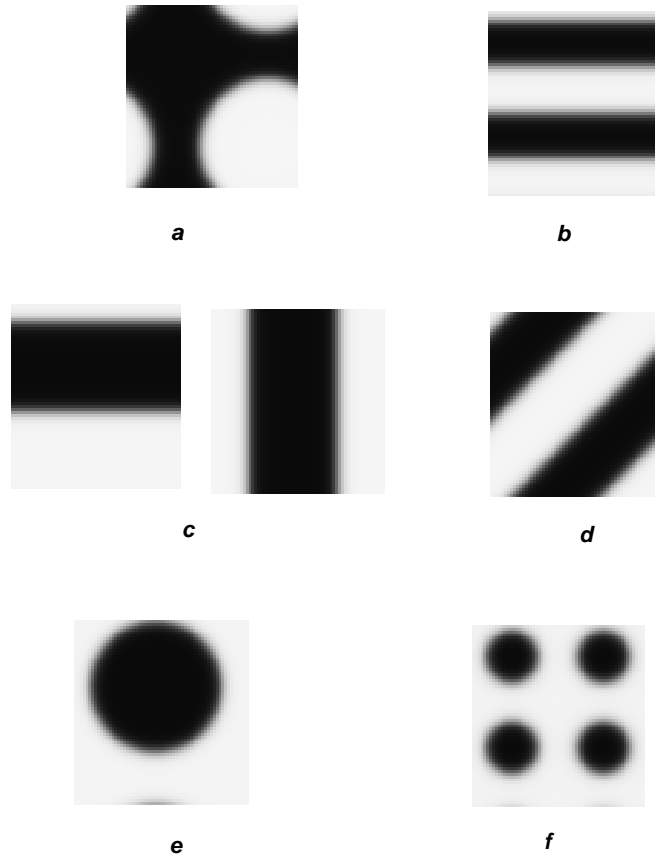


Figure 4.2: Dynamically stable domain states obtained at the same parameter values: $J = 10$, $\omega = H = 3$, $h = 2$, $K = 5$. a) “spin-up” bubble, period $2L$; b) horizontal stripes, period L ; c) horizontal and vertical stripes, period $2L$; d) diagonal stripes, period $\sqrt{2L}$; e) “spin-down” bubble, period $2L$; f) “spin-down” bubble, period L

of h_{c3} and h_{c4} were seen to be the same whether bubbles or stripes were under investigation.

Again we can consider \bar{m}_z as an indication of the macroscopic state of the probe. Here differences are found between stripes and bubbles. The results are summarized in Figure 4.4.

In the case of stripes, \bar{m}_z has the same very small positive value ($\bar{m}_z \approx 0.03$) for all h at which stripes are stable.

In the case of bubbles, \bar{m}_z varies with h . For “spin-up” bubbles, where $m_z > 0$ inside the bubble and $m_z < 0$ outside the bubble, the average magnetization throughout the probe is always negative, rising from $\bar{m}_z \approx -0.3$ at $h = h_{c3}$ to $\bar{m}_z \approx 0$ as $h \rightarrow h_{c4}$.

For “spin-down” bubbles, where $m_z < 0$ inside the bubble and $m_z > 0$ outside

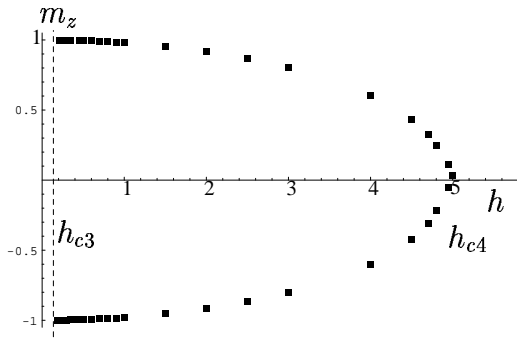


Figure 4.3: The z -component of the magnetization within dynamic domains as obtained from numerical simulations. Each pair of dots for a given value of h corresponds to the m_z values far from the domain wall for a single numerically stable simulation

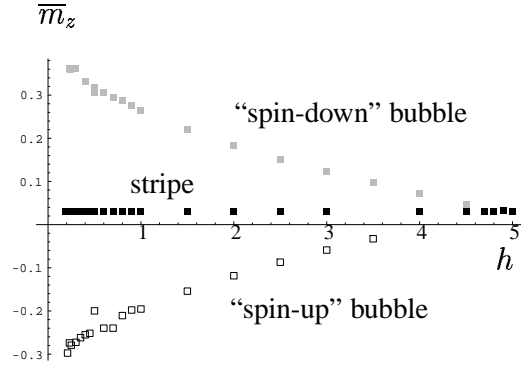


Figure 4.4: Demagnetizing field in dynamic domain states; each square corresponds to the final state of a numerical simulation, with stripe domains (filled square), “spin-down” bubble domains (gray square) and “spin-up” bubble domains (open square)

the bubble, the average magnetization throughout the probe is always positive, falling from $\bar{m}_z \approx 0.3$ at $h = h_{c3}$ to $\bar{m}_z \approx 0$ as $h \rightarrow h_{c4}$.

4.3 Wall Structure

The spatially distinct uniform regions are separated by a domain wall. Here the magnetization does not jump from the value in one domain to the next, but rather varies continuously across the finite wall width. The spins inside the wall rotate at the same frequency with the rest of the probe, but with a phase shift compared to the spins within the domains. A schematic view of the top elevation of a stripe domain wall and a bubble domain is shown in Figure 4.5. In the domain wall all the spins are parallel. In particular, this is also true for the bubble domain wall and so the whole structure including wall is *not* rotationally symmetric. The rotational symmetry of the system is broken by the presence of the driving field h . Such bubble domains as sketched in Figure 4.5 were always obtained, even if rotationally symmetric initial conditions were used.

The m_x , m_y and m_z components of the magnetization through a wall between two (striped) dynamical domains are shown in Figure 4.6, for the cases $h = 0.2 \approx h_{c3}$ and $h = 3 \gg h_{c3}$.

The structure of the wall differs depending on h . For small h close to the lower bound, at the center of the wall the largest component of \mathbf{m} is m_y which is

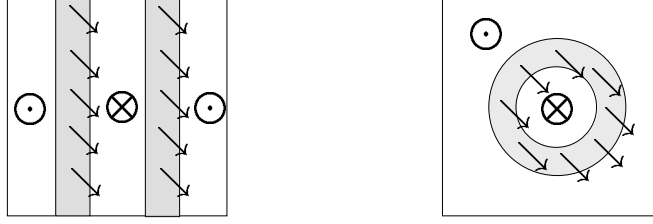


Figure 4.5: Sketch of the orientation of the spins in the probe in the rotating reference frame for stripe dynamic domains (left) and bubble dynamic domains (right). The view is from above onto the plane of the film. Within the domains $m_z > 0$ (denoted by \otimes) or $m_z < 0$ (denoted by \odot). The magnetization rotates from one position to the next in the domain wall (shaded gray). At the center of the wall $m_z \approx 0$ and the arrows indicate the general direction of orientation of the magnetization

negative. As h increases, m_x dominates ever more at the center of the wall, while m_y shrinks to almost zero. In addition, as h is increased, the width of the wall increases and an ever larger part of the probe is spatially inhomogeneous. We noted above that the domains themselves become flattened out. This, together with the ever widening wall, means that it is not possible to say precisely when the domain state merges into the homogeneous state at the upper bound.

Plots like those in Figure 4.6 are shown for many more values of h in Figure 9.4, where at that point the numerical results are compared to results from theories developed later in this work.

As $|\mathbf{m}|$ is a conserved quantity of the motion, the three variables m_x, m_y and m_z are of course not independent of each other. Since $|\mathbf{m}|$ is scaled to 1 in this dimensionless system, a one-dimensional state $\mathbf{m}(\xi, t)$ can be plotted at any given time t_0 as a 1-parameter curve on the surface of a unit sphere with the origin of all \mathbf{m} vectors at the center of the sphere.

Figure 4.7 shows plots equivalent to those in Figure 4.6, for the same two values of h . Above, we see the solution obtained for $h = 0.2 \approx h_{c3}$, the lower critical point for stripe and bubble domain states. In this case m_z varies through from $m_z \approx +1$ to $m_z \approx -1$. In doing so it rotates about an axis that is approximately constant throughout the rotation process. This axis \mathbf{a} is indicated by an arrow in the top elevation of the unit sphere shown on the right-hand side of Figure 4.7. For the case $h \approx h_{c3}$, the axis \mathbf{a} is almost in the direction of $-\mathbf{e}_y$.

The lower pictures show the case for $h \gg h_{c3}$, namely for $h = 3$ where m_z varies between $m_z \approx 0.8$ and $m_z \approx -0.8$. In this case the axis \mathbf{a} is approximately in the direction $-\mathbf{e}_x$.

Other values of h (not depicted here) show similar behavior. The magnetization on the sphere always passes through the lower right-hand quadrant of the top

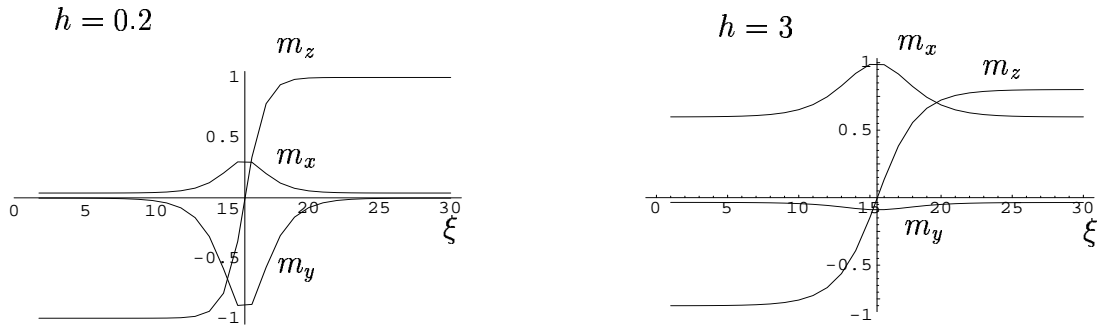


Figure 4.6: Numerical simulation: Spatial variation of m_x , m_y and m_z components of the magnetization across a (stripe) domain wall for the case $h = 0.2 \approx h_{c3}$ and $h = 3 \gg h_{c3}$. ξ is the direction normal to the plane of the wall. The numbers on the horizontal axes are grid points

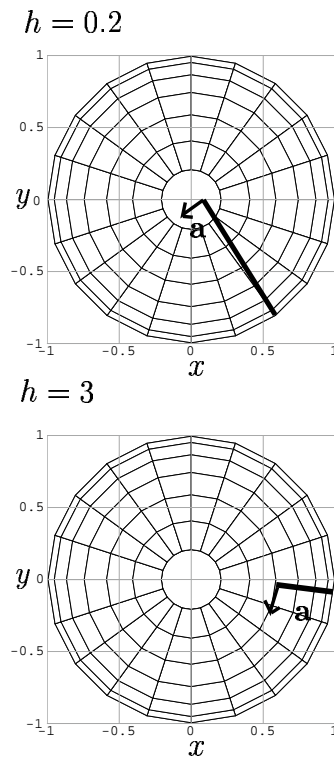


Figure 4.7: Numerical simulation: Stripe domain wall traced on a unit sphere for $h = 0.2 \approx h_{c3}$ (above) and for $h = 3 \gg h_{c3}$ (below). The figures show the top elevation, making it easier to identify the axis \mathbf{a} about which the magnetization rotates, denoted with an arrow

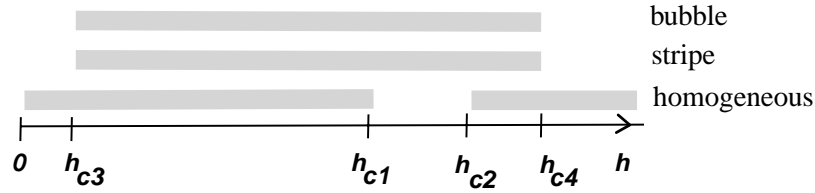


Figure 4.8: Schematic view of where the homogeneous, stripe and bubble solutions are found numerically, h is the amplitude of the driving field

elevation of the unit sphere. The axis about which the magnetization rotates is approximately constant in space and varies from $\mathbf{a} \approx -\mathbf{e}_y$ for $h \approx h_{c3}$ to $\mathbf{a} \approx -\mathbf{e}_x$ for $h \approx h_{c4}$.

The illustrations shown in Figure 4.7 correspond to the walls between striped dynamical domains. The same procedure can be carried out for bubble domains, again choosing the direction normal to the wall, in this case the radial polar coordinate, as ξ . There appears to be no difference between stripes, “spin-up” bubbles and “spin-down” bubbles when we look at orientation of the spins inside the wall.

4.4 Bistability and Hysteresis

Figure 4.2 already indicates that many different probe structures are numerically dynamically stable at the set of same parameter values. Clearly there is bistability present, or tristability if we recall that the spatially homogeneous solution is also dynamically stable at this set of parameter values. This bistability is shown schematically in Figure 4.8. Which of these patterns actually occurs depends on the initial conditions of the probe.

The homogeneous solution exists between h_{c1} and h_{c2} and the domain solution between h_{c3} and h_{c4} . h_{c3} is much smaller than h_{c1} , and so between these two points both homogeneous and domain solutions exist. Although h_{c2} and h_{c4} are both approximately 5, there is no indication that they take on exactly the same numerical value. In fact it appears that h_{c2} is slightly smaller than h_{c4} , so that again there is a region of overlap where both types of solution exist.

Two hysteresis loops occur in the system as follows: If we begin with a homogeneous initial condition and a driving field amplitude $h = 0$ and slowly increase h , the state of the probe remains spatially uniform until we reach the field strength $h_{c1} \approx 3.7$. The homogeneous state is then no longer stable and a striped domain state spontaneously appears in the probe. This remains so until $h_{c4} \approx 5.1$ when the stripe state merges into the homogeneous state, where it remains for $h > h_{c4}$.

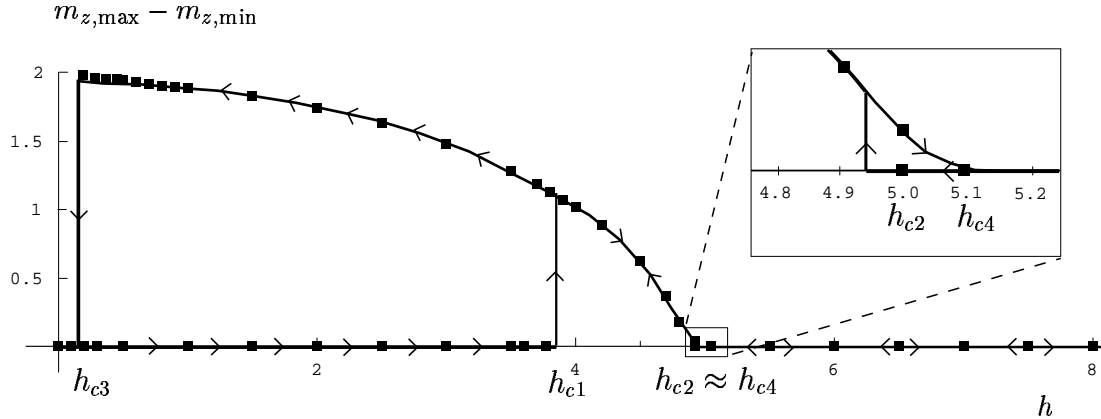


Figure 4.9: Hysteresis between the homogeneous and domain solutions. The figure plots $m_{z,\max} - m_{z,\min}$ vs h , the strength of the driving field. For the homogeneous state $m_{z,\max} - m_{z,\min} = 0$, while for bubble and stripe domains $m_{z,\max} - m_{z,\min} > 0$. Each dot is the result of a numerical simulation. Arrows indicate the direction of change of the driving field h and the direction of transition. There is a sharp transition from the uniform state to domains at $h_{c1} \approx 3.7$ and from the domain state to the homogeneous state at $h_{c3} \approx 0.2$. The region around $h \approx 5$ is enlarged to show more clearly the sharp transition from the homogeneous state to the domain state at $h_{c2} \approx 5$ and the continuous transition from the domain state to the homogeneous state at the somewhat higher value of h_{c4}

Then decreasing the field h again, the probe again becomes striped at $h_{c2} \approx 5$ and remains in this state until well below the original phase transition, only becoming homogeneous again at $h_{c3} \approx 0.2$. This behavior is shown in Figure 4.9.

The behavior of the probe at h_{c3} is of interest. We select as an initial state a domain state which would be stable just above h_{c3} . Reducing h a little below the critical value h_{c3} , the two walls on either side of the “spin-down” domain begin to move towards each other, and the spins within the walls to rotate faster and faster than the angular frequency of the driving field. Eventually the walls collide and leave the probe in a homogeneous “spin-up” state. The velocity of walls in this transient state is smaller the closer we are to the value $h = h_{c3}$, and it can take up to $60T$, where $T = 2\pi/\omega$ the period of the driving field, for the wall collision to occur. This is an example of the phenomenon of critical slowing down.

4.5 Nature of Critical Thresholds

Now we consider the stability of the solutions found numerically. These are of course all stable, stationary solutions to the Landau-Lifshitz equation in the rotating reference frame. However we are particularly interested in the critical

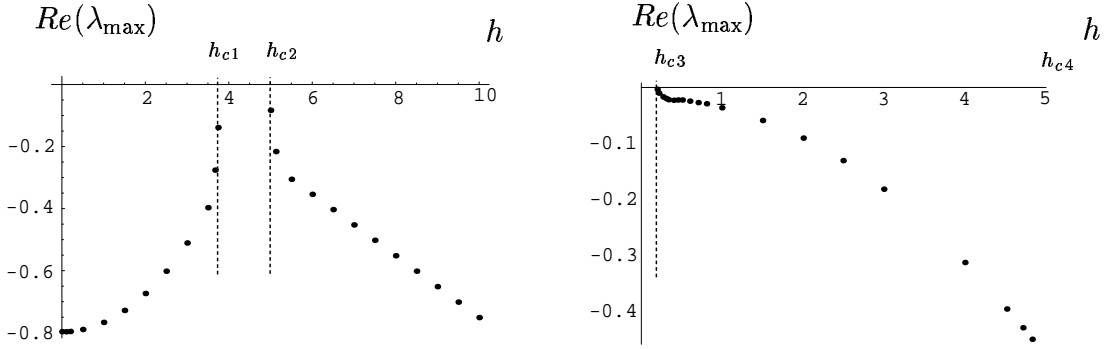


Figure 4.10: Investigation into relative stability of homogeneous solutions (left) and domain solutions (right) arising out of simulations: the largest real part of the eigenvalues of matrix $\underline{\underline{L}}$ is plotted against h , the amplitude of the driving field. Each point in the plot corresponds to the final state of one simulation

driving field amplitudes h_{c1}, \dots, h_{c4} and in what manner the homogeneous and domain solutions vanish at these points. We wish to consider the *relative* stability of the numerical solutions found.

We linearize the equation of motion (2.5) around the result from numerical simulation, called $\mathbf{m}_0 \equiv \mathbf{m}_0(\xi)$. The calculation may be performed on homogeneous, bubble or stripe states. In the homogeneous case $\mathbf{m}_0 = \text{const.}$; for stripes ξ is a Cartesian coordinate and for bubbles the radial polar coordinate. Now adding a small perturbation $\varepsilon \mathbf{m}_1(\xi, t)$ to this and recalling that the magnitude of the magnetization remains constant throughout the motion, i.e. $|\mathbf{m}_0| = 1 = |\mathbf{m}_0 + \varepsilon \mathbf{m}_1|$, we see that \mathbf{m}_1 must lie in a plane to which \mathbf{m}_0 is normal.

Therefore we use an adapted local coordinate system with one coordinate axis in the direction of \mathbf{m}_0 . This coordinate system is differently orientated at each of the n grid points over which the numerical solution is defined, and is described in Appendix A.

We attain a linearized equation of motion for the disturbance \mathbf{m} of the form

$$\dot{\mathbf{m}}_1 = \underline{\underline{L}} \mathbf{m}_1 \quad .$$

As \mathbf{m}_1 can only lie in a (two-dimensional) plane, it is represented by a vector of length $2n$, while $\underline{\underline{L}}$ is a $2n \times 2n$ matrix.

If one of more eigenvalues of $\underline{\underline{L}}$ has a positive real part, \mathbf{m}_1 will grow in time and \mathbf{m}_0 is unstable; otherwise \mathbf{m}_0 is stable. Of course all numerical \mathbf{m}_0 available to us must be stable, otherwise they would not have arisen out of the simulations. This means that all $2n$ eigenvalues λ_k of $\underline{\underline{L}}$ will have negative real parts.

On the left-hand side of Figure 4.10 we consider the homogeneous state at different driving field amplitudes h . The eigenvalue of $\underline{\underline{L}}$ with the *largest* real part, i.e.

that λ_k where $\text{Re}(\lambda_k)$ is closest to zero, is plotted against h . We see that for very small values of h , $\text{Re}(\lambda_{\max})$ is large and negative. As we move upwards towards $h_{c1} \approx 3.7$, $\text{Re}(\lambda_{\max})$ moves closer to zero, and so the solution is less stable. The same occurs moving downwards from large values of h to $h_{c2} \approx 5$. Thus there appears to be a change in the stability of the homogeneous solution at these two critical points.

On the right-hand side of Figure 4.10, numerically stable stripe solutions are considered. Again we look at the most “dangerous” eigenvalue of $\underline{\underline{L}}$. We see that for large h the final state is “more” stable than the final state at smaller h (the largest eigenvalue is more negative). This confirms what was discussed in Sections 4.2 and 4.4. The upper transition $h = h_{c4}$ is verified as a vanishing of the domain solution itself. In contrast, at the lower transition, the largest eigenvalue of $\underline{\underline{L}}$ becomes ever closer to zero, indicating a change in the stability of the dynamic domain solution at $h = h_{c3}$

Part II

Analytical Investigation

Chapter 5

Homogeneous Solution

The simplest steady state solution to the Landau-Lifshitz equation in the rotating reference frame (2.5) is the homogeneous or uniform solution. In the lab frame this implies that all spins in the system rotate in phase around the z -axis at the frequency ω of the transversal driving field h and have all the same m_z value.

5.1 Calculation of Homogeneous Solution

We begin with the Gilbert form of the Landau-Lifshitz equation in the rotating reference frame (2.7) with effective field (2.6). Homogeneous steady state solutions must satisfy the following conditions

$$\partial_t \mathbf{m} = 0 \quad , \quad \nabla^2 \mathbf{m} = 0 \quad ,$$

i.e. there should be no change in the magnetization in time and no inhomogeneities in the solution. We note that in the case of a homogeneous solution the average magnetization in the z -direction is the same as the magnetization itself in the z -direction:

$$\overline{m_z} = m_z \quad .$$

Therefore the effective magnetic field becomes:

$$\mathbf{h}_{\text{eff}} = H \mathbf{e}_z + h \mathbf{e}_x + (K - 1)m_z \mathbf{e}_z \quad . \quad (5.1)$$

Inserting (5.1) into equation (2.7) we obtain:

$$0 = \mathbf{m} \times \left[h \mathbf{e}_x + \left(H + (K - 1)m_z - \frac{\omega}{1 + \Gamma^2} \right) \mathbf{e}_z + \frac{\Gamma \omega}{1 + \Gamma^2} \mathbf{m} \times \mathbf{e}_z \right] \quad . \quad (5.2)$$

The expression in square brackets in (5.2) must be parallel to \mathbf{m} , with some unknown proportionality factor μ :

$$h\mathbf{e}_x + (\delta + am_z)\mathbf{e}_z + \gamma\mathbf{m} \times \mathbf{e}_z = \mu\mathbf{m} \quad , \quad (5.3)$$

where we have introduced the following definitions:

$$a = K - 1 \quad , \quad \delta = H - \frac{\omega}{1 + \Gamma^2} \quad , \quad \gamma = \frac{\Gamma\omega}{1 + \Gamma^2} \quad . \quad (5.4)$$

The parameter δ is a measure of the deviation of the system from resonance and is called the detuning, while γ is the rescaled frequency.

Taking the scalar product of equation (5.3) with \mathbf{e}_z leads to

$$m_z = \frac{\delta}{\mu - a} \quad . \quad (5.5)$$

Similarly taking the scalar products with \mathbf{e}_x and \mathbf{e}_y leads to two equations:

$$\begin{aligned} h + \gamma m_y &= \mu m_x \quad , \\ -\gamma m_x &= \mu m_y \quad , \end{aligned}$$

which may be solved simultaneously to give

$$m_x = \frac{\mu h}{\mu^2 + \gamma^2} \quad \text{and} \quad m_y = -\frac{\gamma h}{\mu^2 + \gamma^2} \quad (5.6)$$

An expression for the unknown factor μ is found from the additional requirement that $|\mathbf{m}| = 1$, i.e. $m_x^2 + m_y^2 + m_z^2 = 1$:

$$\frac{h^2}{\mu^2 + \gamma^2} + \frac{\delta^2}{(\mu - a)^2} = 1 \quad . \quad (5.7)$$

This is a fourth order polynomial in μ . By setting $\mu \rightarrow \frac{\delta}{m_z} + a$ from (5.5) we obtain a fourth order polynomial in the variable m_z

$$m_z^4(a^2 + \gamma^2) + m_z^3(2a\delta) + m_z^2(h^2 + \delta^2 - a^2 - \gamma^2) + m_z(-2a\delta) - \delta^2 = 0 \quad . \quad (5.8)$$

Either 2 or 4 solutions to equation (5.8) are found, depending on the parameter regime. In most of this work it is seen to be useful to fix the parameters H, ω, K and to vary h . This yields a solution curve as shown in Figure 5.1. As one passes from the regions of two solutions to regions of four solutions, it is a saddle-node bifurcation which yields two further solutions.

The positions of these saddle-node bifurcations may be found by computing the local maxima and minima of the inverse function to that shown in Figure 5.1,

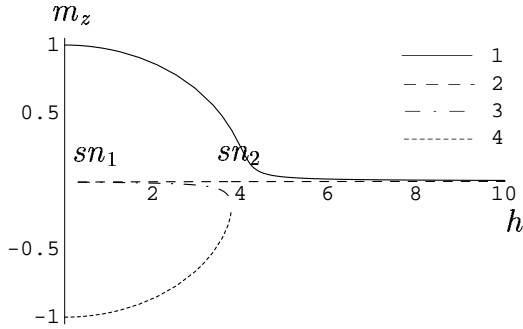


Figure 5.1: Dependence of solutions of equation (5.8) on the driving field h with other parameters fixed as $K = 5$, $H = \omega = 3$, $\Gamma = 0.1$. The four fixpoints depicted are labelled 1 to 4 from top to bottom

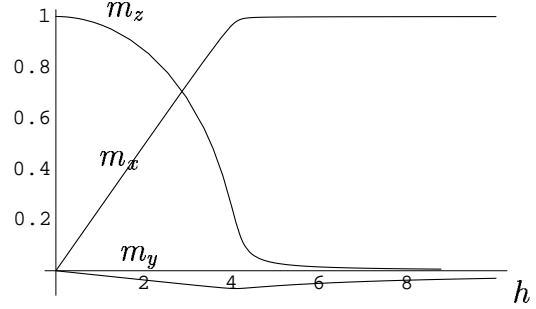


Figure 5.2: m_x , m_y and m_z components of the magnetization for the solution of the homogeneous fixpoint equation (5.8) where $m_z > 0$ (fixpoint 1) plotted against the amplitude of the driving field h . Other parameters as Figure 5.1

namely $h \equiv h(m_z)$. The equation (5.8) can be considered as a quadratic equation for h , with the solution

$$h = \sqrt{a^2 - \delta^2 + \gamma^2 + \frac{\delta^2}{m_z^2} + \frac{2a\delta}{m_z} - 2a\delta m_z - a^2 m_z^2 - \gamma^2 m_z^2} . \quad (5.9)$$

Setting $\partial h / \partial m_z = 0$ and solving for m_z yields the location of the two saddle-node bifurcations $m_{z,sn1}$ and $m_{z,sn2}$. These may be inserted back into equation (5.9) to obtain the two turning points explicitly h_{sn1} and h_{sn2} explicitly. Using the parameter values in Figure 5.1, the saddle-node bifurcations are located at $(h_{sn1}, m_{z,sn1}) = (0.297, -0.0075)$ and $(h_{sn2}, m_{z,sn2}) = (3.785, -0.195)$

In particular, we consider fixpoint 1, where m_z is always positive in the final state. We employ equation (5.6) and show the m_x and m_y components of the magnetization in Figure 5.2. It can be seen that for small h , the magnetization points essentially in the z direction. As h is increased, m_x begins to dominate, i.e. for large h the spins in the probe rotate essentially in the x - y plane with no component in the z direction.

5.2 Linear Stability Analysis

In the previous section we determined four homogeneous fixpoint solutions to the Landau-Lifshitz equation. We now consider their stability. To do so we denote the basic solution as \mathbf{m}_0 . We then add a small time and space dependent perturbation to \mathbf{m}_0 , and draw conclusions of the stability or instability of \mathbf{m}_0 from

whether the perturbation decays or amplifies in time, respectively. In particular we may consider one Fourier mode of such a perturbation:

$$\mathbf{m}(\xi, t) = \mathbf{m}_0 + \varepsilon \mathbf{m}_1(t) e^{ik\xi} \quad (5.10)$$

Now the magnetization $\mathbf{m}(\xi, t)$ must have magnitude 1:

$$|\mathbf{m}(\xi, t)| = |\mathbf{m}_0 + \varepsilon \mathbf{m}_1(t) e^{ik\xi}| = 1 \quad .$$

But \mathbf{m}_0 is already normalized to one. Thus \mathbf{m}_1 must lie in a plane perpendicular to \mathbf{m}_0 and so

$$\mathbf{m}_0 \cdot \mathbf{m}_1 = 0 \quad (5.11)$$

We insert ansatz (5.10) into the Landau-Lifshitz equation in the rotating reference frame (2.5) and sort for powers of ε .

In the zeroth order case $O(\varepsilon^0)$ we simply obtain an equation satisfied by the \mathbf{m}_0 obtained in the previous section:

$$0 = \mathbf{m}_0 \times [\mathbf{h}_{\text{eff},0} - \omega \mathbf{e}_z + \Gamma \mathbf{m}_0 \times \mathbf{h}_{\text{eff},0}] \quad . \quad (5.12)$$

The case $O(\varepsilon^1)$ yields:

$$\begin{aligned} -\dot{\mathbf{m}}_1 &= \mathbf{m}_1 \times (\mathbf{h}_{\text{eff},0} - \omega \mathbf{e}_z) + \mathbf{m}_0 \times \mathbf{h}_{\text{eff},1} + \\ &\Gamma [\mathbf{m}_1 \times (\mathbf{m}_0 \times \mathbf{h}_{\text{eff},0}) + \mathbf{m}_0 \times (\mathbf{m}_1 \times \mathbf{h}_{\text{eff},0}) + \mathbf{m}_0 \times (\mathbf{m}_0 \times \mathbf{h}_{\text{eff},1})] \end{aligned} \quad (5.13)$$

where we have introduced

$$\begin{aligned} \mathbf{h}_{\text{eff},0} &= H \mathbf{e}_z + h \mathbf{e}_x + (K - 1) m_{z,0} \mathbf{e}_z \\ \mathbf{h}_{\text{eff},1} &= -J k^2 \mathbf{m}_1 + K m_{z,1} \mathbf{e}_z - \overline{m}_{z,1} \mathbf{e}_z \quad . \end{aligned}$$

The field $\mathbf{h}_{\text{eff},1}$ depends on whether the case $k = 0$ or $k \neq 0$ is being considered, i.e. whether \mathbf{m}_1 is uniform or non-uniform. If $k = 0$, $\overline{m}_{z,1} = m_{z,1}$, whereas if $k \neq 0$, the fluctuations averaged over the entire probe are zero and so $\overline{m}_{z,1} = 0$. Therefore

$$\begin{aligned} \text{for } k = 0, \quad \mathbf{h}_{\text{eff},1} &= (K - 1) m_{z,1} \mathbf{e}_z \\ \text{for } k \neq 0, \quad \mathbf{h}_{\text{eff},1} &= K m_{z,1} \mathbf{e}_z - J k^2 \mathbf{m}_1 \quad . \end{aligned}$$

Note that the expression in square brackets in equation (5.12) is parallel to \mathbf{m}_0 . We can write

$$\mathbf{h}_{\text{eff},0} - \omega \mathbf{e}_z + \Gamma (\mathbf{m}_0 \times \mathbf{h}_{\text{eff},0}) =: B \mathbf{m}_0$$

Scalar multiplying this equation by \mathbf{m}_0 , we therefore obtain the proportionality factor B :

$$B = \mathbf{h}_{\text{eff},0} \cdot \mathbf{m}_0 - \omega m_{z,0} \quad ,$$

recalling that $\mathbf{m}_0 \cdot \mathbf{m}_0 = 1$.

Using this we can combine the first and third terms on the right-hand side of (5.13) as

$$\mathbf{m}_1 \times (\mathbf{h}_{\text{eff},0} - \omega \mathbf{e}_z) + \Gamma [\mathbf{m}_1 \times (\mathbf{m}_0 \times \mathbf{h}_{\text{eff},0})] = B \mathbf{m}_1 \times \mathbf{m}_0$$

Furthermore, exploiting (5.11), the fourth term on the right-hand side of (5.13) can be written as

$$\Gamma [\mathbf{m}_0 \times (\mathbf{m}_1 \times \mathbf{h}_{\text{eff},0})] = \Gamma (\mathbf{m}_0 \cdot \mathbf{h}_{\text{eff},0}) \mathbf{m}_1$$

This leads us to the linearized Landau-Lifshitz equation in its most compact form:

$$-\dot{\mathbf{m}}_1 = B \mathbf{m}_1 \times \mathbf{m}_0 + \Gamma (\mathbf{m}_0 \cdot \mathbf{h}_{\text{eff},0}) \mathbf{m}_1 + \mathbf{m}_0 \times [\mathbf{h}_{\text{eff},1} + \Gamma \mathbf{m}_0 \times \mathbf{h}_{\text{eff},1}] \quad (5.14)$$

We stated above that \mathbf{m}_1 must lie in a plane perpendicular to \mathbf{m}_0 . We therefore introduce a coordinate system defined as

$$\begin{aligned} \mathbf{e}_1 &= \mathbf{m}_0 \\ \mathbf{e}_2 &= \mathbf{m}_0 \times \mathbf{e}_z \\ \mathbf{e}_3 &= \mathbf{m}_0 \times (\mathbf{m}_0 \times \mathbf{e}_z) \end{aligned} \quad (5.15)$$

In this coordinate system \mathbf{m}_1 can be written as

$$\mathbf{m}_1(t) = \beta(t) \mathbf{e}_2 + \gamma(t) \mathbf{e}_3$$

and equation (5.14) assumes the form

$$\begin{aligned} -\dot{\beta} \mathbf{e}_2 - \dot{\gamma} \mathbf{e}_3 &= B(-\beta \mathbf{e}_3 + \gamma \mathbf{e}_2) + \Gamma (\mathbf{m}_0 \cdot \mathbf{h}_{\text{eff},0}) (\beta \mathbf{e}_2 + \gamma \mathbf{e}_3) + \\ &\quad \mathbf{e}_1 \times [\mathbf{h}_{\text{eff},1} + \Gamma \mathbf{e}_1 \times \mathbf{h}_{\text{eff},1}] \end{aligned} \quad (5.16)$$

The final expression containing $\mathbf{h}_{\text{eff},1}$ is different depending on whether we consider the case $k = 0$ or $k \neq 0$:

- For $k = 0$:

$$\mathbf{h}_{\text{eff},1} = a m_{z,1} \mathbf{e}_z$$

Therefore

$$\begin{aligned} \mathbf{e}_1 \times [\mathbf{h}_{\text{eff},1} + \Gamma \mathbf{e}_1 \times \mathbf{h}_{\text{eff},1}] &= a m_{z,1} (\mathbf{e}_1 \times \mathbf{e}_z + \Gamma \mathbf{e}_1 \times (\mathbf{e}_1 \times \mathbf{e}_z)) \\ &= a \gamma (m_{z,0}^2 - 1) (\mathbf{e}_2 + \Gamma \mathbf{e}_3) \end{aligned}$$

where we have used the fact that

$$\begin{aligned} m_{z,1} &= \mathbf{m}_1 \cdot \mathbf{e}_z \\ &= (\beta \mathbf{e}_2 + \gamma \mathbf{e}_3) \cdot \mathbf{e}_z \\ &= \beta (\mathbf{m}_0 \times \mathbf{e}_z) \cdot \mathbf{e}_z + \gamma (\mathbf{m}_0 \times (\mathbf{m}_0 \times \mathbf{e}_z)) \cdot \mathbf{e}_z \\ &= \gamma (m_{z,0}^2 - 1) \end{aligned} \quad (5.17)$$

- For $k \neq 0$:

$$\mathbf{h}_{\text{eff},1} = Km_{z,1}\mathbf{e}_z - Jk^2\mathbf{m}_1$$

Therefore

$$\begin{aligned} \mathbf{e}_1 \times [\mathbf{h}_{\text{eff},1} + \Gamma\mathbf{e}_1 \times \mathbf{h}_{\text{eff},1}] &= Km_{z,1}(\mathbf{e}_2 + \Gamma\mathbf{e}_3) - Jk^2[\mathbf{e}_1 \times \mathbf{m}_1 + \Gamma\mathbf{e}_1 \times (\mathbf{e}_1 \times \mathbf{m}_1)] \\ &= K\gamma(m_{z,0}^2 - 1)(\mathbf{e}_2 + \Gamma\mathbf{e}_3) - Jk^2[(-\gamma - \beta\Gamma)\mathbf{e}_2 - (\beta - \Gamma\gamma)\mathbf{e}_3] \end{aligned}$$

The two coupled equations for β and γ (5.16) can be written in matrix form as:

$$\begin{pmatrix} \dot{\beta} \\ \dot{\gamma} \end{pmatrix} = \underline{\underline{L}} \begin{pmatrix} \beta \\ \gamma \end{pmatrix}$$

where the matrix $\underline{\underline{L}}$ has the following form:

- For $k = 0$

$$\underline{\underline{L}} = \begin{pmatrix} -\Gamma(\mathbf{m}_0 \cdot \mathbf{h}_{\text{eff},0}) & -(B + a(m_{z,0}^2 - 1)) \\ B & -\Gamma(\mathbf{m}_0 \cdot \mathbf{h}_{\text{eff},0} + a(m_{z,0}^2 - 1)) \end{pmatrix}$$

- For $k \neq 0$

$$\underline{\underline{L}} = \begin{pmatrix} -\Gamma(\mathbf{m}_0 \cdot \mathbf{h}_{\text{eff},0} + Jk^2) & -(B + K(m_{z,0}^2 - 1) + Jk^2) \\ B + Jk^2 & -\Gamma(\mathbf{m}_0 \cdot \mathbf{h}_{\text{eff},0} + K(m_{z,0}^2 - 1) + Jk^2) \end{pmatrix}$$

If the real parts of both eigenvalues of these matrices are negative, \mathbf{m}_1 will die away in time and the solution \mathbf{m}_0 is stable to uniform and non-uniform perturbations, respectively. On the other hand, if the real part of one or more eigenvalues is positive, the perturbation \mathbf{m}_1 will be amplified in time and the solution \mathbf{m}_0 is unstable. For 2×2 matrices, demanding that both eigenvalues have negative real parts is equivalent to demanding that the trace of the matrix be negative and the determinant positive.

Stability to Uniform Perturbations

For each of the 4 fixpoints, we consider the trace and determinant of $\underline{\underline{L}}_{k=0}$ for different values of h . We have

$$Tr(\underline{\underline{L}}_{k=0}) = -2\Gamma(\mathbf{m}_0 \cdot \mathbf{h}_{\text{eff},0}) - \Gamma a(m_{z,0}^2 - 1) \quad (5.18)$$

$$Det(\underline{\underline{L}}_{k=0}) = \Gamma^2(\mathbf{m}_0 \cdot \mathbf{h}_{\text{eff},0})^2 + B^2 + (-\Gamma(\mathbf{m}_0 \cdot \mathbf{h}_{\text{eff},0}) + B) a(m_{z,0}^2 - 1) \quad (5.19)$$

From Figures 5.3 and 5.4 we see:

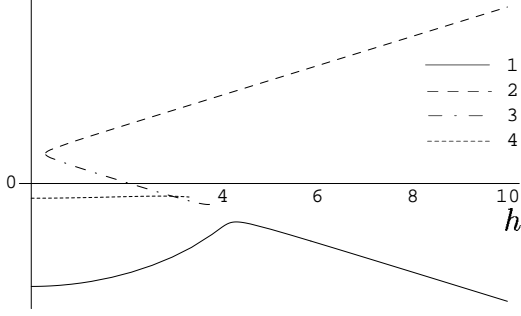


Figure 5.3: Plot of equation (5.18) (trace of the matrix $\underline{L}_{k=0}$) for each of the four fixpoints shown in Figure 5.1

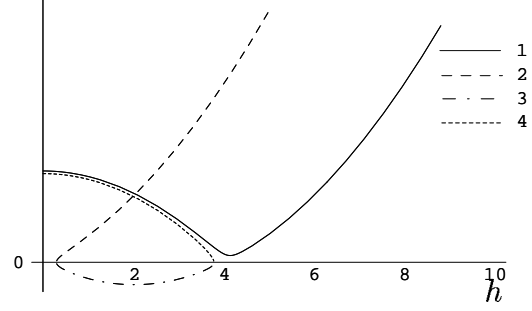


Figure 5.4: Plot of equation (5.19) (determinant of the matrix $\underline{L}_{k=0}$) for each of the four fixpoints shown in Figure 5.1

- Fixpoint 1: $Tr(\underline{L}_{k=0}) < 0$ and $Det(\underline{L}_{k=0}) > 0$ for all h
- Fixpoint 2: $Tr(\underline{L}_{k=0}) > 0$ for all h
- Fixpoint 3: $Det(\underline{L}_{k=0}) < 0$ for all h
- Fixpoint 4: $Tr(\underline{L}_{k=0}) < 0$ and $Det(\underline{L}_{k=0}) > 0$ for all h

Therefore, fixpoints 2 and 3 are unstable to homogeneous perturbations, while fixpoints 1 and 4 are stable to homogeneous perturbations.

Stability to Non-Uniform Perturbations

It remains to be seen whether the fixpoints 1 and 4 are stable to inhomogeneous perturbations. We consider initially the trace of the matrix $\underline{L}_{k \neq 0}$:

$$Tr(\underline{L}_{k \neq 0}) = -2\Gamma(\mathbf{m}_0 \cdot \mathbf{h}_{\text{eff},0}) - \Gamma K(m_{0z}^2 - 1) - 2\Gamma Jk^2 \quad (5.20)$$

This expression has its maximum value for $k \rightarrow 0$, and so we only need consider this case. A plot of (5.20) with $k \rightarrow 0$ vs. h is qualitatively the same as the trace plot in Figure 5.3 and so is not shown. Again the trace of $L_{k \neq 0}$ for $k \rightarrow 0$ is found to be negative for fixpoints 1 and 4, and so it is negative for all values of k , and the first criterion for stability is satisfied for both these fixpoints¹.

However it is the determinant of $L_{k \neq 0}$ which is of more interest:

$$Det(L_{k \neq 0}) = k^4 J^2 (1 + \Gamma^2) + k^2 J P + Q \quad (5.21)$$

¹For the record, the trace of $\underline{L}_{k \neq 0}$ for fixpoint 2 is again positive for all h as $k \rightarrow 0$, while $Tr(\underline{L}_{k \neq 0})$ for fixpoint 3 is positive for $h < 2.5$ and negative for $h > 2.5$, qualitatively the same as in Figure 5.3.

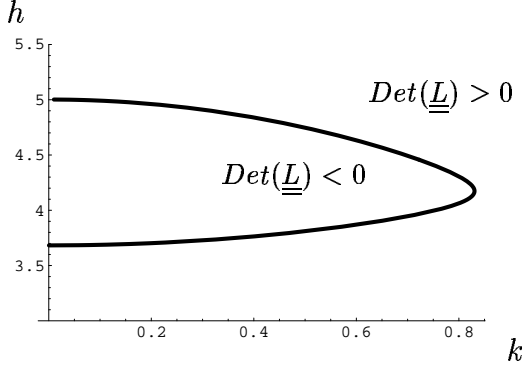


Figure 5.5: Plot of equation (5.22) for fixpoint 1 showing stable ($Det(L_{k \neq 0}) > 0$) and unstable ($Det(L_{k \neq 0}) < 0$) parameter regions

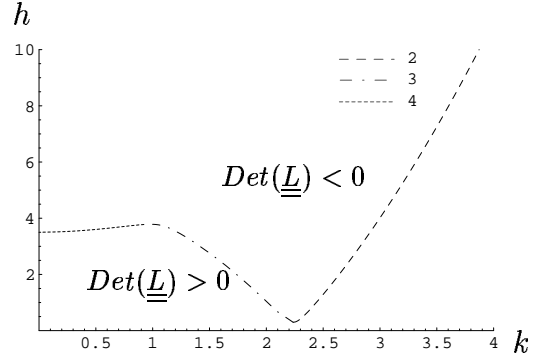


Figure 5.6: Plot of equation (5.22) for fixpoints 2, 3 and 4 showing stable ($Det(L_{k \neq 0}) > 0$) and unstable ($Det(L_{k \neq 0}) < 0$) parameter regions

where

$$P = 2B + K(m_{0z}^2 - 1) + \Gamma^2 (2(\mathbf{m}_0 \cdot \mathbf{h}_{\text{eff},0}) + K(m_{0z}^2 - 1))$$

$$Q = \Gamma^2 (\mathbf{m}_0 \cdot \mathbf{h}_{\text{eff},0})^2 + B^2 + K(m_{0z}^2 - 1) (\Gamma^2 (\mathbf{m}_0 \cdot \mathbf{h}_{\text{eff},0}) + B)$$

We are interested in values of k and h for which $Det(L_{k \neq 0}) = 0$. This curve separates the parameter regions where \mathbf{m}_0 is stable ($Det(L_{k \neq 0}) > 0$) from those where \mathbf{m}_0 is unstable ($Det(L_{k \neq 0}) < 0$) and is given by:

$$k^2 = \frac{-JP \pm \sqrt{J^2 P^2 - 4QJ^2(1 + \Gamma^2)}}{2J^2(1 + \Gamma^2)} . \quad (5.22)$$

The plot of this curve in the (h, k) plane is shown in Figures 5.5 and 5.6.

Fixpoint 1 is initially considered separately from the rest, as the solution curve (see Figure 5.1) is disjoint from that of the other three fixpoints. The regions of negative and positive determinant (unstable and stable regions respectively) are shown in Figure 5.5. We see that as we increase h from zero, or decrease h from large values, the mode which first becomes unstable is the $k \rightarrow 0$ mode.

For fixpoints 2, 3 and 4, which form one single curve in Figure 5.1, the corresponding regions are shown in Figure 5.6. Here we see, as we increase h from zero, it is fixpoints 2 and 3 which become unstable, precisely at the point h_{sn1} where they appear, i.e. fixpoints 2 and 3 are unstable to both homogeneous and inhomogeneous perturbations for all values of h . The appearance of fixpoints 2 and 3 at h_{sn1} is associated with an instability to inhomogeneous perturbations with a wave number around $k \approx 2.3$.

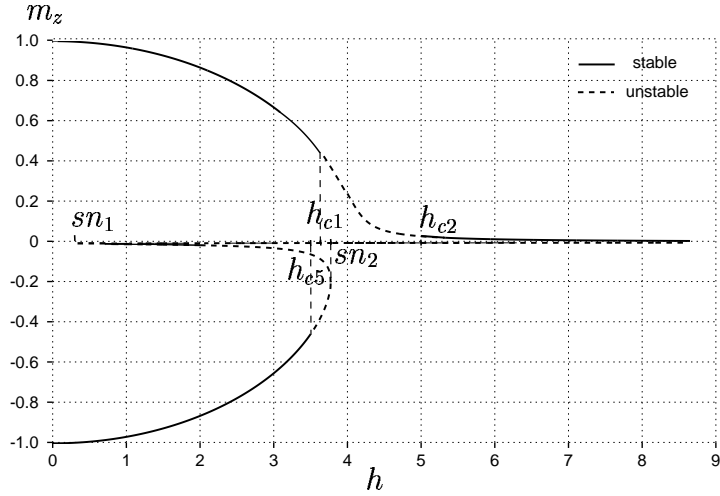


Figure 5.7: Summary of the stability of homogeneous solutions to the Landau-Lifshitz equation. The full line indicates fixpoint solutions that are stable, the dashed line those that are unstable. Fixpoint 1 is unstable to non-uniform perturbations between $h_{c1} = 3.682$ and $h_{c2} = 5.002$; fixpoints 2 and 3 are unstable to uniform and non-uniform perturbations for all values of h at which they exist; fixpoint 4 is unstable to non-uniform perturbations between $h_{c5} = 3.503$ and the point it ceases to exist $h_{sn2} = 3.785$

Further increasing h we see that fixpoint 4 becomes unstable at $k \rightarrow 0$. The critical h at which fixpoint 4 becomes unstable is denoted h_{c5} . Fixpoint 4 then remains unstable for the rest of its existence until the solution itself vanishes at h_{sn2} .

We can use (5.22) to calculate the precise values of h at which fixpoints 1 and 4 become unstable. We have seen above that this occurs for inhomogeneous perturbations with $k \rightarrow 0$. So we set (5.22) to zero and look for values of m_z where

$$P - \sqrt{P^2 - 4Q(1 + \Gamma^2)} = 0 \quad (5.23)$$

For the fixed parameter values H, K, ω used in simulations, this yields three solutions: $m_z = (-0.4604; 0.02984; 0.4306)$. These can be translated into critical h values using (5.9), and we obtain: $h_{c1} = 3.682$, $h_{c2} = 5.002$, $h_{c5} = 3.504$.

Figure 5.1 may now be supplemented to include the three critical h values and the two turning points computed above. The results are shown in Figure 5.7. Note now that the dashed line indicates an unstable solution (to either uniform or nonuniform disturbances) while the full line indicates a stable solution.

Chapter 6

Domain Features far from the Wall

In Chapter 5 we saw that there is a region in parameter space (between h_{c1} and h_{c2}) where no steady state homogeneous solutions are found. We are interested in what other solutions are to be found in this region. The numerical results indicate the presence of dynamic domains, and motivated by these we make a simple approach to solving the equations of motion far from the wall, at this point entirely neglecting the structure of the wall itself.

6.1 Magnetization far from the Wall

The name *domain* itself indicates that the that the structure can be thought of as two locally homogeneous regions separated by a wall where the magnetization distribution is non-uniform. In this chapter we consider only the magnetization within the domains themselves a considerable distance away from the domain walls. This is equivalent to assuming that the width of the wall is infinitesimally thin. Hence we can write down the magnetization in the probe as [Fles]

$$\mathbf{m}(\xi) = \begin{cases} \mathbf{m}^{(1)} & 0 < \xi < 2Lq \\ \mathbf{m}^{(2)} & 2Lq < \xi < 2L(1 - q) \end{cases} \quad (6.1)$$

The magnetization is in the state $\mathbf{m}^{(1)}$ in the first domain and $\mathbf{m}^{(2)}$ in the second domain, and there is a discontinuous jump between these results at the “wall”. We have introduced the quantity q to describe the proportion of the probe in each domain. $2Lq$ is the amount of the probe in state 1, while $2L(1 - q)$ of the probe is in state 2 (where the length over which the pattern repeats itself is $2L$). For stripe domain patterns such as examples **b**, **c**, or **d** in Figure 4.2, ξ is a Cartesian

coordinate. (In circular domain patterns such as \mathbf{a} , \mathbf{e} or \mathbf{f} , with some redefinition of the length L , ξ is the radial coordinate.)

As the Landau-Lifshitz equation must hold throughout the probe, so it must also hold within each locally homogeneous domain i ($i = 1, 2$). Thus in each domain i we require that the spatial inhomogeneity vanishes, and that a steady state solution be found:

$$\partial_t \mathbf{m}^{(i)} = 0 \quad , \quad \nabla^2 \mathbf{m}^{(i)} = 0 \quad , \quad \text{for } i = 1, 2 \quad . \quad (6.2)$$

We follow the same approach as used in Section 5.1 (see equation (5.2)). Inserting the conditions that the magnetization within each dynamic domain be locally homogeneous and in the steady state in the rotating reference frame, we write down the Landau-Lifshitz equation in each of the two domains as

$$-\mathbf{h}_{\text{eff}}^{(i)} + \frac{\omega}{1 + \Gamma^2} \mathbf{e}_z - \frac{\Gamma\omega}{1 + \Gamma^2} \mathbf{m}^{(i)} \times \mathbf{e}_z = \mu^{(i)} \mathbf{m}^{(i)} \quad (6.3)$$

with

$$\mathbf{h}_{\text{eff}}^{(i)} = H \mathbf{e}_z + h \mathbf{e}_x - \overline{m}_z \mathbf{e}_z + K m_z^{(i)} \mathbf{e}_z$$

where the $\mu^{(i)}$ are unknown.

These two equations for $\mathbf{m}^{(1)}$ and $\mathbf{m}^{(2)}$ are not independent, but rather are coupled via the demagnetizing term \overline{m}_z which holds for the entire probe and appears in each effective field $\mathbf{h}_{\text{eff}}^{(i)}$. Using the ansatz (6.1) we can write down the demagnetizing term as

$$\begin{aligned} \overline{m}_z &= \frac{1}{2L} \int_0^{2L} m_z(\xi) d\xi \\ &= q m_z^{(1)} + (1 - q) m_z^{(2)} \end{aligned} \quad (6.4)$$

A further ansatz still needs to be made to obtain domain solutions, and to obtain this we look at some typical numerical results as shown in Figure 4.6. It is seen that the m_x and m_y values in domains 1 and 2 are the same, i.e. $m_x^{(1)} = m_x^{(2)}$ and $m_y^{(1)} = m_y^{(2)}$. Equally we can see that $m_z^{(1)} = -m_z^{(2)}$ ¹:

$$\begin{aligned} m_x^{(1)} &= m_x^{(2)} & =: m_x \\ m_y^{(1)} &= m_y^{(2)} & =: m_y \\ m_z^{(1)} &= -m_z^{(2)} \end{aligned} \quad (6.5)$$

¹This is a symmetry that is not present in the equations of motion, and is wholly motivated by the numerical simulations. Although this symmetry is only explicitly shown in Figure 4.6 for the cases $h = 0.2$ and $h = 3$, the following is true for all domain solutions numerically found (see the numerical results in Figure 9.4 for many other values of h)

Therefore from (6.4), $\bar{m}_z = m_z^{(1)}(2q - 1)$. All this can be inserted into (6.3) for each domain (i), which in component form read:

$$\gamma m_y + \mu^{(i)} m_x = -h \quad (6.6a)$$

$$-\gamma m_x + \mu^{(i)} m_y = 0 \quad (6.6b)$$

$$(K + \mu^{(i)}) m_z^{(i)} = -(\delta - \bar{m}_z) \quad (6.6c)$$

with δ and γ from (5.4):

$$\delta = H - \frac{\omega}{1 + \Gamma^2} \quad \text{and} \quad \gamma = \frac{\Gamma\omega}{1 + \Gamma^2}$$

We can obtain two equations that do not contain the unknown expressions $\mu^{(i)}$ as follows:

$$(6.6a) \cdot m_y - (6.6b) \cdot m_x \rightarrow \gamma(m_x^2 + m_y^2) = -hm_y \quad (6.7)$$

$$(6.6b) \cdot m_z^{(i)} - (6.6c) \cdot m_y \rightarrow -\gamma m_x m_z^{(i)} - K m_y m_z^{(i)} = (\delta - \bar{m}_z) m_y \quad (6.8)$$

Inserting $i = 1, 2$ respectively, equation (6.8) yields

$$-\gamma m_x m_z^{(1)} - K m_y m_z^{(1)} = (\delta - \bar{m}_z) m_y \quad (6.9a)$$

$$\gamma m_x m_z^{(1)} + K m_y m_z^{(1)} = (\delta - \bar{m}_z) m_y \quad (6.9b)$$

In order that (6.9a) and (6.9b) can be simultaneously satisfied, either $m_y = 0$ (but we know this not to be true, from the numerical results in Figure 4.6, for example) or

$$\delta = H - \frac{\omega}{1 + \Gamma^2} = \bar{m}_z \quad (6.10)$$

Thus the demagnetizing field is equal exactly to the detuning effect. Consider the Landau-Lifshitz equation in Gilbert form in the rotating reference field (2.7). We note that the effective *internal* field in the \mathbf{e}_z direction is $H - \bar{m}_z - \frac{\omega}{1 + \Gamma^2}$ which is precisely equal to zero. (Compare the steady state Bloch wall solution ($h = 0$) where the effective internal field is $H - \bar{m}_z = 0$. This is discussed in more detail in Appendix C.)

Inserting $\delta = \bar{m}_z$ into (6.4) and sorting for q we obtain

$$q = \frac{1}{2} \left(\frac{\delta}{m_z^{(1)}} + 1 \right) \quad (6.11)$$

To find $m_z^{(i)}$ we note that with (6.10) the effective field in each domain i is now

$$\mathbf{h}_{\text{eff}}^{(i)} = (H - \delta) \mathbf{e}_z + h \mathbf{e}_x + K m_z^{(i)} \mathbf{e}_z \quad (6.12)$$

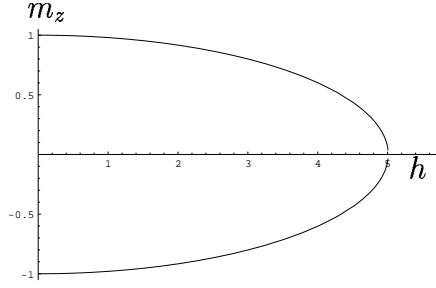


Figure 6.1: The z -component of the magnetization within each domain as calculated from (6.14). The parameter values $K = 5$, $H = \omega = 3$ have been selected

Comparing equation (6.12) with (5.1), we see that all results from the homogeneous calculation in Section 5.1 can now be applied, providing H is replaced by $H - \delta$ (thus δ is replaced by $(H - \delta) - \frac{\omega}{1+\Gamma^2} = 0$) and a by K . Equation (5.8) then becomes

$$m_z^{(i)4} (K^2 + \gamma^2) + m_z^{(i)2} (h^2 - K^2 - \gamma^2) = 0 \quad (6.13)$$

Taking the two non-zero fixpoints of (6.13) to be those which we are looking for, the solutions of interest are:

$$m_z^{(1)} = +\sqrt{1 - \frac{h^2}{K^2 + \gamma^2}} \quad m_z^{(2)} = -\sqrt{1 - \frac{h^2}{K^2 + \gamma^2}} \quad (6.14)$$

In addition, we note that equation (6.8) for $\delta = \overline{m}_z$ now yields a relation between m_x and m_y :

$$\frac{m_y}{m_x} = -\frac{\gamma}{K}$$

This, together with the condition $|\mathbf{m}| = 1$ and (6.14), can be used to work out m_x and m_y :

$$\begin{aligned} m_x &= \frac{K}{h} (1 - m_z^2) = \frac{hK}{K^2 + \gamma^2} \\ m_y &= -\frac{\gamma}{h} (1 - m_z^2) = -\frac{\gamma h}{K^2 + \gamma^2} \end{aligned} \quad (6.15)$$

Figure 6.1 shows values of $m_z^{(1)}$ and $m_z^{(2)}$ for different values of h , and for the parameter set $K = 5$, $H = \omega = 3$. We note that according to solution (6.14), the domain solution only exists for $h < \sqrt{K^2 + \gamma^2}$, which is the value 5.0073 in Figure 6.1. This places an upper bound on the dynamical domain solutions determined with this simple ansatz.

6.2 Linear Stability Analysis

Now, motivated by the numerical solutions, we had also hoped to find a lower bound for dynamical domain solutions. The simple ansatz (6.1) does not deliver us a lower bound for existence. We saw in Section 4.5 that it appears that the lower bound h_{c3} , below which numerical dynamic domains are not found, is determined from a stability criterion. It is the aim of the following section to determine this lower critical value of h . We recall that the ansatz (6.1) does *not* describe an entire dynamic domain, only that part far from the domain wall. Therefore any criteria for stability determined in performing a linear stability analysis on (6.1) will be only *necessary* conditions for stability, and not *sufficient* conditions.

To determine where (6.1) is stable, we add a small perturbation to the basic solution $\mathbf{m}_0^{(i)}$ in each domain i . As usual, the basic solution is now given the subscript 0, and the small perturbation the subscript 1. Initially this local stability analysis follows closely the procedure in Section 5.2. The basic ansatz now becomes

$$\mathbf{m}^{(i)}(\xi, t) = \mathbf{m}_0^{(i)} + \varepsilon \mathbf{m}_1^{(i)}(\xi, t) \quad i = 1, 2 \quad (6.16)$$

where, as before in the homogeneous case

$$\mathbf{m}_0^{(i)} \cdot \mathbf{m}_1^{(i)} = 0 \quad .$$

Using (6.10) and (6.16), the demagnetizing field is now:

$$\begin{aligned} \bar{m}_z &= qm_z^{(1)} + (1 - q)m_z^{(2)} \\ &= qm_{z,0}^{(1)} + (1 - q)m_{z,0}^{(2)} + \varepsilon(qm_{z,1}^{(1)} + (1 - q)m_{z,1}^{(2)}) \\ &= \delta + \varepsilon(qm_{z,1}^{(1)} + (1 - q)m_{z,1}^{(2)}) \\ &=: (\bar{m}_z)_0 + \varepsilon(\bar{m}_z)_1 \end{aligned}$$

We insert this into the Landau-Lifshitz equation (2.5) for each domain and expand to order ε . To order $O(\varepsilon)$ the linearized equation (equivalent to (5.14) in the homogeneous case) for each domain i is:

$$-\dot{\mathbf{m}}_1^{(i)} = B^{(i)} \mathbf{m}_1^{(i)} \times \mathbf{m}_0^{(i)} + \Gamma(\mathbf{m}_0^{(i)} \cdot \mathbf{h}_{\text{eff},0}^{(i)}) \mathbf{m}_1^{(i)} + \mathbf{m}_0^{(i)} \times \left[\mathbf{h}_{\text{eff},1}^{(i)} + \Gamma \mathbf{m}_0^{(i)} \times \mathbf{h}_{\text{eff},1}^{(i)} \right] \quad (6.17)$$

where

$$B^{(i)} := (\mathbf{m}_0^{(i)} \cdot \mathbf{h}_{\text{eff},0}^{(i)}) - \omega m_{z,0}^{(i)}$$

The effective field \mathbf{h}_{eff} to zeroth and first order is determined as:

$$\begin{aligned} \mathbf{h}_{\text{eff},0}^{(i)} &= (H - \delta) \mathbf{e}_z + h \mathbf{e}_x + K m_{z,0}^{(i)} \mathbf{e}_z \\ \mathbf{h}_{\text{eff},1}^{(i)} &= J \frac{\partial^2 \mathbf{m}_{z,1}^{(i)}}{\partial \xi^2} + K m_{z,1}^{(i)} \mathbf{e}_z - (\bar{m}_z)_1 \mathbf{e}_z \end{aligned}$$

As before $\mathbf{m}_0^{(i)} \perp \mathbf{m}_1^{(i)}$ and we can choose an orthogonal coordinate system in each domain defined by

$$\begin{aligned}\mathbf{e}_1^{(i)} &= \mathbf{m}_0^{(i)} \\ \mathbf{e}_2^{(i)} &= \mathbf{m}_0^{(i)} \times \mathbf{e}_z \\ \mathbf{e}_3^{(i)} &= \mathbf{m}_0^{(i)} \times (\mathbf{m}_0^{(i)} \times \mathbf{e}_z)\end{aligned}$$

and so write

$$\mathbf{m}_1^{(i)}(\xi, t) = \beta(\xi, t)^{(i)} \mathbf{e}_2^{(i)} + \gamma(\xi, t)^{(i)} \mathbf{e}_3^{(i)}$$

The linearized Landau-Lifshitz equation (6.17) is written down for each domain in its special coordinate system, leading to a system of 2 equations for each $(\beta^{(i)}, \gamma^{(i)})$:

$$\begin{aligned}-\dot{\beta}^{(i)} \mathbf{e}_2^{(i)} - \dot{\gamma}^{(i)} \mathbf{e}_3^{(i)} &= \\ B^{(i)}(-\beta^{(i)} \mathbf{e}_3^{(i)} + \gamma^{(i)} \mathbf{e}_2^{(i)}) + \Gamma(\mathbf{m}_0^{(i)} \cdot \mathbf{h}_{\text{eff},0}^{(i)}) &(\beta^{(i)} \mathbf{e}_2^{(i)} + \gamma^{(i)} \mathbf{e}_3^{(i)}) \\ &+ [K(m_{z,0}^2 - 1)\gamma^{(i)} - (\overline{m}_z)_1] (\mathbf{e}_2^{(i)} + \Gamma \mathbf{e}_3^{(i)}) \\ &+ J [\beta''^{(i)} (\mathbf{e}_3^{(i)} - \Gamma \mathbf{e}_2^{(i)}) + \gamma''^{(i)} (-\mathbf{e}_2^{(i)} - \Gamma \mathbf{e}_3^{(i)})]\end{aligned}\tag{6.18}$$

where we have used the fact from (5.17) that $m_{z,1}^{(i)} = \gamma^{(i)}(m_{z,0}^2 - 1)$.

Now the term $(\overline{m}_z)_1$ is the same in both sets of two equations and hence couples all four equations together. Also using (5.17) it has the form:

$$(\overline{m}_z)_1 = (m_{z,0}^2 - 1) (q\gamma^{(1)} + (1 - q)\gamma^{(2)})$$

Again we discuss the cases of homogeneous ($k = 0$) and inhomogeneous ($k \neq 0$) perturbations separately.

Uniform Perturbations

We wish to consider the stability of the domain solution (6.14) and (6.15) to uniform perturbations, i.e. we consider the case $\beta^{(i)} \equiv \beta^{(i)}(t)$ and $\gamma^{(i)} \equiv \gamma^{(i)}(t)$. The linearized Landau-Lifshitz equation (6.17) written down for both domains becomes a system of four coupled *ordinary* linear differential equations as follows:

$$\begin{pmatrix} \dot{\beta}^{(1)} \\ \dot{\gamma}^{(1)} \\ \dot{\beta}^{(2)} \\ \dot{\gamma}^{(2)} \end{pmatrix} = \underline{\underline{L}} \begin{pmatrix} \beta^{(1)} \\ \gamma^{(1)} \\ \beta^{(2)} \\ \gamma^{(2)} \end{pmatrix}$$

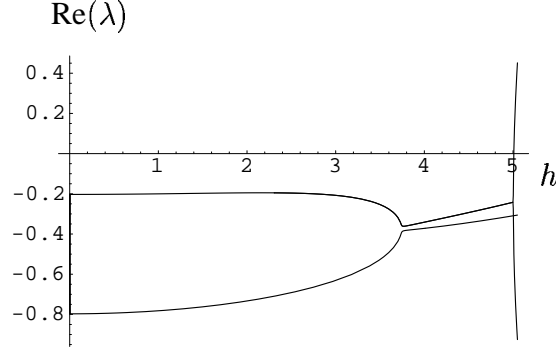


Figure 6.2: Real parts of the eigenvalues of $\underline{\underline{L}}$ vs. h for uniform perturbations. All $\text{Re}(\lambda_i) < 0$ for $i = 1, \dots, 4$ (two complex conjugate pairs of eigenvalues) and so the domain solution $\mathbf{m}_0(\xi)$ is stable to uniform perturbations

where $\underline{\underline{L}}$ can be written as a sum of two matrices as follows:

$$\underline{\underline{L}} = \underline{\underline{L}}_A + \underline{\underline{L}}_B \quad (6.19)$$

$\underline{\underline{L}}_A$ is made up of two 2×2 blocks in the upper left and lower right corners:

$$\underline{\underline{L}}_A = \begin{pmatrix} \underline{\underline{L}}^{(1)} & 0 \\ 0 & \underline{\underline{L}}^{(2)} \end{pmatrix} \quad (6.20)$$

and, in analogy to the case where the stability of the homogeneous solution to uniform perturbations was investigated,

$$\underline{\underline{L}}^{(i)} = \begin{pmatrix} -\Gamma(\mathbf{m}_0^{(i)} \cdot \mathbf{h}_{\text{eff},0}^{(i)}) & -(B^{(i)} + K(m_{z,0}^2 - 1)) \\ B^{(i)} & -\Gamma(\mathbf{m}_0^{(i)} \cdot \mathbf{h}_{\text{eff},0}^{(i)} + K(m_{z,0}^2 - 1)) \end{pmatrix} \quad i = 1, 2$$

The coupling between the domains by means of the demagnetizing field is to be found in $\underline{\underline{L}}_B$:

$$\underline{\underline{L}}_B = (m_{z,0}^2 - 1) \begin{pmatrix} 0 & q & 0 & (1 - q) \\ 0 & \Gamma q & 0 & \Gamma(1 - q) \\ 0 & q & 0 & (1 - q) \\ 0 & \Gamma q & 0 & \Gamma(1 - q) \end{pmatrix} \quad (6.21)$$

The eigenvalues of the matrix $\underline{\underline{L}}$ in (6.19) determine the stability of the basic solution $\mathbf{m}_0(\xi)$. If the real parts of all four eigenvalues are negative, $\mathbf{m}_0(\xi)$ is stable to (local) uniform perturbations.

The real parts of the four solutions to the quartic characteristic polynomial for the eigenvalues of $\underline{\underline{L}}$ are plotted against h in Figure 6.2. Here we see that for

$h < \sqrt{K^2 + \gamma^2} = 5.0073$, namely for all h where the domain solution $\mathbf{m}_0(\xi)$ in fact exists, $\text{Re}(\lambda_i) < 0$ for $i = 1, \dots, 4$. Thus $\mathbf{m}_0(\xi)$ is stable to uniform perturbations at all times. More precisely, there is *no* indication of the lower bound observed in numerical solutions.

Non-Uniform Perturbations

We now turn to more general inhomogeneous perturbations, i.e. we consider the case where $\beta^{(i)} \equiv \beta^{(i)}(\xi, t)$ and $\gamma^{(i)} \equiv \gamma^{(i)}(\xi, t)$. The linearized Landau-Lifshitz equation (6.17) written down for both domains becomes a system of four coupled *partial* linear differential equations as follows:

$$\begin{pmatrix} \dot{\beta}^{(1)} \\ \dot{\gamma}^{(1)} \\ \dot{\beta}^{(2)} \\ \dot{\gamma}^{(2)} \end{pmatrix} = \underline{\underline{L}} \begin{pmatrix} \beta^{(1)} \\ \gamma^{(1)} \\ \beta^{(2)} \\ \gamma^{(2)} \end{pmatrix}$$

where $\underline{\underline{L}}$ can again be written as a sum of two matrices:

$$\underline{\underline{L}} = \underline{\underline{L}}_A + \underline{\underline{L}}_B \quad (6.22)$$

As in (6.20), $\underline{\underline{L}}_A$ is again made up of two 2×2 blocks in the upper left and lower right corners, $\underline{\underline{L}}^{(1)}$ and $\underline{\underline{L}}^{(2)}$ respectively, now with

$$\underline{\underline{L}}^{(i)} = \begin{pmatrix} -\Gamma \left(\mathbf{m}_0^{(i)} \cdot \mathbf{h}_{\text{eff},0}^{(i)} - J \frac{\partial^2}{\partial \xi^2} \right) & - \left(B^{(i)} + K(m_{z,0}^2 - 1) - J \frac{\partial^2}{\partial \xi^2} \right) \\ B^{(i)} - J \frac{\partial^2}{\partial \xi^2} & -\Gamma \left(\mathbf{m}_0^{(i)} \cdot \mathbf{h}_{\text{eff},0}^{(i)} + K(m_{z,0}^2 - 1) - J \frac{\partial^2}{\partial \xi^2} \right) \end{pmatrix}$$

for $i = 1, 2$. The matrix $\underline{\underline{L}}_B$ is again as in (6.21).

In the case where the stability of homogeneous basic solution to inhomogeneous perturbations was considered in the last chapter, we were able quite generally to consider one Fourier component of such an inhomogeneous perturbation. In this domain case, we would have to carry all Fourier modes through the calculation, as those in the first domain would necessarily be coupled to those in the second domain.

For this reason it seems more sensible to carry out the calculation numerically in real space rather than Fourier space. The spatial derivatives $\beta^{n(i)}$ and $\gamma^{n(i)}$ in (6.18) may then be replaced by finite difference expressions. The procedure is similar to that detailed in Appendix A where the stability of the numerical simulations was investigated, but in this present case the Laplace terms of the linearized Landau-Lifshitz equation (6.18) are considerably easier to compute because the set of basis vectors of the new coordinate system $\mathbf{e}_1^{(i)}, \mathbf{e}_2^{(i)}, \mathbf{e}_3^{(i)}$ in each domain is *not* spatially dependent.

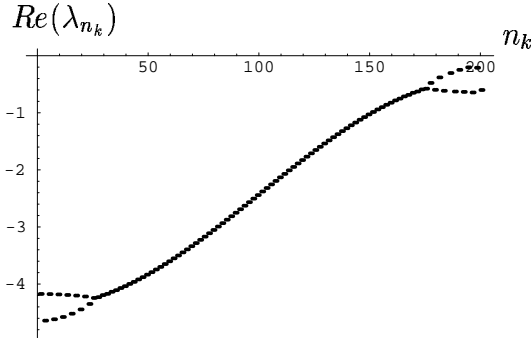


Figure 6.3: Real parts of the eigenvalue spectrum of \underline{L} describing non-uniform perturbations for a driving field of strength $h = 3$, where the equation of motion for the non-uniform perturbation has been discretized along $n = 100$ mesh points. As $\text{Re}(\lambda_{n_k}) < 0$ for all n_k , the domain solution $\mathbf{m}_0(\xi)$ in (6.1) is stable to non-uniform perturbations for $h = 3$

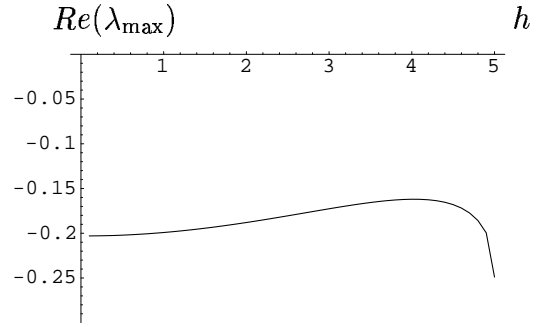


Figure 6.4: Largest real eigenvalue of all eigenvalue spectra as shown in Figure 6.3 for $0 \leq h < \sqrt{K^2 + \gamma^2} = 5.0073$. As $\text{Re}(\lambda_{\max}) < 0$ for all h , the domain solution $\mathbf{m}_0(\xi)$ in (6.1) is stable to non-uniform perturbations everywhere that it exists

We divide the length L over which the basic pattern repeats itself into n grid points. qn of these points are then given the basic solution $\mathbf{m}_0^{(1)}$, while $(1 - q)n$ points have the basic solution $\mathbf{m}_0^{(2)}$. Again we introduce a local coordinate system at each point j on the grid, and finally form a system of $2n$ coupled linear ordinary differential equations for $(\beta^{(j)}, \gamma^{(j)})$ where $j = 1 \dots n$. Also to be taken into account are the periodic boundary conditions of the problem, which of course also must hold for \mathbf{m}_1 . The $2n$ eigenvalues of the resulting $2n \times 2n$ matrix are investigated. Figure 6.3 shows as an example the eigenvalue spectrum of matrix \underline{L} for $n = 100$ and $h = 3$. (The $2n$ discrete eigenvalues $n_k = 1, \dots, 2n$ are ordered according to their magnitude. Thus n_k is some function of the wave number k , in which the characteristic k^2 spectrum can still be recognized.)

What is however of interest is the largest real part of the eigenvalues of \underline{L} (i.e. the eigenvalue whose real part is closest to zero, the “most dangerous” eigenvalue). This is shown in Figure 6.4 for all values of h , the driving field, where the domain solution as given by (6.1), (6.14) and (6.15) exists. We note first of all that the magnitude of the largest eigenvalue in Figure 6.4 for $h < \sqrt{K^2 + \gamma^2} = 5.0073$ is about 0.2, of the same order of magnitude as the largest eigenvalue in Figure 6.2.

Figure 6.4 may be compared to the right-hand side of Figure 4.10, where the equivalent calculation was performed on the numerical simulation results. We see some agreement between the behavior of the numerical solution and that of the ansatz (6.1) for large values of h , namely as we approach the upper boundary for existence, the solution becomes more stable. However there is great discrepancy

for small values of h . In fact there is absolutely *no* sign of the lower bound to stability when a small perturbation (uniform or non-uniform) is added to the magnetization within the domains as described by the ansatz (6.1).

Perturbations to Domain Wall Position

Now in Section 4.4 we discussed the nature of the transition at the lower bound h_{c3} . We saw that just below h_{c3} the two domain walls on either side of the “spin down” domain (that with negative m_z value) move towards each other. Eventually this lower domain is obliterated and only the “spin-up” domain remains as a homogenous stable solution. For this reason it would seem that a small shift in the position of the wall may be the trigger causing the domain state to become unstable at the lower critical value of h . As it may of course be a coupling of wall shift and change in magnetization which triggers the instability, it is necessary to carry both perturbations through the calculation.

While retaining the above local alterations in the magnetization, we add a small perturbation to the position of the wall Lq_0 as follows and extend the ansatz (6.16) as follows:

$$\begin{aligned} \mathbf{m}^{(i)} &= \mathbf{m}_0^{(i)} + \varepsilon \mathbf{m}_1^{(i)}(\xi) \quad i = 1, 2 \\ q &= q_0 + \varepsilon q_1 \end{aligned} \quad (6.23)$$

The changes to the equations describing the magnetization perturbation are only to be found within the demagnetizing term. It now becomes, to order ε

$$\begin{aligned} \bar{m}_z &= qm_z^{(1)} + (1 - q)m_z^{(2)} \\ &= \delta + \varepsilon \left(q_0 m_{z,1}^{(1)} + (1 - q_0) m_{z,1}^{(2)} + 2q_1 m_{z,0}^{(1)} \right) =: (\bar{m}_z)_0 + \varepsilon (\bar{m}_z)_1 \end{aligned} \quad (6.24)$$

The linearized Landau-Lifshitz equation now contains five variables, namely $(\beta^{(1)}, \gamma^{(1)}, \beta^{(2)}, \gamma^{(2)}, q_1)$. Therefore, in addition to the two vectorial equations (6.18), we still need a further equation describing the time development of q_1 to close the system. To find this we make use of the Heaviside step function $\theta(\xi)$ and write the domain solution as follows

$$\mathbf{m} = \mathbf{m}^{(1)}\theta(-\xi + Lq) + \mathbf{m}^{(2)}\theta(\xi - Lq) \quad (6.25)$$

Thus, retaining only terms to order $O(\varepsilon)$, we have:

$$\begin{aligned} \mathbf{m} &= (\mathbf{m}_0^{(1)} + \varepsilon \mathbf{m}_1^{(1)})\theta(-\xi + Lq_0 + \varepsilon Lq_1) + (\mathbf{m}_0^{(2)} + \varepsilon \mathbf{m}_1^{(2)})\theta(\xi - Lq_0 - \varepsilon Lq_1) \\ &= \mathbf{m}_0^{(1)}\theta(-\xi + Lq_0) + \mathbf{m}_0^{(2)}\theta(\xi - Lq_0) \\ &\quad + \varepsilon \left(\mathbf{m}_1^{(1)}\theta(-\xi + Lq_0) + \mathbf{m}_1^{(2)}\theta(\xi - Lq_0) + 2m_{z,0}^{(1)}Lq_1\delta(\xi - Lq_0)\mathbf{e}_z \right) \\ &=: \mathbf{m}_0 + \varepsilon \mathbf{m}_1 \end{aligned}$$

Thus inserting (6.23) into (2.5) and retaining only terms to order $O(\varepsilon)$, we obtain the linearized Landau-Lifshitz equation in the form (5.14), where the effective fields now read:

$$\begin{aligned}\mathbf{h}_{\text{eff},0} &= h \mathbf{e}_x + (H - (\overline{m}_z)_0) \mathbf{e}_z + K m_{z,0} \mathbf{e}_z + J \mathbf{m}_0'' \\ \mathbf{h}_{\text{eff},1} &= -(\overline{m}_z)_1 + K m_{z,1} \mathbf{e}_z + J \mathbf{m}_1''\end{aligned}$$

with the demagnetizing field \overline{m}_z as in (6.24).

In order to get an equation of motion for q , we integrate (5.14) over a small section of the probe containing the wall from $\xi = Lq_0 - \bar{\varepsilon}$ to $\xi = Lq_0 + \bar{\varepsilon}$, and then let the size of this section go to zero:

$$\lim_{\bar{\varepsilon} \rightarrow 0} \int_{Lq_0 - \bar{\varepsilon}}^{Lq_0 + \bar{\varepsilon}} \dots d\xi \quad (6.26)$$

When this procedure is carried out, only those terms in (5.14) containing a delta function will remain, and all others will vanish. We also assume that perturbations in the magnetization are *smooth* close to the wall, i.e. that terms of the form $\frac{\partial \mathbf{m}_1^{(1)}}{\partial \xi} \delta(\xi - Lq_0)$ and $\mathbf{m}_1^{(1)}(\xi) \delta'(\xi - Lq_0)$ that appear in the first-order exchange term (second spatial derivative) all yield zero after carrying out the integration (6.26).

The application of integral (6.26) to each term in (5.14) is given in Appendix B and we obtain, in component form:

$$\begin{aligned}-2m_{z,0}^{(1)} \dot{q}_1 \mathbf{e}_z &= (hm_{x,0} + Km_{z,0}^2) q_1 \left(-2m_{y,0} m_{z,0}^{(1)} \mathbf{e}_x + 2m_{x,0} m_{z,0}^{(1)} \mathbf{e}_y \right) \\ &\quad + \Gamma (hm_{x,0} + Km_{z,0}^2) q_1 2m_{z,0}^{(1)} \mathbf{e}_z \\ &\quad + Km_{z,0}^{(1)} q_1 (2m_{y,0} \mathbf{e}_x - 2m_{x,0} \mathbf{e}_y - 2\Gamma(m_{x,0}^2 + m_{y,0}^2) \mathbf{e}_z)\end{aligned} \quad (6.27)$$

In the x and y directions equation (6.27) yields the same requirements, namely that

$$\begin{aligned}0 &= - (hm_{x,0} + Km_{z,0}^2) K \\ &\rightarrow m_{x,0} = \frac{K}{h} (1 - m_{z,0}^2)\end{aligned}$$

This is of course merely the solution function for $m_{x,0}$, already found in equation (6.15).

In the z direction, we can divide both sides by $2m_{z,0}^{(1)}$ and obtain

$$\begin{aligned}q_1 &= -K (1 - \Gamma(1 - m_{z,0}^2)) q_1 \\ &=: -Q q_1 \\ &\rightarrow q_1(t) = A e^{-Qt}\end{aligned}$$

where $Q > 0$ for all $m_{z,0}$. Therefore a small perturbation to the position of the wall q_1 will always die away in time, and the ground solution remains stable to such perturbations.

We note that equation (6.27) does not indeed contain \mathbf{m}_1 . Therefore the wall shift q_1 is decoupled from any shift in the magnetization \mathbf{m}_1 , and so an eigenvalue spectrum such as that shown in Figure 6.3 will merely be extended by a further single eigenvalue $-Q$. As $-1 < m_{z,0} < +1$, the order of magnitude of Q is the order of magnitude of K ($= 5$ for plots shown). The single additional eigenvalue of the extended linear matrix \underline{L} is therefore one of the smallest (most negative) eigenvalues in an extended Figure 6.3, and so there is no change in Figure 6.4. Therefore a shift in the domain wall position q_1 has *no effect* on the overall stability of the domain solution as represented by (6.1).

In conclusion, this chapter examined whether the simple ansatz (6.1) was sufficient to reproduce and understand the behavior of dynamical domains as motivated by numerical simulations. To one end we were successful: we obtained an upper bound for existence of dynamical domain solutions. However, the lower bound remains elusive. Although it was expected that ansatz (6.1) would in fact be more successful for small values of h (where the domain wall is very narrow compared the size of the probe), neither uniform nor non-uniform perturbations to the magnetization within the domains, nor perturbations to the wall position, gave any indication of a lower stability bound.

Thus, the simple ansatz (6.1) yielded only *necessary* conditions that must be satisfied for dynamic domains to exist. *Sufficient* conditions could only be calculated by means of a linear stability analysis if we had a full analytic description of the domain solution. The main difference between the numerical dynamical domains and ansatz (6.1) is that the wall has been entirely neglected, and it seems clear that the structure of the wall must play a role in determining the lower stability bound. Including the wall structure brings us one step closer to a complete description of the domain solution and will be discussed in the following chapters.

Chapter 7

Dynamic Domain Wall Structure

In this chapter we present a more realistic picture of dynamic domains. Motivated by the chapter on numerical results, we realize that the walls between the domains also play an important role in determining the stability of a dynamic domain. In particular, at the end of Section 4.4 we noted how the walls move towards each other and how the spins within the walls rotate faster and faster out of phase with the rest of the probe as a critical threshold in the driving field amplitude h_{c3} is passed. In Section 6.2 we saw that merely connecting two coexisting spatially uniform solutions by a discontinuous jump and allowing this junction to travel through the probe delivered no new results with respect to limits of stability of dynamic domain solutions. In this chapter, therefore, we propose to determine the structure of the walls between dynamic domains.

To work out the wall structure we need to include the full spatial dependence in the Landau-Lifshitz equation. For simplicity, we rescale the dimensionless unit of length used in the system, the width of the static Bloch wall, redefining it as

$$\sqrt{\frac{J}{K}} := 1$$

This is equivalent to setting the exchange coefficient equal to the anisotropy coefficient ($J = K$) in the Landau-Lifshitz equation.

As the magnitude of the magnetization $|\mathbf{m}|$ is of constant length one throughout the motion, the three components of the magnetization m_x, m_y, m_z are of course not independent of each other, and so it can be better parameterized using *two* independent variables. For reasons explained at the end of Section 7.1, we select as our two variables u and φ defined as follows [Helm]:

$$\begin{aligned} m_x &= \cos \varphi \operatorname{sech} u \\ m_y &= \sin \varphi \operatorname{sech} u \\ m_z &= \tanh u \end{aligned} \tag{7.1}$$

7.1 Planar Domain Walls without Damping

At this point we restrict ourselves to planar (stripe) solutions, i.e. the magnetization $\mathbf{m}(\xi)$ is dependent on one Cartesian coordinate ξ . This affects the calculation in that the exchange term in the Landau-Lifshitz equation becomes:

$$\nabla^2 \mathbf{m} = \frac{\partial^2 \mathbf{m}(\xi)}{\partial \xi^2}$$

The Landau-Lifshitz-Gilbert equation in the rotating reference frame (2.7) with (2.6) now has the form [Helm]

$$\begin{aligned} \dot{u} &= -F + \Gamma G \\ \dot{\varphi} &= \Gamma F + G \end{aligned} \quad (7.2)$$

where

$$\begin{aligned} F &= -\gamma - h \cosh u \sin \varphi + K [\varphi'' - 2 \tanh u u' \varphi'] \\ G &= (\delta - \bar{m}_z) - h \sinh u \cos \varphi + K \tanh u + K [u'' - \tanh u ((u')^2 - (\varphi')^2)] \end{aligned} \quad (7.3)$$

and δ and γ as defined in (5.4). Steady solutions to this set of equations satisfy $\partial_t u = 0$ and $\partial_t \varphi = 0$, i.e. $F = 0$ and $G = 0$.

Now there is no simple method of determining a closed solution when the wall is described by two independent variables [Hube]. However, we note that when $\gamma = 0$, the equation $F = 0$ is easily solved by $\varphi = \text{const} = 0$. Then the equation $G = 0$ becomes

$$G = (\delta - \bar{m}_z) - h \sinh u + K \tanh u + K [u'' - \tanh u (u')^2] = 0 \quad (7.4)$$

If we take position of the wall to be such that the probe is in equilibrium, i.e. from (6.10) $\delta - \bar{m}_z = 0$, then u must be a solution of:

$$-u'' + \tanh u (u')^2 - \tanh u + \frac{h}{K} \sinh u = 0 \quad (7.5)$$

Now equation (7.5) can be integrated exactly as follows: we note that

$$\begin{aligned} [-\tanh u (u')^2 + u''] 2u' \operatorname{sech}^2 u &= \frac{\partial}{\partial \xi} (u' \operatorname{sech} u)^2 \\ \left[-\tanh u + \frac{h}{K} \sinh u \right] 2u' \operatorname{sech}^2 u &= \frac{\partial}{\partial \xi} \left(\operatorname{sech} u - \frac{h}{K} \right)^2 \end{aligned}$$

Thus multiplying (7.5) by $2u' \operatorname{sech}^2 u$, we can integrate the resulting expression from $\xi = -\infty$ (far to the left of the domain wall, where $u' = 0$ and $\operatorname{sech} u = m_x = h/K$) to ξ . We obtain

$$(u' \operatorname{sech} u)^2 = \left(\operatorname{sech} u - \frac{h}{K} \right)^2 \quad (7.6)$$

and taking the square root

$$u' = \pm \left(1 - \frac{h}{K} \cosh u \right) \quad (7.7)$$

This may again be integrated from the center of the wall ($\xi = u = 0$) to ξ :

$$\int_0^u \frac{d u}{1 - \frac{h}{K} \cosh u} = \pm \int_0^\xi d \xi$$

and so we obtain $\xi(u)$ [Grad]

$$\pm \xi = \frac{1}{\sqrt{1 - \frac{h^2}{K^2}}} \ln \frac{1 - \frac{h}{K} + \sqrt{1 - \frac{h^2}{K^2}} \tanh \frac{u}{2}}{1 - \frac{h}{K} - \sqrt{1 - \frac{h^2}{K^2}} \tanh \frac{u}{2}}$$

Inverting this leads to $u(\xi)$:

$$u^\pm(\xi) = 2 \operatorname{artanh} \left[\sqrt{\frac{K-h}{K+h}} \tanh \left(\pm \frac{1}{2} \sqrt{1 - \frac{h^2}{K^2}} \xi \right) \right] \quad (7.8)$$

The two signs (\pm) refer to oppositely orientated walls, the plus sign yielding a wall from a “spin-down” domain is on the left to a “spin-up” domain on the right, and vice versa for the minus sign. Clearly $u^+ = -u^-$ and so for the components of the magnetization

$$\begin{aligned} m_x^+ &= \operatorname{sech} u^+ = \operatorname{sech} u^- = m_x^- \\ m_z^+ &= \tanh u^+ = -\tanh u^- = -m_z^- \end{aligned}$$

We recall that the solution (7.8) required $\gamma = 0$, i.e. $\Gamma = 0$ or $\omega = 0$. In the case $\Gamma = 0$, (7.8) is a dynamic domain solution in the limiting case of no damping. For $\omega = 0$, it describes a *static* domain solution with a static field $h\mathbf{e}_x$ in the plane of the film. The equilibrium condition (6.10) is then $H = \overline{m}_z$. Taking the limit $h \rightarrow 0$ we obtain from (7.8):

$$u^\pm(\xi) = \pm \xi \quad (7.9)$$

This is the static Bloch wall solution and is a special case of the more general solution (7.8). The simplicity of solution (7.9) is the reason for the choice of parameterization (7.1).

7.2 Effect of Wall Curvature

We now consider the alteration to the above equations when bubble domains rather than stripe domains are considered. We look for cylindrically symmetric solutions to the Landau-Lifshitz equation, i.e. solutions where $\mathbf{m} = \mathbf{m}(\rho)$. Motivated by the numerical evidence (Figure 4.5) we assume that all the spins at the center of the steady state bubble domain wall are lined up in parallel, and so bubble domains also require only one parameter u to describe them, at least in the limiting case of no damping.

Therefore the second spatial derivative (from the Laplace term) that appears in equation (7.5) will be different, and the determining equation for steady state solutions now has the form:

$$-u'' - \frac{u'}{\rho} + \tanh u (u')^2 - \tanh u + \frac{h}{K} \sinh u = 0 \quad (7.10)$$

We again attempt to solve this equation by integration, as we did with (7.5) in the previous section. Noting that:

$$\left[-\tanh u (u')^2 + u'' + \frac{u'}{\rho} \right] 2\rho^2 u' \operatorname{sech}^2 u = \frac{\partial}{\partial \rho} (\rho u' \operatorname{sech} u)^2$$

we can multiply (7.10) by $2u'\rho^2 \operatorname{sech}^2 u$ and integrate with respect to ρ from zero (far to the left of the domain wall) to ρ :

$$(\rho u' \operatorname{sech} u)^2 = \int_0^\rho \tilde{\rho}^2 \frac{\partial}{\partial \tilde{\rho}} \left(\operatorname{sech} u - \frac{h}{K} \right)^2 d\tilde{\rho} \quad (7.11)$$

The integration boundaries are assumed to include the domain wall fully. However, unlike in equation (7.6), the right-hand side of (7.11) cannot be integrated exactly.

There is in fact no known exact solution of (7.10). Even for the case $h = 0$ many attempts have been made to construct solutions for the limiting cases where the radius of the bubble is much larger or much smaller than the width of the wall [Kose, IvSh] or to take into account the singularity at $\rho = 0$ [DeBo].

Equation (7.10) may of course be solved numerically. This yields numerous different solutions for $u(\rho)$ depending on the boundary conditions inserted. However we are only interested in those solutions which have a domain shape, i.e. those where u varies rapidly at the domain wall at $\rho = R$ and away from the wall is essentially constant. In particular, this assumes that the radius of the desired bubble solution is much larger than the width of the bubble wall:

$$R \gg 1$$

Thus the curvature of the wall is very small (the wall is almost planar), and the difference between the solution for cylindrical domain walls and that for planar domain walls will be of order $O(1/R)$. We can write:

$$u_{\text{bub}}(\rho - R) = u_0(\rho - R) + u_1(\rho - R) \quad (7.12)$$

where $u_0(\rho - R)$ is the planar domain wall solution from (7.8) and $u_1(\rho - R)$ is of the order of magnitude of $1/R$.

We can introduce a Cartesian coordinate ξ defined as follows:

$$\xi = \rho - R \quad \text{and therefore} \quad \frac{\partial}{\partial \rho} = \frac{\partial}{\partial \xi}$$

For the purposes of calculation, we can avoid the singularity at $\rho = 0$, and yet still completely cover the domain wall, if we assume that

$$|\xi| \leq |\xi_{\text{max}}| \quad \text{with} \quad |\xi_{\text{max}}| \ll R \quad (7.13)$$

In doing this we assume that the behavior of the probe far away from the wall has no effect on the structure of the domain wall. This is a reasonable assumption, as we saw in Chapter 6 that the magnetization far away from the domain wall has no effect on, in particular, the lower bound h_{c3} . Expanding in ξ/R

$$\frac{1}{\rho} = \frac{1}{R + \xi} = \frac{1}{R} - \frac{\xi}{R^2} + \frac{\xi^2}{R^3} + O\left(\frac{\xi^3}{R^4}\right) \quad (7.14)$$

We now insert expansions (7.12) and (7.14) into (7.4) with the modified Laplace term, and expand in orders of $1/R$. To zeroth order we again obtain (7.5) for u_0 . We bear in mind that the equilibrium condition $\delta = \overline{m}_z$ that held for planar walls will not necessarily hold for cylindrical walls. To this end we modify the demagnetizing term in our calculation as follows:

$$\overline{m}_z = (\overline{m}_z)_0 + (\overline{m}_z)_1 = \delta + (\overline{m}_z)_1$$

where $(\overline{m}_z)_1$ is a constant term of order $1/R$. To linear order in $1/R$, (7.4) with the Laplace term in cylindrical coordinates becomes

$$-u_1'' + 2u_0' \tanh u_0 u_1' + \left(\text{sech}^2 u_0 ((u_0')^2 - 1) + \frac{h}{K} \cosh u_0 \right) u_1 - \frac{u_0'}{R} + \frac{(\overline{m}_z)_1}{K} = 0$$

which yields, using (7.7)

$$\begin{aligned} -u_1'' + 2 \left(\tanh u_0^+ - \frac{h}{K} \sinh u_0^+ \right) u_1' + \left(-\frac{2h}{K} \text{sech} u_0^+ + \frac{h}{K} \cosh u_0^+ + \frac{h^2}{K^2} \right) u_1 \\ = \mp \frac{1}{R} \left(1 - \frac{h}{K} \cosh u_0^+ \right) - \frac{(\overline{m}_z)_1}{K} \end{aligned} \quad (7.15)$$

Equation (7.15) is an inhomogeneous linear differential equation in u_1 with non-constant coefficients. The boundary conditions needed to solve equation (7.15) are determined from the magnetization in the probe a long way from the domain wall. At a great distance from the domain wall, the magnetization in the probe should be homogeneous, i.e.

$$u_1'(\rho \ll R) = 0 \quad \text{and} \quad u_1'(\rho \gg R) = 0$$

Equation (7.15) may be solved numerically using *Mathematica* [Wolf]. Since we cannot set boundary conditions at infinity, we select two radii $R_1 < R < R_2$ and set the numerical boundary conditions to

$$u_1'(\rho = R_1) = 0 \quad \text{and} \quad u_1'(\rho = R_2) = 0$$

or

$$u_1'(\xi = R_1 - R) = 0 \quad \text{and} \quad u_1'(\xi = R_2 - R) = 0$$

R_1 and R_2 are chosen so that the numerical integration of the differential equation (7.15) takes place over a range that completely includes the domain wall structure.

When (7.15) is solved it will yield a solution for u_1 as a function of the (initially) unknown constant $(\overline{m}_z)_1$, i.e. $u_1 \equiv u_1(\xi, (\overline{m}_z)_1)$. Yet there is a direct functional relationship between $(\overline{m}_z)_1$ and u_1 , namely¹

$$(\overline{m}_z)_1 = \frac{1}{2L} \int_{-L}^L m_{z,1} d\xi = \frac{1}{2L} \int_{-L}^L u_1(\xi, (\overline{m}_z)_1) \operatorname{sech}^2 u_0(\xi) d\xi \quad (7.16)$$

The ultimate function $u_1(\xi)$ is determined so that the expression (7.16) is *self-consistent*.

The results obtained can be inserted into the linearized expression for the magnetization \mathbf{m} across the cylindrical bubble wall:

$$\begin{aligned} m_x &= \operatorname{sech} u_0 - u_1 \operatorname{sech} u_0 \tanh u_0 \\ m_y &= 0 \\ m_z &= \tanh u_0 + u_1 \operatorname{sech}^2 u_0 \end{aligned}$$

Thus the structure of planar and cylindrical domain walls differs by an amount of order $O(1/R)$. The x , y and z components of the magnetization across a “spin-up” bubble domain wall and a “spin-down” bubble domain wall are shown in Figures 7.1 and 7.2.

¹In determining this integral numerically, it must be ensured that L is large enough so that varying it slightly has no effect on the numerical value of the entire right-hand side of this expression, i.e. L is much larger than the width of the domain wall, yet $L \ll R$, as demanded by (7.13).

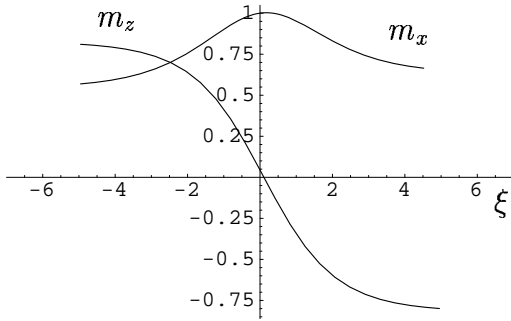


Figure 7.1: Assuming $\Gamma = 0$: Spatial variation of m_x and m_z components of the magnetization across a “spin-up” bubble wall for the case $h = 3$. $\xi = \rho - R$ is the direction normal to the plane of the wall. The radius of the bubble is $R = 10$. Equation (7.15) was integrated between $\rho = 5$ ($\xi = -5$) and $\rho = 15$ ($\xi = 5$)

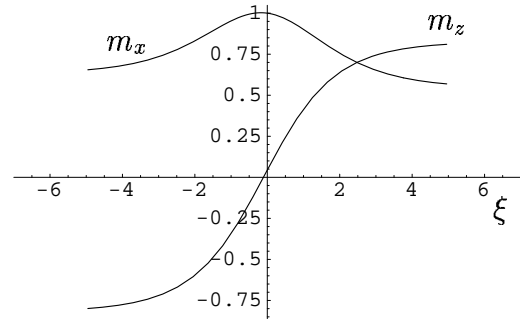


Figure 7.2: Assuming $\Gamma = 0$: Spatial variation of m_x and m_z components of the magnetization across a “spin-down” bubble wall. Parameters and limits of integration as Fig. 7.1

The total demagnetizing field $(\overline{m_z})_0 + (\overline{m_z})_1$ for “spin-up” and “spin-down” bubbles is shown in Figure 7.3 for different values of the driving field h . The parameter $K = 5$ has been chosen to permit later comparison with numerical results, and $R = 10$ selected. We see that, even for bubbles with such a “large” radius, the curvature of the bubble wall has a noticeable effect on the demagnetizing field in the probe, particularly for small values of h .

Therefore in what follows bubble and stripe domain walls may be treated together, provided the curvature of the wall $1/R$ is assumed to deliver only a small deviation from the structure of a planar wall. The expressions F and G in (7.3) may then be extended to

$$\begin{aligned}
 F &= -\gamma - h \cosh u \sin \varphi + K \left[\varphi'' + \varphi' \left(\frac{1}{R} - \frac{\xi}{R^2} + \frac{\xi^2}{R^3} \right) - 2 \tanh u u' \varphi' \right] \\
 G &= (\delta - \overline{m_z}) - h \sinh u \cos \varphi + K \tanh u \\
 &\quad + K \left[u'' + u' \left(\frac{1}{R} - \frac{\xi}{R^2} + \frac{\xi^2}{R^3} \right) - \tanh u ((u')^2 - (\varphi')^2) \right]
 \end{aligned} \tag{7.17}$$

For completeness, expressions (7.17) have been written down including the third term in expansion (7.14) and hence are accurate to $O(\xi^3/R^4)$. The set of equations of motion (7.2) with (7.17) describe cylindrically symmetric domain-type structures when the independent Cartesian coordinate ξ is allowed to roam only close to the the radius of the structure, but still completely covers the entire domain wall, as stated in (7.13). It can also be used to describe planar structures by setting $R = \infty$.

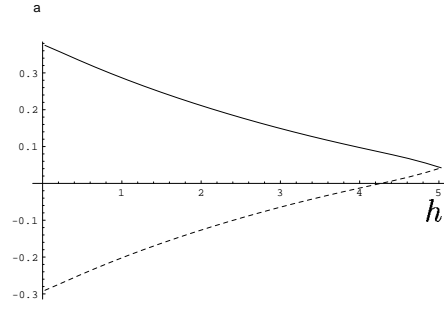


Figure 7.3: Demagnetizing field in “spin-down” bubble domains (full line) and “spin-up” bubble domains (dashed line). Results calculated from linearized equation (7.15) with $R = 10$

7.3 Approximate Wall Solution for $\Gamma \ll 1$

We recall that the work in the last two sections was performed with the condition $\gamma = 0$. Although, as mentioned already, there is no simple way to determine a full steady state solution to (7.2) with (7.17), the solution with $\gamma = 0$ is still a good starting point if we consider the damping Γ to be much smaller than one, and hence treat the case $\gamma \neq 0$ by means of a perturbation calculation.

We assume the new solution has the form:

$$\begin{aligned} u &= u_{\Gamma=0}(\xi) + u_1(\xi) \\ \varphi &= \varphi_1(\xi) \end{aligned} \quad (7.18)$$

where $u_{\Gamma=0}$ is the solution (7.8), $\varphi_0 \equiv 0$ also corresponding to the planar, no-damping case $\Gamma = 0, R = \infty$. The quantities u_1 and φ_1 are assumed to be much smaller than one.

We insert (7.18) into (7.17) and expand the expressions F and G in the small quantities $\Gamma, 1/R, u_1$ and φ_1 :

$$\begin{aligned} F &= F_0 + F_1 + \dots \\ G &= G_0 + G_1 + \dots \end{aligned}$$

Again, steady state solutions must satisfy $F = 0$ and $G = 0$ in each order of the expansion. To zeroth order we obtain:

$$\begin{aligned} F_0 &= 0 \\ G_0 &= (\delta - (\overline{m}_z)_0) - h \sinh u_0 + K \tanh u_0 + K [u_0'' - \tanh u_0 (u_0')^2] = 0 \end{aligned} \quad (7.19)$$

To zeroth order F_0 is identically zero for $\varphi_0 = 0$, while the lower equation in (7.19) is indeed the defining equation for u_0 (7.8) when the equilibrium condition in zeroth order $(\overline{m}_z)_0 = \delta$ is satisfied.

To first order in Γ , $1/R$, u_1 and φ_1 , we obtain two linear equations for u_1 and φ_1 :

$$F_1 = K [\varphi_1'' + 2 \tanh u_0 u_0' \varphi_1'] - h \cosh u_0 \varphi_1 - \gamma = 0 \quad (7.20a)$$

$$G_1 = -(\overline{m}_z)_1 + K \left[u_1'' - 2u_0' \tanh u_0 u_1' - \left(\operatorname{sech}^2 u_0 ((u_0')^2 - 1) + \frac{h}{K} \cosh u_0 \right) u_1 + \frac{u_0'}{R} \right] = 0 \quad (7.20b)$$

After carrying out the transformation $\varphi_1 = \cosh u_0 \widehat{\varphi}_1$, equation (7.20a) becomes

$$K \widehat{\varphi}_1'' - \left[h \operatorname{sech} u_0 + K(1 - 2 \tanh^2 u_0) + \frac{h^2}{K} \right] \widehat{\varphi}_1 = \gamma \operatorname{sech} u_0 \quad (7.21)$$

This is a linear second order inhomogeneous ordinary differential equation with non-constant coefficients. The boundary conditions are also non-zero. From (6.15) we obtain

$$\widehat{\varphi}_1(\xi = \pm\infty) = m_y(\xi = \pm\infty) = -\gamma h / K^2$$

to linear order in Γ . Equation (7.21) can be solved numerically for $\widehat{\varphi}_1(\xi)$. The boundaries are taken at a distance much larger than the width of the wall which is of the order of magnitude 1.

In the planar case ($R = \infty$), equation (7.20b) with $(\overline{m}_z)_1 = 0$ is a linear *homogeneous* second-order differential equation with non-constant coefficient. We note from equation (6.14) that there is no contribution in linear order in Γ (or γ) to $m_z(\xi = \pm\infty)$ (far away from the wall) and so at this order $u = u_0$. Hence $u_1(\xi = \pm\infty) = 0$ at a great distance from the wall (*homogeneous* boundary conditions). Therefore the solution to equation (7.20b) for planar walls is

$$u_1(\xi) \equiv 0 \quad \text{for all } \xi \quad . \quad (7.22)$$

For cylindrical walls, equation (7.20b) is the same equation (7.15) solved numerically for $u_1(\xi)$ in Section 7.2, with $(\overline{m}_z)_1$ as given in (7.16).

Therefore, to linear order in the small quantities $\widehat{\varphi}_1$ and u_1 , the magnetization through the probe when a small damping factor $\Gamma \ll 1$ is taken into account is

$$\begin{aligned} m_x &= \operatorname{sech} u_0 - u_1 \operatorname{sech} u_0 \tanh u_0 \\ m_y &= \widehat{\varphi}_1 \\ m_z &= \tanh u_0 + u_1 \operatorname{sech}^2 u_0 \end{aligned} \quad (7.23)$$

Figure 7.4 shows the components of the magnetization from equation (7.23) for a planar domain wall, using the parameter $K = 5$.

Although the plot on the right for $h = 3$ appears reasonable, for values of the driving field amplitude much less than one (as shown on the left), the results

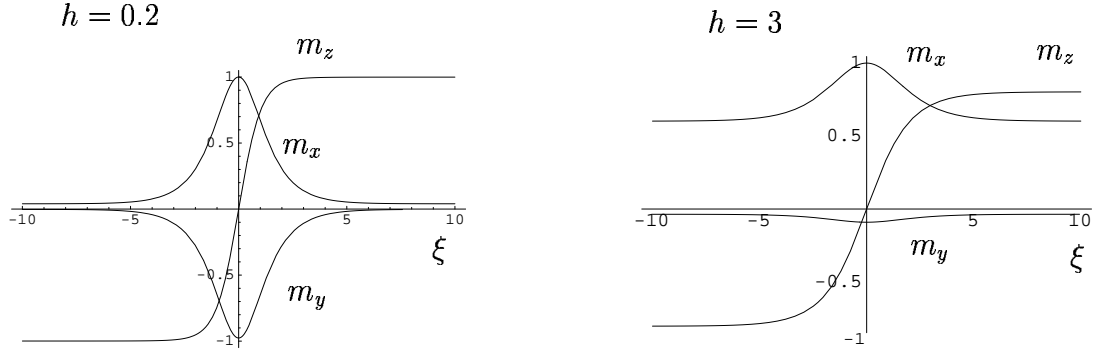


Figure 7.4: Assuming $\Gamma \ll 1$: Spatial variation of m_x and m_z components of the magnetization across a planar domain wall for the case $h = 0.2$ and $h = 3$. ξ is the direction normal to the plane of the wall

are wholly incompatible with the requirement that $|\mathbf{m}| = 1$. The origin of the problem is as follows: From (7.23) to linear order in the small quantities

$$|\mathbf{m}|^2 = 1 + \hat{\varphi}_1^2 + \theta_1^2 = 1 + \text{higher order terms}$$

We see from Figure 7.4 that for the case $h = 0.2$, at the center of the wall $|\mathbf{m}|^2 = m_x^2 + m_y^2 + m_z^2 \approx 2$. In particular, the $\hat{\varphi}_1$ is no longer a small quantity whose square and higher powers can be safely neglected. This is an indication that the simple perturbation calculation performed in this section has broken down, i.e. that the solution perturbed by the small quantity Γ is no longer similar to the solution for $\Gamma = 0$ in the region $h \ll 1$. Only a more sophisticated perturbation calculation will be able to deal with these difficulties, and this will be discussed in the next chapter.

Chapter 8

A Stability Criterion for Dynamic Domains

In the last chapter we succeeded in determining the structure of the wall between dynamic domains, for both the planar and cylindrical cases, by a perturbation calculation in Γ , the damping. However this perturbation calculation broke down for small values of the driving field $h \ll 1$, precisely where, motivated by numerical results, we had hoped to find the lower bound for dynamic domains h_{c3} . In this chapter a more sophisticated perturbation calculation for $h \ll 1$ and $\Gamma \ll 1$ is introduced to attempt to understand better this region of parameter space.

8.1 Comparison with Undriven System

We consider the Landau-Lifshitz equation in the *lab* frame (2.1). The effective field now includes neither the static field H nor the driving field h :

$$\mathbf{h}_{\text{eff}} = K \nabla^2 \mathbf{m} - \bar{m}_z \mathbf{e}_z + K m_z \mathbf{e}_z \quad ,$$

where, as in Chapter 7, we have again scaled the spatial coordinate ξ so that $J = K$. When ξ is strictly a Cartesian coordinate, using the parameterization in (7.1), the Landau-Lifshitz equation has the form

$$\begin{aligned} \dot{u} &= -\tilde{F} + \Gamma \tilde{G} \\ \dot{\varphi} &= \Gamma \tilde{F} + \tilde{G} \end{aligned} \tag{8.1}$$

where

$$\begin{aligned} \tilde{F} &= K [\varphi'' - 2 \tanh u u' \varphi'] \\ \tilde{G} &= -\bar{m}_z + K \tanh u + K [u'' - \tanh u ((u')^2 - (\varphi')^2)] \end{aligned} \tag{8.2}$$

The planar Bloch wall solution satisfies this equation of motion, and this is static when the equilibrium condition $\overline{m}_z = 0$ is satisfied (see Appendix C). The Bloch wall solution is simply:

$$u = \pm\xi \quad , \quad \varphi = \varphi_c = \text{const}$$

where the rotational symmetry of the equations of motion about the z -axis when there is no driving field means that the constant angle φ_c cannot be fixed. The signs (\pm) refer to differently orientated walls.

Now comparing F and G from (7.17) with \tilde{F} and \tilde{G} respectively from (8.2), we see that it might be expected that the equations of motion (7.2) and (8.1) deliver similar solutions when the following four quantities are small, i.e. when:

$$h \ll 1 \quad , \quad \gamma \ll 1 \quad , \quad \delta \ll 1 \quad , \quad \frac{1}{R} \ll 1 \quad (8.3)$$

Thus our calculation will be valid for small values of the driving field. Already we know γ is small as the damping Γ is assumed to be small (just as in Chapter 7); δ is small because we consider only solutions near resonance (in this dimensionless calculation, resonance implies $H = \omega$); and $\frac{1}{R}$ is identically zero for planar domains walls and small for cylindrical domain walls with low curvature, as discussed in Section 7.2. Formally we may identify the four parameters in (8.3) as being of order of magnitude of a smallness parameter ε .

8.2 Linearized Equations of Motion

We now look for solutions to (7.2) with (7.3) of the form

$$\begin{aligned} u &= u_0(\xi, t) + u_1(\xi, t) + u_2(\xi, t) + \dots \\ \varphi &= \varphi_0(\xi, t) + \varphi_1(\xi, t) + \varphi_2(\xi, t) + \dots \end{aligned} \quad (8.4)$$

where $u_i = O(\varepsilon^i)$ and $\varphi_i = O(\varepsilon^i)$.

We insert (8.4) together with (8.3) into the expressions F and G from (7.17) and expand the result as a power series in the smallness parameter ε , yielding

$$\begin{aligned} F &= \tilde{F} + F_1 + F_2 + \dots \\ G &= \tilde{G} + G_1 + G_2 + \dots \end{aligned}$$

where again $F_i = O(\varepsilon^i)$ and $G_i = O(\varepsilon^i)$.

Order ε^0

To order $O(\varepsilon^0)$, \tilde{F} and \tilde{G} are given in (8.2). The solution to zeroth order is therefore

$$\begin{aligned}u_0 &= \pm \xi \\ \varphi_0 &= \varphi_c\end{aligned}$$

as above, and

$$(\overline{m}_z)_0 = 0$$

It is around this solution that we expand the terms of the full expressions for F and G from (7.17).

Order ε^1

To order $O(\varepsilon)$ we obtain:

$$\begin{aligned}F_1 &= K (\varphi_1'' - 2\varphi_1' \tanh \xi) - \gamma - h \cosh \xi \sin \varphi_c \\ G_1 &= K (u_1'' - 2u_1' \tanh \xi) - (\overline{m}_z)_1 + \delta \pm \frac{K}{R} \mp h \sinh \xi \cos \varphi_c\end{aligned}\tag{8.5}$$

Introducing the linear differential operator \mathcal{D} , defined by:

$$\mathcal{D} = -\frac{\partial^2}{\partial \xi^2} + 2 \tanh \xi \frac{\partial}{\partial \xi}\tag{8.6}$$

expressions (8.5) become

$$\begin{aligned}F_1 &= -K \mathcal{D} \varphi_1 - \gamma - h \cosh \xi \sin \varphi_c \\ G_1 &= -K \mathcal{D} u_1 - (\overline{m}_z)_1 + \delta \pm \frac{K}{R} \mp h \sinh \xi \cos \varphi_c\end{aligned}\tag{8.7}$$

Order ε^2

To order $O(\varepsilon^2)$ we obtain:

$$\begin{aligned}F_2 &= K \left(\varphi_2'' - 2\varphi_2' \tanh \xi \mp 2u_1' \varphi_1' \tanh \xi - 2u_1 \varphi_1' \operatorname{sech}^2 \xi + \frac{\varphi_1'}{R} \right) \\ &\quad + h (\mp u_1 \sinh \xi \sin \varphi_c - \varphi_1 \cosh \xi \cos \varphi_c) \\ G_2 &= K (u_2'' - 2u_2' \tanh \xi \mp ((u_1')^2 - (\varphi_1')^2) \tanh \xi + 2u_1 u_1' \operatorname{sech}^2 \xi \\ &\quad + \frac{u_1'}{R} \mp \frac{\xi}{R^2}) - (\overline{m}_z)_2 + h (\pm \varphi_1 \sinh \xi \sin \varphi_c - u_1 \cosh \xi \cos \varphi_c)\end{aligned}\tag{8.8}$$

which similarly become

$$\begin{aligned}
F_2 &= -K\mathcal{D}\varphi_2 + K \left(\mp 2u_1' \varphi_1' \tanh \xi - 2u_1 \varphi_1' \operatorname{sech}^2 \xi + \frac{\varphi_1'}{R} \right) \\
&\quad + h (\mp u_1 \sinh \xi \sin \varphi_c - \varphi_1 \cosh \xi \cos \varphi_c) \\
G_2 &= -K\mathcal{D}u_2 + K \left(\mp ((u_1')^2 - (\varphi_1')^2) \tanh \xi + 2u_1 u_1' \operatorname{sech}^2 \xi \right. \\
&\quad \left. + \frac{u_1'}{R} \mp \frac{\xi}{R^2} \right) - (\overline{m}_z)_2 + h (\pm \varphi_1 \sinh \xi \sin \varphi_c - u_1 \cosh \xi \cos \varphi_c)
\end{aligned} \tag{8.9}$$

Demagnetizing Term

The presence of the terms $(\overline{m}_z)_1$ and $(\overline{m}_z)_2$ in expressions (8.7) and (8.9) above indicates that the demagnetizing field changes when the Bloch solution is perturbed. A change in u causes a change in m_z to the tune of:

$$m_z = \tanh u = \pm \tanh \xi + u_1 \operatorname{sech}^2 \xi + (u_2 \mp u_1^2 \tanh \xi) \operatorname{sech}^2 \xi + O(\varepsilon^3)$$

We assume a system with bounds set at $\xi = \pm L$.¹ The demagnetizing field terms are then given by

$$(\overline{m}_z)_1(t) = \frac{1}{2L} \int_{-L}^L u_1(\xi, t) \operatorname{sech}^2 \xi \, d\xi \tag{8.10}$$

$$(\overline{m}_z)_2(t) = \frac{1}{2L} \int_{-L}^L (u_2(\xi, t) \mp u_1(\xi, t)^2 \tanh \xi) \operatorname{sech}^2 \xi \, d\xi \tag{8.11}$$

The demagnetizing term in each order i is therefore in a functional relationship with u_i and lower order terms, and is a function of t but not of ξ . At the end of the calculation in each order these definitions for the demagnetizing term will be applied so that the calculation is self-consistent.

System of Linear Equations

The equations of motion in each order i are then

$$\begin{aligned}
\dot{u}_i &= -F_i + \Gamma G_i \\
\dot{\varphi}_i &= \Gamma F_i + G_i
\end{aligned} \quad i = 1, 2, \dots$$

In all orders of ε , the equations of motion (a set of two coupled linear inhomogeneous partial differential equations) have the same structure:

$$\begin{pmatrix} \dot{u}_i \\ \dot{\varphi}_i \end{pmatrix} = \underline{\underline{\mathbb{T}}} \begin{pmatrix} u_i \\ \varphi_i \end{pmatrix} + \begin{pmatrix} r_{ui} \\ r_{\varphi i} \end{pmatrix} \quad i = 1, 2, \dots \tag{8.12}$$

¹For the bubble case, treating the curvature of the wall as a perturbation also implies that $L \ll R$ (compare (7.13))

where

$$\underline{\underline{\mathbf{T}}} = \begin{pmatrix} -\Gamma K \mathcal{D} & K \mathcal{D} \\ -K \mathcal{D} & -\Gamma K \mathcal{D} \end{pmatrix} \quad (8.13)$$

For completeness, the inhomogeneous parts of the linear differential equations (8.12) in first and second order in ε are:

$$\begin{aligned} r_{u_1} &= h [\cosh \xi \sin \varphi_c \mp \Gamma \sinh \xi \cos \varphi_c] + \gamma + \Gamma \left(\delta \pm \frac{K}{R} \right) - \Gamma (\overline{m}_z)_1 \\ r_{\varphi_1} &= h [-\Gamma \cosh \xi \sin \varphi_c \mp \sinh \xi \cos \varphi_c] - \Gamma \gamma + \left(\delta \pm \frac{K}{R} \right) - (\overline{m}_z)_1 \end{aligned} \quad (8.14)$$

and

$$\begin{aligned} r_{u_2} &= h [(\pm u_1 \pm \Gamma \varphi_1) \sinh \xi \sin \varphi_c + (\varphi_1 - \Gamma u_1) \cosh \xi \cos \varphi_c] \\ &\quad + K [\pm (2u_1' \varphi_1' - \Gamma ((u_1')^2 - (\varphi_1')^2)) \tanh \xi + (2u_1 \varphi_1' + 2\Gamma u_1 u_1') \operatorname{sech}^2 \xi \\ &\quad - \frac{\varphi_1'}{R} + \Gamma \left(\frac{u_1'}{R} \mp \frac{\xi}{R^2} \right)] - \Gamma (\overline{m}_z)_2 \\ r_{\varphi_2} &= h [\mp (\Gamma u_1 - \varphi_1) \sinh \xi \sin \varphi_c - (\Gamma \varphi_1 + u_1) \cosh \xi \cos \varphi_c] \\ &\quad + K [\mp (2\Gamma u_1' \varphi_1' + ((u_1')^2 - (\varphi_1')^2)) \tanh \xi + (-2\Gamma u_1 \varphi_1' + 2u_1 u_1') \operatorname{sech}^2 \xi \\ &\quad + \Gamma \frac{\varphi_1'}{R} + \left(\frac{u_1'}{R} \mp \frac{\xi}{R^2} \right)] - (\overline{m}_z)_2 \end{aligned} \quad (8.15)$$

General Solution of Homogeneous System

The general solution of the homogeneous part of equation (8.12) can be written down as²:

$$\begin{pmatrix} u_i \\ \varphi_i \end{pmatrix} = \underline{\underline{\mathbf{M}}} \begin{pmatrix} c_1 \\ c_2 \end{pmatrix} \quad (8.16)$$

where

$$\underline{\underline{\mathbf{M}}} = e^{\underline{\underline{\mathbf{T}}}t} = e^{-\Gamma K \mathcal{D}t} \begin{pmatrix} \cos K \mathcal{D}t & \sin K \mathcal{D}t \\ -\sin K \mathcal{D}t & \cos K \mathcal{D}t \end{pmatrix}$$

In particular $\underline{\underline{\mathbf{M}}}$ is the matrix that satisfies

$$\dot{\underline{\underline{\mathbf{M}}}} = \underline{\underline{\mathbf{T}}} \underline{\underline{\mathbf{M}}}$$

Therefore to find the solution of the homogeneous equation (8.16) we need to express the initial conditions c_1 and c_2 in terms of eigenfunctions of \mathcal{D} and so determine how the operator $\underline{\underline{\mathbf{M}}}$ acts on them.

²For simplicity we have suppressed the index i that would normally be attached to the initial conditions c_1 and c_2 in each order

The eigenstates of the operator \mathcal{D} are the solutions to the equation

$$\mathcal{D}\psi_n = E_n\psi_n$$

and are calculated in Appendix D [Helm]. \mathcal{D} has a single uniform localized eigenstate

$$E_0 = 0, \quad \psi_0 = \frac{1}{\sqrt{2}}$$

and a continuous band of spatially dependent states

$$E_k = 1 + k^2$$

$$\psi_k(\xi) = \frac{\cosh \xi (-ik + \tanh \xi) e^{ik\xi}}{\sqrt{1 + k^2}}$$

Then we can expand the initial conditions in the eigenstates ψ_n

$$c_1 = \sum_{n=0,k}^f d_{1n}\psi_n(\xi) \quad , \quad c_2 = \sum_{n=0,k}^f d_{2n}\psi_n(\xi) \quad (8.17)$$

and the solution to equation (8.12) is³

$$u_i(\xi, t) =: \sum_{n=0,k}^f u_{in} = \sum_{n=0,k}^f e^{-\Gamma K E_n t} [C_n d_{1n} + S_n d_{2n}] \psi_n$$

$$\varphi_i(\xi, t) =: \sum_{n=0,k}^f \varphi_{in} = \sum_{n=0,k}^f e^{-\Gamma K E_n t} [-S_n d_{1n} + C_n d_{2n}] \psi_n \quad (8.18)$$

where

$$C_n = \cos K E_n t \quad , \quad S_n = \sin K E_n t \quad (8.19)$$

Solution of Inhomogeneous System

We now approach the full inhomogeneous equation (8.12). First of all we expand the inhomogeneous parts in eigenfunctions of \mathcal{D} :

$$r_{ui}(\xi, t) = \sum_{n=0,k}^f r_{uin}(t)\psi_n(\xi)$$

$$r_{\varphi i}(\xi, t) = \sum_{n=0,k}^f r_{\varphi in}(t)\psi_n(\xi)$$

³The symbol $\sum_{n=0,k}^f$ is used as an abbreviation for summation over the discrete value $n = 0$ and integration over the continuous band $n = k \neq 0$

where

$$r_{uin}(t) = (\psi_k | r_{ui}) \quad \text{and} \quad r_{\varphi in}(t) = (\psi_k | \varphi_{ui}) \quad (8.20)$$

with the inner product $(\cdot | \cdot)$ as defined in (D.1).

Having found the solution of the homogeneous equation in the form (8.18), we can use variation of constants to obtain the full solution to equation (8.12). We allow the coefficients d_{1n} and d_{2n} in (8.17) to be dependent on t . We insert expression (8.18) into the inhomogeneous equation (8.12), compute the time derivatives and cancel out the terms on both sides due to the homogeneous solution. This yields the following expressions for \dot{d}_{1n} and \dot{d}_{2n} :

$$\begin{aligned} \dot{d}_{1n} &= e^{\Gamma K E_n t} [C_n r_{uin} - S_n r_{\varphi in}] \\ \dot{d}_{2n} &= e^{\Gamma K E_n t} [S_n r_{uin} + C_n r_{\varphi in}] \end{aligned}$$

The expressions for \dot{d}_{1n} and \dot{d}_{2n} can then be integrated to obtain d_{1n} and d_{2n} , and these reinserted into (8.18) to yield

$$u_i(\xi, t) = \sum_{n=0,k} u_{in} \quad \text{and} \quad \varphi_i(\xi, t) = \sum_{n=0,k} \varphi_{in}$$

Now it is shown in Appendix D that only the projection of the solution onto the critical eigenspace of \mathcal{D} with $E_0 = 0$ delivers a non-transient solution to (8.12), i.e. for every order $i \geq 1$

$$\left. \begin{aligned} u_{ik}(t \rightarrow \infty) &\rightarrow \text{const} \\ \varphi_{ik}(t \rightarrow \infty) &\rightarrow \text{const} \end{aligned} \right\} \quad \text{for } k \neq 0$$

Therefore we only need calculate the terms d_{10} and d_{20} , that contribute the non-transient parts of the solution of equation (8.12). Because $E_0 = 0$, therefore

$$C_0 = 1 \quad , \quad S_0 = 0$$

and so

$$\dot{d}_{10} = r_{ui0} \quad \text{and} \quad \dot{d}_{20} = r_{\varphi i0}$$

The non-transient parts of the solution in each order i , denoted $u_{i0}(t)$ and $\varphi_{i0}(t)$ are then no longer space-dependent, as they are projections onto the *uniform* critical eigenspace of \mathcal{D} . They are:

$$u_{i0}(t) = d_{10} \psi_0 = \frac{1}{\sqrt{2}} \int r_{ui0}(t) dt \quad (8.21)$$

$$\varphi_{i0}(t) = d_{20} \psi_0 = \frac{1}{\sqrt{2}} \int r_{\varphi i0}(t) dt \quad (8.22)$$

Therefore, to each order i , we need to determine r_{ui0} and $r_{\varphi i0}$ and insert them into (8.21) and (8.22) to find the non-transient solutions u_{i0} and φ_{i0} to that order.

8.3 First Order Solution

Using (8.14) and the definition of the inner product (D.1), the critical parts of the inhomogeneous part of equation (8.12) in first order in ε are⁴

$$\begin{aligned} r_{u10}(t) &= (\psi_0 | r_{u1}) = \frac{1}{\sqrt{2}} \int_{-\infty}^{\infty} r_{u1} \operatorname{sech}^2 \xi \, d\xi \\ &= \frac{h\pi}{\sqrt{2}} \sin \varphi_c + \sqrt{2} \left(\gamma + \Gamma \left(\delta \pm \frac{K}{R} - (\overline{m}_z)_1(t) \right) \right) \\ r_{\varphi10}(t) &= (\psi_0 | r_{\varphi1}) = \frac{1}{\sqrt{2}} \int_{-\infty}^{\infty} r_{\varphi1} \operatorname{sech}^2 \xi \, d\xi \\ &= -\frac{h\pi}{\sqrt{2}} \Gamma \sin \varphi_c + \sqrt{2} \left(-\Gamma \gamma + \delta \pm \frac{K}{R} - (\overline{m}_z)_1(t) \right) \end{aligned}$$

Therefore using formulae (8.21) and (8.22) for $i = 1$ we obtain

$$u_{10}(t) = \left[\frac{h\pi}{2} \sin \varphi_c + \gamma + \Gamma \left(\delta \pm \frac{K}{R} \right) \right] t - \Gamma \int (\overline{m}_z)_1(t) \, dt \quad (8.23)$$

$$\varphi_{10}(t) = \left[-\Gamma \frac{h\pi}{2} \sin \varphi_c - \Gamma \gamma + \delta \pm \frac{K}{R} \right] t - \int (\overline{m}_z)_1(t) \, dt \quad (8.24)$$

The integral terms in (8.23) and (8.24) are dealt with using the definition of $(\overline{m}_z)_1$ in (8.10). As the non-transient part of u_1 is spatially independent, we have

$$(\overline{m}_z)_1(t) = \frac{1}{2L} u_{10}(t) \int_{-L}^L \operatorname{sech}^2 \xi \, d\xi \approx \frac{1}{L} u_{10}(t) \quad (8.25)$$

for sufficiently large L (the probe is assumed large enough to completely contain the domain wall). Inserting this back into (8.23) we have the *self-consistency requirement*

$$u_{10}(t) = \left[\frac{h\pi}{2} \sin \varphi_c + \gamma + \Gamma \left(\delta \pm \frac{K}{R} \right) \right] t - \frac{\Gamma}{L} \int u_{10}(t) \, dt$$

Differentiating with respect to t , we obtain a differential equation that u_{10} must satisfy:

$$\partial_t u_{10}(t) = \frac{h\pi}{2} \sin \varphi_c + \gamma + \Gamma \left(\delta \pm \frac{K}{R} \right) - \frac{\Gamma}{L} u_{10}(t)$$

⁴The following integrals have proved useful in working out the inner products:

$$\int_{-\infty}^{\infty} \operatorname{sech}^2 \xi \, d\xi = 2, \quad \int_{-\infty}^{\infty} \operatorname{sech} \xi \, d\xi = \pi, \quad \int_{-\infty}^{\infty} \operatorname{sech}^2 \xi \sinh \xi \, d\xi = 0$$

This is solved to yield an expression for u_{10} :

$$u_{10}(t) = A_1 e^{-\frac{\Gamma}{L}t} + \frac{L}{\Gamma} \left[\frac{h\pi}{2} \sin \varphi_c + \gamma + \Gamma \left(\delta \pm \frac{K}{R} \right) \right] \quad (8.26)$$

where A_1 is a constant of integration. Thus u_{10} is made up of a transient term that dies away in time and a constant term. We recall that at this stage the constant φ_c is still unknown.

We now turn to the expression for φ_{10} . Inserting $(\overline{m}_z)_1 = u_{10}/L$, with u_{10} from (8.26), into the time integral in (8.24), this becomes:

$$\varphi_{10}(t) = \frac{A_1}{\Gamma} e^{-\frac{\Gamma}{L}t} + A_2 - \frac{1}{\Gamma}(1 + \Gamma^2) \left(\gamma + \frac{h\pi}{2} \sin \varphi_c \right) t \quad (8.27)$$

with A_2 similarly a constant of integration. Thus φ_{10} is made up of a transient part, a constant part, and a part that increases linearly in t . At this stage, this linearly increasing term in the angular component φ_{10} has no effect on the stability of the overall solution to this order as φ is a cyclic coordinate. (8.26) and (8.27) represent the first order alteration to the Bloch solution.

8.4 Second Order Solution

Using (8.15) and the definition of the inner product (D.1), the critical parts of the inhomogeneous part of equation (8.12) in *second* order in ε are⁵

$$\begin{aligned} r_{u20}(t) &= (\psi_0 | r_{u2}) = \frac{1}{\sqrt{2}} \int_{-\infty}^{\infty} r_{u2} \operatorname{sech}^2 \xi \, d\xi \\ &= \frac{h\pi}{\sqrt{2}} \cos \varphi_c (\varphi_{10}(t) - \Gamma u_{10}(t)) - \sqrt{2} \Gamma (\overline{m}_z)_2(t) \end{aligned} \quad (8.28)$$

$$\begin{aligned} r_{\varphi20}(t) &= (\psi_0 | r_{\varphi2}) = \frac{1}{\sqrt{2}} \int_{-\infty}^{\infty} r_{\varphi2} \operatorname{sech}^2 \xi \, d\xi \\ &= \frac{h\pi}{\sqrt{2}} \cos \varphi_c (-\Gamma \varphi_{10}(t) - u_{10}(t)) - \sqrt{2} (\overline{m}_z)_2(t) \end{aligned} \quad (8.29)$$

These expressions for the projection onto the critical eigenspace of the inhomogeneous parts of the second order equation are much more compact than the entire inhomogeneous parts in (8.15), because the non-transient parts of u_1 and φ_1 are

⁵We have made use of the integral:

$$\int_{-\infty}^{\infty} \xi \operatorname{sech}^2 \xi \, d\xi = 0$$

spatially uniform and so all the spatial derivatives of u_1 and φ_1 vanish on carrying out the inner product.

Inserting the first order solutions u_{10} from (8.26) and φ_{10} from (8.27) into $r_{u_{20}}$ in (8.28) we obtain

$$r_{u_{20}}(t) = \sqrt{2}f(t) - \sqrt{2}\Gamma(\overline{m}_z)_2(t) \quad (8.30)$$

where

$$f(t) := \frac{h\pi}{2} \cos \varphi_c \left[\frac{A_1}{\Gamma}(1 - \Gamma^2)e^{-\frac{\Gamma}{L}t} + A_2 - \frac{1 + \Gamma^2}{\Gamma} \left\{ \gamma + \frac{h\pi}{2} \sin \varphi_c \right\} t - L \left(\gamma + \Gamma \left(\delta \pm \frac{K}{R} \right) + \frac{h\pi}{2} \sin \varphi_c \right) \right] \quad (8.31)$$

In order to calculate the second order solution, we have to insert $r_{u_{20}}$ into expression (8.21) for $i = 2$. This yields:

$$u_{20}(t) = \frac{1}{\sqrt{2}} \int r_{u_{20}}(t) dt = \int f(t) dt - \Gamma \int (\overline{m}_z)_2(t) dt \quad (8.32)$$

We recall from (8.11) the definition of the demagnetizing term in second order. Noting that the only non-transient parts of u_1 and u_2 are spatially uniform, $(\overline{m}_z)_2$ becomes:

$$\begin{aligned} (\overline{m}_z)_2(t) &= \frac{1}{2L} u_{20}(t) \int_{-L}^L \operatorname{sech}^2 \xi d\xi \mp \frac{1}{2L} (u_{10}(t))^2 \int_{-L}^L \tanh \xi \operatorname{sech}^2 \xi d\xi \\ &\approx \frac{1}{L} u_{20}(t) \end{aligned} \quad (8.33)$$

again for sufficiently large L . Therefore (8.32) yields the *self-consistency requirement*

$$u_{20}(t) = \int f(t) dt - \frac{\Gamma}{L} \int u_{20}(t) dt$$

which, on differentiation with respect to t , delivers

$$\partial_t u_{20}(t) = f(t) - \frac{\Gamma}{L} u_{20}(t)$$

This may be solved to yield the second order non-transient contribution to u :⁶

$$u_{20}(t) = e^{-\frac{\Gamma}{L}t} \int e^{\frac{\Gamma}{L}t} f(t) dt \quad (8.34)$$

⁶For clarification, this inexact integral is to be understood as an exact integral plus a constant:

$$u_{20}(t) = e^{-\frac{\Gamma}{L}t} \left[\int_0^t e^{\frac{\Gamma}{L}t'} f(t') dt' + \text{const} \right]$$

8.5 Secular Condition

Now, from its definition in (8.31), $f(t)$ is made up of constant terms, exponentially decaying terms, and a term increasing linearly in time t (in curly brackets). When these are inserted into (8.34), the constant and exponentially decaying parts yield again constant and exponentially decaying contributions to u_{20} . However the term that increases linearly in time will also, when integrated to obtain u_{20} , yield a term which increases linearly in time⁷. This would imply a domain wall whose position changes linearly with t along the ξ axis, i.e. an unstable wall solution. This can only be avoided if the term in curly brackets in expression (8.30) vanishes. Hence

$$-\gamma = \frac{h\pi}{2} \sin \varphi_c \quad (8.35)$$

Equation (8.35) is the condition that must be satisfied if a *second order* solution is desired which does not contain terms that increase in time (*secular* terms).

As the field h and the rescaled frequency γ are positive, this means that $\sin \varphi_c$ is certainly negative. For a given γ , not all h can satisfy this requirement. There is a minimum h with which (8.35) can be satisfied. This occurs when $\sin \varphi_c$ is at a minimum, i.e. when $\sin \varphi_c = -1$. Therefore

$$\varphi_{c \min} = \frac{3\pi}{2}$$

So

$$\gamma \leq \frac{h\pi}{2} \quad \text{or} \quad h \geq h_{\min} = \frac{2\gamma}{\pi} \quad (8.36)$$

Expression (8.36) gives a lower bound in h below which no stable dynamic domains can exist and is a stability criterion that is necessary for the existence of dynamic domains.

Final First Order Solution

We now return to the expressions (8.26) and (8.27) and make use of the secular condition (8.35) to write down the solutions to order ε . We have:

$$\begin{aligned} u_{10}(t) &= A_1 e^{-\frac{\Gamma}{L}t} + L \left(\delta \pm \frac{K}{R} \right) \\ \varphi_{10}(t) &= \frac{A_1}{\Gamma} e^{-\frac{\Gamma}{L}t} + A_2 \end{aligned} \quad (8.37)$$

⁷because

$$e^{-\frac{\Gamma}{L}t} \int e^{\frac{\Gamma}{L}t} t dt = -\frac{L^2}{\Gamma^2} + \frac{L}{\Gamma}t + \text{const} \cdot e^{-\frac{\Gamma}{L}t}$$

Therefore, after the transient terms have died away (as $t \rightarrow \infty$):

$$u_{10} = L \left(\delta \pm \frac{K}{R} \right) \quad , \quad \varphi_{10} = A_2$$

Now A_2 is a constant of integration of order ε which currently cannot be determined. The value of A_2 will be delivered by the requirement that a higher order secular term vanish. In fact it is this demand on a *third order* secular term that yields:

$$A_2 = 0$$

The calculation to third order is tedious and, beyond determining the value of A_2 , offers no new insights. It is carried out in Appendix E.

Thus u and φ to first order in the smallness parameter ε are

$$u = u_0 + u_{10} = \pm \xi + L \left(\delta \pm \frac{K}{R} \right) \quad (8.38)$$

$$\varphi = \varphi_c = \arcsin \left(-\frac{2\gamma}{h\pi} \right) \quad (8.39)$$

Therefore, recalling the definitions of u and φ from (7.1), \mathbf{m} to first order in ε may be written as

$$\begin{aligned} m_x &= \cos \varphi_c (\operatorname{sech} u_0 - u_{10} \operatorname{sech} u_0 \tanh u_0) \\ &= \sqrt{1 - \frac{4\gamma^2}{h^2\pi^2}} \left(\operatorname{sech} \xi + L \left(\mp \delta - \frac{K}{R} \right) \operatorname{sech} \xi \tanh \xi \right) \\ m_y &= \sin \varphi_c (\operatorname{sech} u_0 - u_{10} \operatorname{sech} u_0 \tanh u_0) \\ &= -\frac{2\gamma}{h\pi} \left(\operatorname{sech} \xi + L \left(\mp \delta - \frac{K}{R} \right) \operatorname{sech} \xi \tanh \xi \right) \\ m_z &= \tanh u_0 + u_{10} \operatorname{sech}^2 u_0 \\ &= \pm \tanh \xi + L \left(\delta \pm \frac{K}{R} \right) \operatorname{sech}^2 \xi \end{aligned} \quad (8.40)$$

Plots of \mathbf{m} from (8.40) are shown in Figure 8.1 for the planar wall case and in Figure 8.2 for the “spin-up” bubble case. The driving field was selected as $h = 0.2$. In the bubble case we selected $R = 10L$. We see very little difference in the wall structure for these two cases. The center of the wall has shifted by the small amount u_{10} and this is different for bubbles and for stripes. Likewise, the magnetization at the center of the wall is slightly differently orientated. Figure 9.4 shows plots for the case of a planar wall for many different values of h .

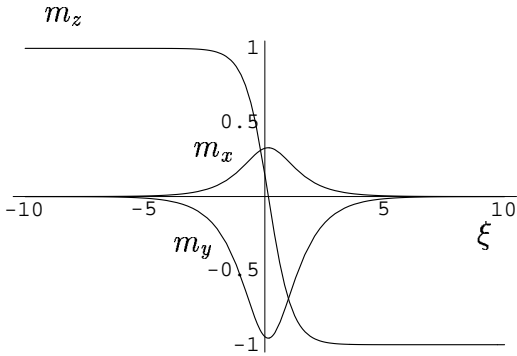


Figure 8.1: The components of magnetization in the planar domain wall

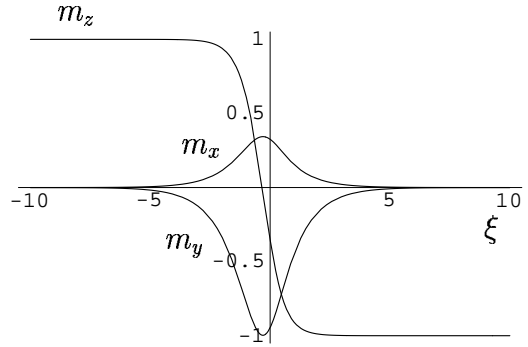


Figure 8.2: The components of magnetization in the “spin-up” bubble wall

Finally we consider the change in the demagnetizing field \bar{m}_z . Using (8.25) we have

$$\begin{aligned}\bar{m}_z &= (\bar{m}_z)_0 + (\bar{m}_z)_1 \\ &= 0 + \frac{u_{10}}{L} = \delta \pm \frac{K}{R}\end{aligned}\tag{8.41}$$

For planar domains ($R = \infty$), this is again merely the requirement that the effective static field in the z direction in the rotating reference frame be equal to the demagnetizing field. Again we see that the equilibrium condition differs somewhat for stripes and bubbles, and that the demagnetizing field in the probe when a cylindrical structure is present is positive for “spin-down” bubbles and negative for “spin-up” bubbles.

The calculation performed in this chapter may be thought of as follows: in the static domain case when a saturating static field in the z direction is applied, the Bloch walls travel through the probe and collide, leaving a magnetic film in the homogeneous $+\mathbf{e}_z$ state (see Appendix C). However, if a sufficiently large resonant transverse driving field is also applied to the film, this movement of the walls can be brought up short and a so-called saturated probe (in the sense that the static field in the z direction is larger than the saturation magnetization of the probe) will remain in a dynamically stable domain state.

To conclude, in this chapter we investigated the parameter region $h \ll 1$ and $\Gamma \ll 1$. This involved linearizing the equations of motion around the static Bloch wall solution to the undriven system. We were able to determine a stability criterion for dynamic domains, the position of the wall in equilibrium and the orientation of the spins within the wall. However, it remains to be seen to what degree these results are useful, i.e. how large the region in parameter space is in which these results correctly represent the behavior of the probe. In the following chapter we present a comparison between the numerical results and the

analytical results. In particular, we determine the regions in parameter space where the semi-analytical wall result developed in Chapter 7 is valid and where the analytical wall results developed in this chapter holds.

Chapter 9

Comparison of Results

Throughout this work, various solutions of the Landau-Lifshitz equation have been determined in various different manners. In Chapter 4 the results from numerical simulations were presented. These will now be compared to the homogeneous solution and linear stability analysis in Chapter 5, to the results for the magnetization far from the domain wall and linear stability analysis in Chapter 6, and to the approximate solutions in Chapters 7 and 8. The critical driving fields determined numerically and analytically are summarized in Table 9.1.

9.1 Homogeneous Solution

In this section we determine compare the results obtained in Chapter 5 to those obtained in the numerical simulations. Firstly a comparison of Figure 5.2 with Figure 4.1 (noting that the same set of parameter values were selected) shows good agreement. These two plots are shown together in Figure 9.1 below.

Moreover the values $h_{c1} = 3.682$ and $h_{c2} = 5.002$, where the homogeneous solution with $m_z > 0$ becomes unstable to non-uniform disturbances, as calculated in Section 5.2 are in agreement with those found in the numerical simulations (Figure 4.9). All that remains is a brief discussion of why fixpoint 4 (the homogeneous solution with $m_z < 0$), although seen here to be stable for $h < h_{c5} = 3.504$, does not appear in simulations. In fact, if we choose initial conditions close enough to the lower branch of the solution curve in Figure 5.1, fixpoint 4 does indeed appear as the final state in the simulation. However with any great variation of these initial conditions from the solution curve, the probe relaxes to fixpoint 1 (or indeed to a dynamical domains state). Thus fixpoint 1 has a greater basin of stability than fixpoint 4. This is an aspect that is not addressed in this linear stability analysis, where only the stability to very small perturbations was investigated.

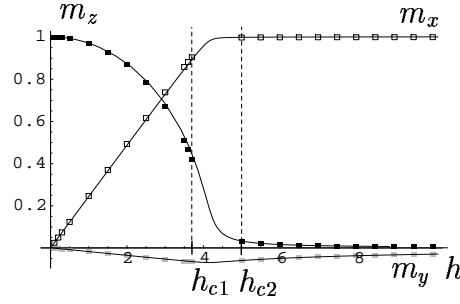


Figure 9.1: Dynamically stable homogeneous states at the parameter values: $J = 10$, $\omega = H = 3$, $K = 5$ for different values of h . The dots show the m_x , m_y and m_z components of the magnetization found numerically, while the solid line shows the results determined analytically

9.2 Domain Features far from the Wall

Section 6.1 yields the magnetization in the domains far from the wall using a simple ansatz. In particular, the z component of the magnetization, plotted in Figure 6.1 compares well with the equivalent numerical results shown in Figure 4.3. These two plots are combined in Figure 9.2 below.

In addition, in this section we determine the upper critical driving field $h_{c4} = 5.0073$ where the domain solution merges into a homogeneous solution. This value may be compared with the rough numerical value of approximately 5.1, with the continuous transition to the homogeneous state in this region indicated in Figure 4.9. Now we noted that for $h < h_{c3} \approx 0.2$ no numerical domain solutions are found. However, there is no indication whatsoever in solution (6.14) of a lower bound. Indeed, in carrying out the numerical calculations, initial conditions arbitrarily close to the known solid line in Figure 9.2 can be chosen, and yet the system always reverts to the homogeneous state in the regime $h < h_{c3}$.

As well as this, equation (6.10) contains a relation for the demagnetizing field $\overline{m}_z = H - \frac{\omega}{1+\Gamma^2} = 0.0297$ for the parameter values used in the numerical simulations. There is good agreement between this value and the constant value of the demagnetizing field $\overline{m}_z \approx 0.03$ determined numerically for stripe domains.

Thus the simple ansatz (6.1) used in this chapter is sufficient to determine accurately the upper bound for the existence of dynamical domain solutions, the magnetization within the domains far from the wall and the demagnetizing field in the probe for stripe domains. Other aspects, such as the lower stability bound seen in the numerical simulations and the differing demagnetizing field for bubbles, cannot be explained using these ideas alone.

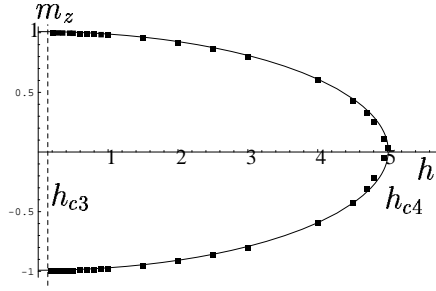


Figure 9.2: The z -component of the magnetization within dynamic domains as obtained from numerical simulations and analytical calculation. Each pair of dots for a given value of h corresponds to the m_z values far from the domain wall for a single numerically stable simulation; the solid lines show the analytical result (6.14)

9.3 Wall Structure

We now compare the results obtained in Chapters 7 and 8, both to each other and to the numerical results in Chapter 4. We recall that in Chapters 7 and 8 we scaled the spatial coordinate ξ such that $\sqrt{\frac{J}{K}} = 1$, whereas in the numerical simulations $K = 5$ and $J = 10$. This must be rescaled in making the comparison.

Chapter 7 considered how to take the wall curvature into account when the radius of the bubble is much greater than the domain wall width. In Figure 9.3 the analytical results calculated from (7.16) are compared to the corresponding numerical results. We see good qualitative agreement between results.

In Chapter 8 we obtained from the secular condition (8.36) a lower bound for domain solutions. With the parameter value $\omega = 3 \Rightarrow \gamma = 0.29703$, this yields a result $h_{\min} = 0.189$. This is in good agreement with the lower bound of $h_{c3} \approx 0.2$ found in the simulations.

Figure 9.4 shows the m_x , m_y and m_z components of the magnetization through a planar domain wall for different values of the driving field h . Close to the lower bound $h_{c3} \approx 0.2$, the calculation from Chapter 8 (right-hand column) compares well with the numerical simulations. However, as h is increased, the comparison becomes less and less favorable. For $h > 0.5$ there is little agreement between the results. Numerically the domains become ever more flattened out, while the theory developed in this chapter which is based on a perturbation of the Bloch solution, pins the z component of the magnetization far from the wall at $m_z = \pm 1$.

In contrast, the theory developed in Chapter 7 agrees well with the numerical simulations for $h \gg h_{c3}$. The flattening out of the domains as h increases to $h_{c4} \approx 5$ is represented well. However, for $h \approx h_{c3}$, the agreement is very poor. In that chapter we discussed how the perturbation calculation broke down for small values of h .

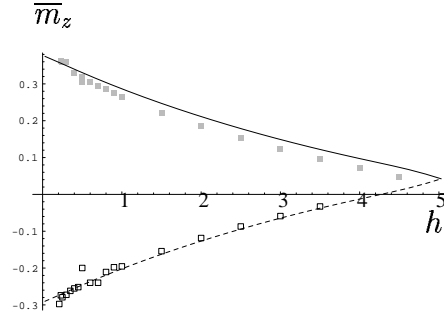


Figure 9.3: Demagnetizing field in bubble dynamic domain states. Each dot corresponds to the final state of a numerical simulations (“spin-down”, gray squares; “spin-up”, open squares) while the lines shows the results calculated from Chapter 7 (“spin-down”, solid line; “spin-up”, dashed line)

Thus the theory developed in Chapter 8 is good for small values of h , while that developed in Chapter 7 is good for larger values of h . There is a region of overlap where both the theories in Chapters 7 and 8 compare well with the numerical simulations. This is in the region of $h \approx 0.5$. Therefore a combination of both methods of calculation can be used to completely describe the structure of the domain wall for all values of h and to explain the structures obtained numerically.

field	numerical	analytical	calculated from
h_{c1}	3.7	3.682	(5.23)
h_{c2}	5	5.002	(5.23)
h_{c3}	0.2	0.189	(6.14)
h_{c4}	5.1	5.0073	(8.36)

Table 9.1: Comparison of critical fields (h_{c1} lower bound of homogeneous solution; h_{c2} upper bound of homogeneous solution; h_{c3} lower bound of domain solution; h_{c4} upper bound of domain solution) determined numerically and analytically

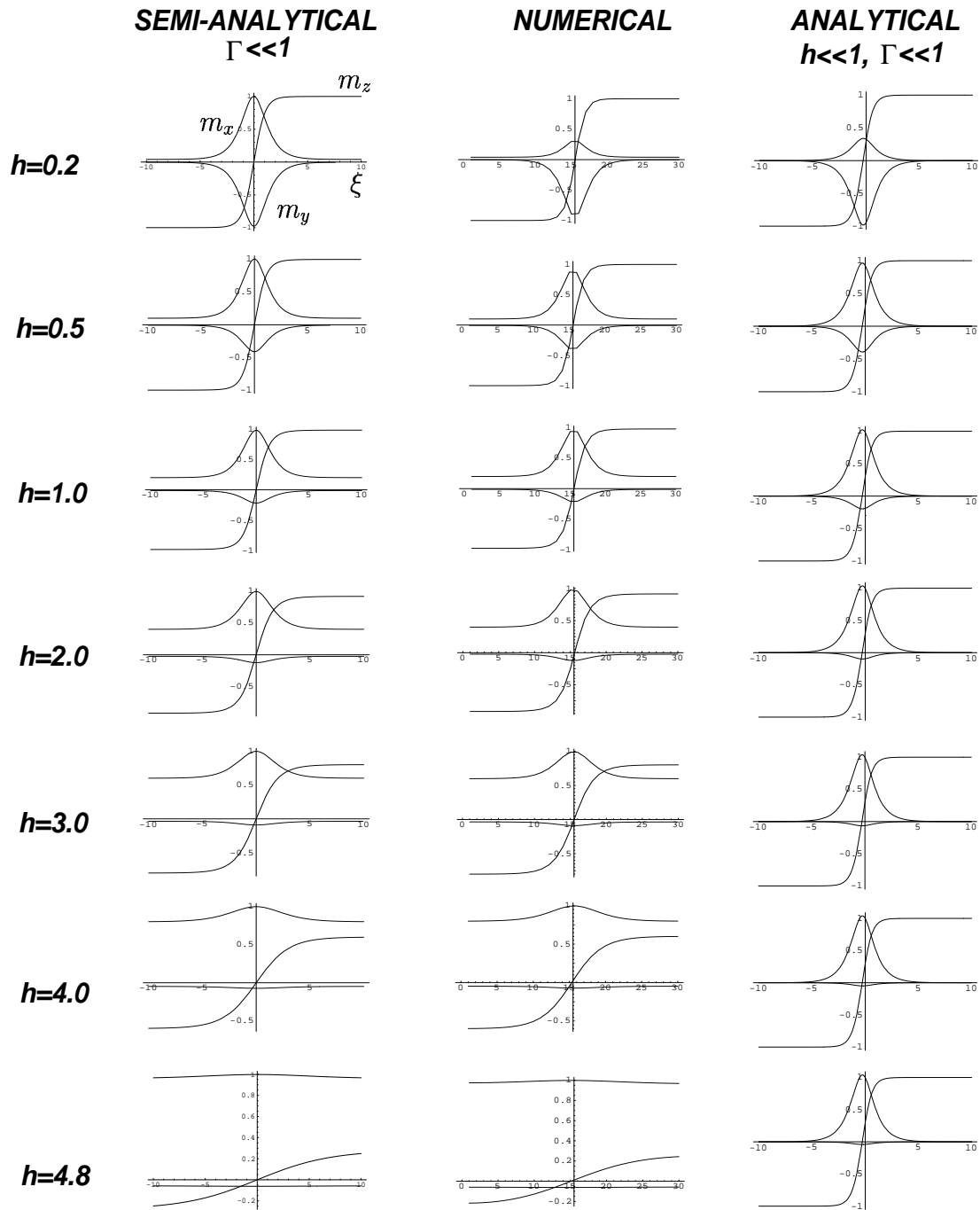


Figure 9.4: Components of magnetization through a planar domain wall.
 Central column: results from numerical simulation, Chapter 4
 Left column: results from perturbation calculation ($\Gamma \ll 1$), Chapter 7
 Right column: results from perturbation calculation ($\Gamma, h \ll 1$), Chapter 8

Chapter 10

Conclusions

In this work we investigated dynamic domains in ferromagnetic films. As a starting point we used the Landau-Lifshitz equation to describe the dynamics of the magnetization in the two-dimensional film. The effective magnetic field in the probe was made of up a static field normal to the plane of the film (in the z direction), a rotating field in the plane of the film, an isotropic exchange field, the demagnetizing part of the dipolar field and a strong anisotropy in the z direction. It was seen that the time-dependent Landau-Lifshitz equation could be transformed to a reference frame rotating with the driving field, yielding a time-independent equation.

The investigation was carried out both numerically and analytically. In Chapter 3 we saw how the numerical investigation was performed using a Fortran program that treated the spatial dependence of the magnetization with spectral methods. The results from the simulation of the time-independent Landau-Lifshitz equation seen to correspond with the stroboscopic view of the results obtained from simulating the time-dependent equation in the lab frame.

In Chapter 4 we looked at the different types of solutions found numerically. It was seen that in large regions of parameter space a homogeneous solution was found, where all spins in the probe rotate in phase about the axis normal to the plane of the film. For small values of the driving field, the magnetization pointed approximately in the z direction, while for larger values of the driving field, the magnetization rotated essentially in the x - y plane.

In addition dynamic domain solutions were found. In this case the probe is made up of two distinct domains in which the spins rotate at two different angles. The domains were observed in only two forms: stripes and bubbles. Within the domains the spins rotate uniformly, while in the wall between the domains there is a continuous transition from one angle of rotation to the next. For small values of the driving field, the magnetization is orientated essentially in the \mathbf{e}_z

or $-\mathbf{e}_z$ directions, and so the domains could be called “spin-up” and “spin-down” domains. As the driving field was increased, the domain structure flattened out, eventually merging back into the homogeneous state.

The structure of the wall was also investigated and it was seen that for a given set of parameter values, the orientation of the magnetization throughout the wall was parallel (see Figure 4.5), and so bubble dynamic domains are not rotationally symmetric.

We also considered the regions of parameter space (varying the amplitude of the driving magnetic field) where the different types of solution were found. It was seen that the homogeneous solution occurs below one critical field amplitude h_{c1} and above another critical field h_{c2} , while domain solutions were found between the critical fields h_{c3} and h_{c4} . Stripe and bubble domain solutions existed between the same boundaries. As $h_{c3} < h_{c1}$ and $h_{c2} < h_{c4}$, there were regions of parameter space where homogeneous, bubble and stripe solutions could all be obtained (bi- or tri-stability), depending on the initial conditions used in the simulation. Two hysteresis loops were observed in the system when the amplitude of the driving field was varied (see Figure 4.9). We were able to investigate numerically the stability of the results of the simulation. Although of course all steady state numerical solutions turned out indeed to be stable according to this investigation, we nevertheless observed that at the critical fields h_{c1} , h_{c2} and h_{c3} , a transition in the stability of the homogeneous and domain solutions appeared to be on the point of occurring. In contrast, there is no indication of a stability transition at the critical field h_{c4} .

In the second part of this work, we investigated the structures observed numerically using analytical methods. Chapter 5 is devoted to the homogeneous solution. Using the requirement that the magnetization be spatially uniform, we were able to reduce the steady-state Landau-Lifshitz equation in the rotating reference frame to a fourth-order polynomial equation for the component of the magnetization in the z direction. This polynomial equation could be solved numerically and it was observed that, depending on the region of parameter space, either two or four solutions were found, and that these regions were separated by a saddle-node bifurcation. In the second part of Chapter 5, we considered the stability of the homogeneous solutions, using a complete linear stability analysis. Because of the demagnetizing term in the equation of motion (an integral term), we had to distinguish between spatially uniform perturbations ($k = 0$) and spatially non-uniform perturbations ($k \neq 0$). It was seen that two of the four homogeneous fixpoints were always unstable to uniform perturbations. The stability of the other two fixpoints to non-uniform perturbations was then investigated. Critical values of the driving field were found where these two fixpoints become unstable for non-uniform perturbations with $k \rightarrow 0$. For the fixpoint with $m_z > 0$, these critical values agreed well with the numerical values h_{c1} and

h_{c2} . The fixpoint with $m_z < 0$ was also seen to be linearly stable below a certain value of the driving field amplitude.

In Chapter 6 we looked at the features of the dynamic domain solution far from the domain wall. Using a simple ansatz that neglected the domain wall, we could reduce the Landau-Lifshitz equation in the rotating reference frame for steady state solutions to a second order polynomial in m_z . These two fixpoints describe the z component of the magnetization in each of the coexisting domains. They merge together at a certain value of the driving field amplitude, and this was seen to coincide with the numerical critical value h_{c4} .

We then considered the stability of this simplified domain structure using a partial linear stability analysis. Both fixpoints were seen to be stable when uniform or non-uniform perturbations were added to the magnetization within the domains. In addition we investigated the effect on the stability of the structure when the position of the wall was shifted. These was also seen to have no effect. We concluded from the work in this chapter that the structure of the domain wall must be taken into account in order to obtain the lower stability bound for dynamic domains.

In Chapter 7 we then looked at the structure of the walls between the dynamic domains. We parameterized the magnetization using two variables u and φ [Helm] and wrote down the Landau-Lifshitz equation with full spatial dependence. We saw that in the limiting case of no damping, the equation defining the steady state was an equation in u only, which could be exactly integrated. This calculation was initially performed for stripe solutions. We then considered the effect of the curvature of the wall in bubble solutions on the no-damping solution. We saw that the curvature of the wall could be treated using a perturbation calculation when the radius of the bubble is assumed much larger than the width of the wall. The results of the perturbation calculation yielded a wall structure only slightly differing from that of the stripe. The greatest effect of the wall curvature was found in the demagnetizing field for “spin-up” and “spin-down” bubbles. From this point onwards we were able to treat both stripe and bubble domains together.

We next considered the domain wall solution including damping, and needed to include the other variable φ in the calculation. Unfortunately there is no general simple method of finding a steady state solution when the magnetization is parameterized by two variables. We treated the damping using a perturbation calculation, linearizing around the no-damping solution obtained earlier and thus were able to reproduce the structure of the domain wall, at least for values of the driving field much larger than zero. For small values of the driving field, not only did we find no indication of a stability threshold h_{c3} expected from numerics, but in fact the perturbation calculation for small damping broke down at that point, as the supposedly higher order quantities took on the same order of magnitude as zeroth order quantities.

In Chapter 8 we continued the search for the lower stability bound for dynamic domain solutions. To this end we compared the equation of motion for small driving field and small damping in the *rotating reference frame* with the Bloch solution for zero driving field in the *lab frame*. We identified three (four) small parameters in the equation of motion for dynamic domains: the driving field, the rescaled frequency, the detuning (and the curvature of the wall). Using a perturbation expansion around the Bloch wall solution, we were able to write down the equation of motion in different orders of the smallness parameter. This led in each order to an inhomogeneous set of linear partial differential equations, containing a differential operator \mathcal{D} . We were then able to write down the solution to these partial differential equations as an expansion in the eigenstates of \mathcal{D} (from Appendix D). It was observed that only one eigenstate of \mathcal{D} makes a non-transient contribution to the solution and that happily this eigenstate is spatially homogeneous. We found that to first order in the smallness parameter, u is constant, while φ increases linearly in time. However, as φ is a cyclic coordinate, this time dependence does not affect the stability of the solution. To *second order* in the smallness parameter, a secular term in u was obtained. In order that the dynamic domain solution could be considered stable, this secular term had to vanish. This led directly to a condition on the amplitude of the driving field which could only be satisfied by a driving field greater than or equal to a certain value. Taking the second order secular condition into account, we could then write down the dynamic domain solution to first order in the smallness parameter, up to a constant that could be determined from the *third order* secular condition.

In Chapter 9 we compared the numerical results (Chapter 4) with the analytic calculations. We saw that the homogeneous solution (Chapter 5), and its critical thresholds h_{c1} and h_{c2} agreed well with numerics. In addition, the calculation in Chapter 6 predicted well the numerical magnetization within the domains and the upper bound h_{c4} where the domains merge together. Finally we compared the numerics with the semi-analytic wall calculation from Chapter 7 and with the analytic wall calculation from Chapter 8 (Figure 9.4). We saw that the calculation from Chapter 8 compared well with the numerics for small values of the driving field amplitude, while Chapter 7 described the region for larger values well. Moreover it was seen that these two solution types overlapped, and together described the numerical dynamic domain solution well. The calculation in Chapter 8 yielded a lower critical threshold h_{c3} for domains.

In conclusion, in this work we found dynamic domain solutions to the Landau-Lifshitz equation above a certain critical value of the driving field. These then then merged into a homogeneous state as the driving field was increased further. The magnetization within the individual dynamic domains is large and rotates about axes oriented in opposite directions. Dynamic domains are a well-defined magnetic structure that seem to represent a solution to the equations of motion in the driven case that is as fundamental as the Bloch solution in the static case.

Appendix A

Numerical Linear Stability Analysis

We assume we have obtained a steady state solution of (2.5), called \mathbf{m}_0 . This may be a solution that has been obtained by numerical simulation from Chapter 4 or by analytical calculation. It may be a homogeneous solution $\mathbf{m}_0 = \text{const}$ or a one-dimensional (planar or cylindrical) domain solution $\mathbf{m}_0 = \mathbf{m}_0(\xi)$. For completeness, we carry the ξ -dependence through this calculation.

In order to investigate the stability of \mathbf{m}_0 we add a small spatially dependent perturbation to it and observe whether it amplifies or decays in time. We consider a magnetization

$$\mathbf{m}(\xi, t) = \mathbf{m}_0(\xi) + \varepsilon \mathbf{m}_1(\xi, t)$$

We insert this into (2.5) and expand in powers of ε . To linear order in ε we obtain

$$-\dot{\mathbf{m}}_1 = B \mathbf{m}_1 \times \mathbf{m}_0 + \Gamma (\mathbf{m}_1 \cdot \mathbf{h}_{\text{eff},0}) \mathbf{m}_1 + (\mathbf{m}_0 \times \mathbf{h}_{\text{eff},1} + \Gamma \mathbf{m}_0 \times (\mathbf{m}_0 \times \mathbf{h}_{\text{eff},1})) \quad (\text{A.1})$$

where

$$B = (\mathbf{m}_0 \cdot \mathbf{h}_{\text{eff},0}) - \omega m_{z,0}$$

and the effective magnetic fields to zeroth and first order in ε are:

$$\begin{aligned} \mathbf{h}_{\text{eff},0} &= h \mathbf{e}_x + (H - \bar{m}_{z,0}) \mathbf{e}_z + K m_{z,0} \mathbf{e}_z + J \mathbf{m}_0'' \\ \mathbf{h}_{\text{eff},1} &= K m_{z,1} \mathbf{e}_z + J \mathbf{m}_1'' \end{aligned}$$

(This linearization of the equation of motion is carried out in more detail for the homogeneous solution in Chapter 5 and for the domain solution in Chapter 6, but the principle here is the same.)

We now introduce a local coordinate system

$$\begin{aligned}
\mathbf{e}_1 &= \mathbf{m}_0 \\
\mathbf{e}_2 &= \mathbf{m}_0 \times \mathbf{e}_z \\
\mathbf{e}_3 &= \mathbf{m}_0 \times (\mathbf{m}_0 \times \mathbf{e}_z)
\end{aligned} \tag{A.2}$$

In this coordinate system the linearized equation of motion (A.1) has the form:

$$\begin{aligned}
-\dot{\beta}\mathbf{e}_2 - \dot{\gamma}\mathbf{e}_3 &= B(-\beta\mathbf{e}_3 + \gamma\mathbf{e}_2) + \Gamma(\mathbf{m}_0 \cdot \mathbf{h}_{\text{eff},0})(\beta\mathbf{e}_2 + \gamma\mathbf{e}_3) + \\
&K(m_{z,0}^2 - 1)\gamma(\mathbf{e}_2 + \Gamma\mathbf{e}_3) + J\mathbf{e}_1 \times (\mathbf{m}_1'' + \Gamma\mathbf{e}_1 \times \mathbf{m}_1'')
\end{aligned} \tag{A.3}$$

where we have used the orthogonality of the vectors in (A.2) and the fact that $m_{z,1} = \mathbf{m}_1 \cdot \mathbf{e}_z = \gamma(m_{z,0}^2 - 1)$.

The final term in (A.3) containing terms with \mathbf{m}_1'' representing the exchange interaction needs further consideration. In particular we must consider the spatial dependence of the unit vectors themselves. We have

$$\begin{aligned}
(\beta\mathbf{e}_2)'' &= \beta''\mathbf{e}_2 + 2\beta'\mathbf{e}_2' + \beta\mathbf{e}_2'' \\
(\gamma\mathbf{e}_3)'' &= \gamma''\mathbf{e}_3 + 2\gamma'\mathbf{e}_3' + \gamma\mathbf{e}_3''
\end{aligned} \tag{A.4}$$

The derivatives the unit vectors (A.2) are

$$\begin{aligned}
\mathbf{e}_2' &= \mathbf{m}_0' \times \mathbf{e}_z \\
\mathbf{e}_2'' &= \mathbf{m}_0'' \times \mathbf{e}_z \\
\mathbf{e}_3' &= m_{0z}'\mathbf{m}_0 + m_{0z}\mathbf{m}_0' \\
\mathbf{e}_3'' &= m_{0z}''\mathbf{m}_0 + m_{0z}\mathbf{m}_0'' + 2m_{0z}'\mathbf{m}_0'
\end{aligned} \tag{A.5}$$

Inserting $\mathbf{m}_0 = m_{x,0}\mathbf{e}_x + m_{y,0}\mathbf{e}_y + m_{z,0}\mathbf{e}_z$ and its derivatives into (A.5), and using the inverse transformation to (A.2) to write the $(\mathbf{e}_x, \mathbf{e}_y, \mathbf{e}_z)$ as $(\mathbf{e}_1, \mathbf{e}_2, \mathbf{e}_3)$ again, we obtain the required expressions in the form

$$\begin{aligned}
(\beta\mathbf{e}_2)'' &= \sum_{i=0}^2 \sum_{j=1}^3 b_{ij}(\beta)^{(i)}\mathbf{e}_j \\
(\gamma\mathbf{e}_3)'' &= \sum_{i=0}^2 \sum_{j=1}^3 c_{ij}(\gamma)^{(i)}\mathbf{e}_j
\end{aligned}$$

The first index of the coefficients b_{ij} and c_{ij} indicates the order of the derivative of β or γ in front of which it appears; the second index j indicates the direction \mathbf{e}_j in which the contribution is made. The coefficients b_{ij} and c_{ij} are dependent on the components of \mathbf{m}_0 and their spatial derivatives. Some of the b_{ij} and c_{ij} are easy to write down. For example, from (A.4), it is clear that the only contribution

containing the second derivative of β is in the \mathbf{e}_2 direction. Hence $b_{21} = b_{23} = 0$ and $b_{22} = 1$. Similarly $c_{21} = c_{22} = 0$ and $c_{23} = 1$.

Because of the particular choice of vector products in equation (A.3), expressions in the direction \mathbf{e}_1 need not be calculated, i.e. we do not need the coefficients $b_{i,1}$ and $c_{i,1}$. The remaining eight coefficients are:

$$\begin{aligned}
b_{02} &= \frac{1}{1 - m_{0z}^2} (m_{0x} m_{0x}'' + m_{0y} m_{0y}'') \\
b_{12} &= \frac{1}{1 - m_{0z}^2} (-2m_{0z} m_{0z}') \\
b_{03} &= \frac{m_{0z}}{1 - m_{0z}^2} (-m_{0y} m_{0x}'' + m_{0x} m_{0y}'') \\
b_{13} &= \frac{m_{0z}}{1 - m_{0z}^2} (-2m_{0y} m_{0x}' + 2m_{0x} m_{0y}')
\end{aligned} \tag{A.6}$$

$$\begin{aligned}
c_{02} &= \frac{1}{1 - m_{0z}^2} (2m_{0z}' (m_{0y} m_{0x}' - m_{0x} m_{0y}') + m_{0z} (m_{0y} m_{0x}'' - m_{0y} m_{0y}'')) \\
c_{12} &= \frac{2m_{0z}}{1 - m_{0z}^2} (m_{0y} m_{0x}' - m_{0x} m_{0y}') \\
c_{03} &= \frac{1}{1 - m_{0z}^2} (m_{0z}^2 (m_{0x} m_{0x}'' + m_{0y} m_{0y}'' + m_{0z} m_{0z}'') - 2m_{0z}'^2 - m_{0z} m_{0z}'') \\
c_{13} &= \frac{m_{0z}}{1 - m_{0z}^2} (-2m_{0y} m_{0x}' + 2m_{0x} m_{0y}')
\end{aligned} \tag{A.7}$$

Equation (A.3) in component form can therefore be written as two coupled linear differential equations:

$$\begin{aligned}
-\dot{\beta} &= B\gamma + \Gamma(\mathbf{m}_0 \cdot \mathbf{h}_{\text{eff},0})\beta + K(m_{z,0}^2 - 1)\gamma \\
&\quad + J[-(b_{03}\beta + b_{13}\beta') - (c_{03}\gamma + c_{13}\gamma' + \gamma'')] \\
&\quad + \Gamma(-(b_{02}\beta + b_{12}\beta' + \beta'') - (c_{02}\gamma + c_{12}\gamma'))] \\
-\dot{\gamma} &= -B\beta + \Gamma(\mathbf{m}_0 \cdot \mathbf{h}_{\text{eff},0})\gamma + \Gamma K(m_{z,0}^2 - 1)\gamma \\
&\quad + J[(b_{02}\beta + b_{12}\beta' + \beta'') + (c_{02}\gamma + c_{12}\gamma')] \\
&\quad + \Gamma(-(b_{03}\beta + b_{13}\beta') - (c_{03}\gamma + c_{13}\gamma' + \gamma''))]
\end{aligned} \tag{A.8}$$

Now we recall that \mathbf{m}_0 is defined on a grid with n points. Writing the derivatives of β and γ as central finite difference expressions (taking note of the periodic boundary conditions), equation (A.8) may be written as $2n$ coupled algebraic equations in the form:

$$\begin{pmatrix} \dot{\beta} \\ \dot{\gamma} \end{pmatrix} = \underline{\underline{L}} \begin{pmatrix} \beta \\ \gamma \end{pmatrix} \tag{A.9}$$

where β and γ are vectors of length n and $\underline{\underline{L}}$ is a matrix of dimensions $2n \times 2n$.

Appendix B

Evaluation of Integrals

In determining the effect of a shift in the domain wall position on the stability of the domain solution in Section 6.2, the linearized Landau-Lifshitz equation (5.14), with the demagnetizing field (6.24), is integrated over a small section of the probe containing the discontinuous wall. We apply the integral (6.26) to each of the terms in (5.14) and obtain:

$$\lim_{\bar{\varepsilon} \rightarrow 0} \int_{Lq_0 - \bar{\varepsilon}}^{Lq_0 + \bar{\varepsilon}} \dot{\mathbf{m}}_1 \, d\xi = 2m_{z,0}^{(1)} Lq_1 \mathbf{e}_z$$

$$\lim_{\bar{\varepsilon} \rightarrow 0} \int_{Lq_0 - \bar{\varepsilon}}^{Lq_0 + \bar{\varepsilon}} B \mathbf{m}_1 \times \mathbf{m}_0 \, d\xi = (hm_{x,0} + Km_{z,0}^{(1)2}) Lq_1 \mathbf{m}_0^{(1)} \times \mathbf{m}_0^{(2)}$$

$$\lim_{\bar{\varepsilon} \rightarrow 0} \int_{Lq_0 - \bar{\varepsilon}}^{Lq_0 + \bar{\varepsilon}} (\mathbf{m}_0 \cdot \mathbf{h}_{\text{eff},0}) \mathbf{m}_1 \, d\xi = (hm_{x,0} + Km_{z,0}^{(1)2}) Lq_1 (\mathbf{m}_0^{(1)} - \mathbf{m}_0^{(2)})$$

$$\lim_{\bar{\varepsilon} \rightarrow 0} \int_{Lq_0 - \bar{\varepsilon}}^{Lq_0 + \bar{\varepsilon}} \mathbf{m}_0 \times \mathbf{h}_{\text{eff},1} \, d\xi = Km_{z,0}^{(1)} Lq_1 (\mathbf{m}_0^{(1)} \times \mathbf{e}_z + \mathbf{m}_0^{(2)} \times \mathbf{e}_z)$$

$$\lim_{\bar{\varepsilon} \rightarrow 0} \int_{Lq_0 - \bar{\varepsilon}}^{Lq_0 + \bar{\varepsilon}} \mathbf{m}_0 \times (\mathbf{m}_0 \times \mathbf{h}_{\text{eff},1}) \, d\xi = Km_{z,0}^{(1)} Lq_1 \left(\mathbf{m}_0^{(1)} \times (\mathbf{m}_0^{(1)} \times \mathbf{e}_z) \right. \\ \left. + \mathbf{m}_0^{(2)} \times (\mathbf{m}_0^{(2)} \times \mathbf{e}_z) \right)$$

Appendix C

Bloch Wall Dynamics

We consider the case where $h = 0$, i.e. where there is no driving field, but retain the static field H in the z direction. We parameterize the magnetization \mathbf{m} with polar coordinates [ScWa, Dill]:

$$\begin{aligned}m_x &= \sin \theta \cos \varphi \\m_y &= \sin \theta \sin \varphi \\m_z &= \cos \theta\end{aligned}$$

We consider solutions in one dimension, i.e. $\mathbf{m} = \mathbf{m}(\xi)$. In the *lab* frame, the Landau-Lifshitz equation (2.1) with

$$\mathbf{h}_{\text{eff}} = H\mathbf{e}_z + Km_z\mathbf{e}_z - \bar{m}_z\mathbf{e}_z + J\mathbf{m}''$$

has the form:

$$\begin{aligned}\sin \theta \dot{\varphi} &= \Gamma F + G \\ \dot{\theta} &= F - \Gamma G\end{aligned}\tag{C.1}$$

where

$$\begin{aligned}F &= J [2 \cos \theta \theta' \varphi' + \sin \theta \varphi''] \\ G &= (H - \bar{m}_z) \sin \theta + K \cos \theta \sin \theta + J [\sin \theta \cos \theta (\varphi')^2 - \theta'']\end{aligned}$$

We look for solutions of the form

$$\begin{aligned}\theta &= \theta(\xi - vt) \\ \varphi &= \varphi_c + \Omega t\end{aligned}$$

where v , Ω and φ_c are unknown constants. Then $\dot{\theta} = -v\theta'$ and

$$\begin{aligned}F &= 0 \\ G &= (H - \bar{m}_z) \sin \theta + K \cos \theta \sin \theta - J\theta''\end{aligned}$$

Equations (C.1) have the form

$$\sin \theta \Omega = G \quad (\text{C.2a})$$

$$-v \theta' = -\Gamma G \quad (\text{C.2b})$$

and so

$$\begin{aligned} v \theta' &= \Gamma \Omega \sin \theta \\ \Rightarrow v \theta'' &= \Gamma \Omega \cos \theta \theta' \\ \Rightarrow \theta'' &= \frac{\Gamma^2}{v^2} \Omega^2 \cos \theta \sin \theta \end{aligned}$$

This expression for θ'' is inserted into equation (C.2a), yielding

$$\sin \theta [\Omega - H + \bar{m}_z] = \cos \theta \sin \theta \left[K - J \frac{\Gamma^2}{v^2} \Omega^2 \right] \quad (\text{C.3})$$

Expression (C.3) can only be satisfied for all angles θ if both expressions in square brackets vanish, i.e.

$$\Omega = H_i \quad \text{and} \quad v = \pm \sqrt{\frac{J}{K}} \Gamma H_i$$

$H_i = H - \bar{m}_z$ is the internal field in the z direction the probe. The solution of the undriven Landau-Lifshitz equation when the internal field is zero is the expression for the steady state Bloch wall

$$\theta(\xi) = 2 \arctan e^{\pm \sqrt{\frac{K}{J}} \xi}, \quad \varphi = \varphi_c \quad (\text{C.4})$$

Therefore, when $H \neq \bar{m}_z$, the solution has the form

$$\begin{aligned} \theta(\xi - vt) &= 2 \arctan e^{\left(\pm \sqrt{\frac{K}{J}} \xi - \Gamma H_i t \right)} \\ \varphi &= \varphi_c + H_i t \end{aligned} \quad (\text{C.5})$$

and describes a Bloch wall moving with velocity proportional ΓH_i , while the spins in the wall rotate at a frequency H_i . The wall connecting the $m_z = +1$ domain on the left with the $m_z = -1$ domain on the right (negative sign in exponent in (C.5)) moves to the right and vice versa. Therefore two oppositely orientated walls in a single probe will move towards each other, increasing the amount of the probe in the spin up ($m_z = +1$) state and thus increasing the demagnetizing field \bar{m}_z . Therefore the internal field H_i (and hence the velocity of the walls) becomes ever smaller as the walls approach each other, until they eventually come to a standstill in the time limit $t \rightarrow \infty$. At this point $H = \bar{m}_z$ and the steady state Bloch wall solution (C.4) is found.

However, if H is from the outset larger than the maximum value of $\overline{m}_z = 1$, this equilibrium state can never be reached and the two walls collide, leaving the probe in the homogeneous spin up state. This is the case in the numerical simulations presented here, indicating why a steady state Bloch wall solution is never seen for $h = 0$.

Appendix D

Eigenstates of \mathcal{D} and T

In Chapter 8 we linearize the Landau-Lifshitz equation of motion around the Bloch wall. In doing so we meet the two-dimensional linear operator \underline{T} (8.13) that is defined in terms of a differential operator \mathcal{D} (8.6).

The spectrum and eigenstates of \underline{T} are based on those of \mathcal{D} . Hence we look for solutions of

$$-\psi'' + 2 \tanh \xi \psi' = E\psi$$

or, substituting $\psi(\xi) = \theta(\xi) \cosh \xi$, we can obtain an equation that has been much researched in the literature [Helm]

$$-\theta'' - (2 \operatorname{sech}^2 \xi - 1)\theta = E\theta$$

This has one localized state

$$E_0 = 0, \quad \theta_0(\xi) = \operatorname{sech} \xi / \sqrt{2}$$

and running states

$$E_k = 1 + k^2$$
$$\theta_k(\xi) = [-ik + \tanh \xi] e^{ik\xi} / (1 + k^2)^{1/2}$$

These functions form a complete and orthogonal set as they are eigenfunctions of a self-adjoint operator

$$\int_{-\infty}^{\infty} d\xi \theta_k^*(\xi) \theta_{k'}(\xi) = 2\pi \delta(k - k')$$
$$\int_{-\infty}^{\infty} d\xi \theta_0(\xi) \theta_0(\xi) = 1$$

The eigenfunctions of \mathcal{D} , ψ_n , are:

$$\psi_0 = \frac{1}{\sqrt{2}}$$

$$\psi_{k \neq 0}(\xi) = \cosh \xi [-ik + \tanh \xi] e^{ik\xi} / (1 + k^2)^{1/2}$$

Note that the zero eigenfunction of \mathcal{D} is *not* space dependent. Written in terms of the ψ_n , the orthogonality relations read

$$\int_{-\infty}^{\infty} d\xi \psi_k^*(\xi) \psi_{k'}(\xi) \operatorname{sech}^2 \xi = 2\pi \delta(k - k')$$

$$\int_{-\infty}^{\infty} d\xi \psi_0 \psi_0 \operatorname{sech}^2 \xi = 1$$

With this we can construct an inner product¹

$$(a|b) := \int_{-\infty}^{\infty} d\xi a^* b \operatorname{sech}^2 \xi \quad (\text{D.1})$$

We also wish determine the eigenvalues and right eigenfunctions of $\underline{\mathbb{T}}$:

$$\underline{\mathbb{T}} u_n = \gamma_n u_n$$

we make the ansatz

$$u_n^\pm = \begin{pmatrix} p_n^\pm \psi_n \\ \psi_n \end{pmatrix}$$

Consistency then requires that

$$\gamma_n^\pm = K E_n(-\Gamma \pm i)$$

and

$$p_n^\pm = \mp i$$

Similarly the left eigenfunctions of $\underline{\mathbb{T}}$ are

$$v_n^\pm = (\psi_n^*, p_n^\pm \psi_n^*)$$

It can be easily checked that these eigenfunctions indeed form a complete, orthogonal set under a vectorial version of the inner product (D.1).

¹Strictly speaking, it is only when ξ is truly a Cartesian coordinate that integration with respect to ξ from $-\infty$ to $+\infty$ makes sense. In the case of cylindrical structures, where $\xi = \rho - R$, we should integrate over a stretch that completely encloses the domain wall. However, here, as throughout this work, we assume that the behavior of the probe very far from the domain wall has no effect on the structure of the wall or the stability of the domains.

$\underline{\underline{T}}$ has two discrete eigenvalues $\gamma_0^\pm = 0$ and a continuous band of eigenvalues $\gamma_{k \neq 0}^\pm$. The discrete zero eigenvalues represent the rotational and translational symmetry in the system. We note that $\text{Re}(\gamma_{k \neq 0}^\pm) = -\Gamma K(1 + k^2) < 0$ i.e the continuous band of eigenvalues has negative real parts.

All $\text{Re}(\gamma_n^\pm) \leq 0$. This means that the Bloch solution is stable or marginally stable. It is only the projection of the the solution of equation (8.12) onto the eigenspace of the critical eigenvalues γ_0^\pm which is of interest. All other parts of the solution, projected onto non-critical eigenspaces, deliver only transient terms to the final solution.

Appendix E

Higher Order Secular Condition

In this appendix we continue the calculation in Chapter 8 to higher orders in the smallness parameter ε , in order to determine the constant of integration A_2 that appears to first order in the variable φ .

Using the *second order* secular condition (8.35), we can write down $f(t)$ from (8.31) as

$$f(t) = \frac{h\pi}{2} \cos \varphi_c \left[\frac{A_1}{\Gamma} (1 - \Gamma^2) e^{-\frac{\Gamma}{L}t} + A_2 - L\Gamma \left(\delta \pm \frac{K}{R} \right) \right]$$

Inserting this into the integral (8.32) we obtain

$$u_{20}(t) = \frac{h\pi}{2} \cos \varphi_c \left[\frac{A_1}{\Gamma} (1 - \Gamma^2) e^{-\frac{\Gamma}{L}t} (t + A_3) + \left(A_2 - L\Gamma \left(\delta \pm \frac{K}{R} \right) \right) \left(\frac{L}{\Gamma} + A_4 e^{-\frac{\Gamma}{L}t} \right) \right] \quad (\text{E.1})$$

A_3 and A_4 are two constants of integration. u_{20} is therefore made up of transient terms and constant terms (any terms increasing in t have been explicitly removed by demanding the second order secular condition (8.35)).

To find the second order angular coordinate φ_{20} , we first insert (8.37) into (8.29) and obtain:

$$r_{\varphi_{20}}(t) = -\frac{h\pi}{\sqrt{2}} \cos \varphi_c \left(2A_1 e^{-\frac{\Gamma}{L}t} + \Gamma A_2 + L \left(\delta \pm \frac{K}{R} \right) \right) - \sqrt{2} (\overline{m}_z)_2(t)$$

This is inserted into (8.22) for $i = 2$, yielding

$$\varphi_{20}(t) = \frac{h\pi}{2} \cos \varphi_c \left[\frac{2A_1 L}{\Gamma} e^{-\frac{\Gamma}{L}t} - \Gamma A_2 t - L \left(\delta \pm \frac{K}{R} \right) t \right] - \frac{1}{L} \int u_{20}(t) dt \quad (\text{E.2})$$

The integral in (E.2) is dealt with using (E.1) and we finally obtain:

$$\begin{aligned} \varphi_{20}(t) = & \frac{h\pi}{2} \cos \varphi_c \left\{ \frac{2A_1L}{\Gamma} e^{-\frac{\Gamma}{L}t} + \frac{A_1}{\Gamma} (1 - \Gamma^2) \left(\frac{1}{\Gamma}t + \frac{L}{\Gamma^2} \right) e^{-\frac{\Gamma}{L}t} \right. \\ & \left. + \frac{1}{\Gamma} \left[\frac{A_1A_3}{\Gamma} (1 - \Gamma^2) + A_4 \left(A_2 - L\Gamma \left(\delta \pm \frac{K}{R} \right) \right) \right] e^{-\frac{\Gamma}{L}t} - \frac{1 + \Gamma^2}{\Gamma} A_2 t \right\} + A_5 \end{aligned} \quad (\text{E.3})$$

A_5 is a further constant of integration. $\varphi_{20}(t)$ is made up of transient terms, constant terms and a term increasing linearly in time (underscored). At this order, this term does not cause any problems as φ is a cyclic coordinate. However it is expected to yield a secular term in the next order in ε , i.e. a term linearly increasing in time in u_{30} . This is demonstrated below.

We insert (8.4) together with (8.3) into the expressions F and G from (7.3) and expand the result as a power series in the smallness parameter ε .

Order ε^3

$$\begin{aligned} F_3 = & -h \left[\cosh \xi \left(\varphi_2 \cos \varphi_c - \frac{\varphi_1^2}{2} \sin \varphi_c \right) \pm u_1 \varphi_1 \sinh \xi \cos \varphi_c \right. \\ & \left. + \left(\pm u_2 \sinh \xi + \frac{u_1^2}{2} \cosh \xi \right) \sin \varphi_c \right] + \text{terms involving } \varphi'_1, u'_1, \varphi'_2, u'_2 \\ G_3 = & -h \left[\mp \sinh \xi \left(\varphi_2 \sin \varphi_c + \frac{\varphi_1^2}{2} \cos \varphi_c \right) - u_1 \varphi_1 \cosh \xi \sin \varphi_c \right. \\ & \left. + \left(u_2 \cosh \xi \pm \frac{u_1^2}{2} \sinh \xi \right) \cos \varphi_c \right] - (\overline{m}_z)_3 \pm \frac{K}{R^3} \xi^2 \\ & + \text{terms involving } \varphi'_1, u'_1, \varphi'_2, u'_2 \end{aligned}$$

We are able safely to neglect terms involving spatial derivatives, because we know that the projection onto the critical eigenspace of \mathcal{D} yields *spatially uniform* non-transient parts of the solution. From (8.20) and using the definition of the inner product (D.1)

$$\begin{aligned} r_{u30} &= (\psi_0 | -F_3 + \Gamma G_3) \\ &= \sqrt{2}g(t) - \sqrt{2}\Gamma(\overline{m}_z)_3(t) \end{aligned}$$

where¹

$$g(t) = \frac{h\pi}{2} \left[(\varphi_{20} - \Gamma u_{20}) \cos \varphi_c + \left(-\frac{\varphi_{10}^2}{2} + \frac{u_{10}^2}{2} + \Gamma u_{10} \varphi_{10} \right) \sin \varphi_c \right] \pm \frac{\Gamma}{2} \frac{K}{R^3} \frac{\pi^2}{6}$$

¹We have used the fact that

$$\int_{-\infty}^{\infty} \xi^2 \operatorname{sech}^2 \xi \, d\xi = \frac{\pi^2}{6}$$

As in all other orders of magnitude

$$(\overline{m}_z)_3(t) \approx \frac{1}{L} u_{30}(t)$$

for sufficiently large L . The calculation is therefore completely equivalent to that performed in second order in ε in Section 8.4 and we have

$$u_{30}(t) = e^{-\frac{\Gamma}{L}t} \int e^{\frac{\Gamma}{L}t} g(t) dt$$

As discussed in Section 8.5, constant terms and transient terms in $g(t)$ will only contribute constant and transient terms to $u_{30}(t)$. However a term that increases linearly in time in $g(t)$ will lead to a linearly increasing $u_{30}(t)$. The only source of such a term is the underscored expression in (E.3). Thus, unstable terms in third order in ε can only be avoided for all parameter values if

$$A_2 = 0$$

This is a *third order* secular condition and is needed to write down fully the *first order* solution in Section 8.5.

Inserting $A_2 = 0$ into (E.1) and (E.3) and retaining only non-transient terms we find

$$u_{20}(t \rightarrow \infty) = -\frac{h\pi}{2} \cos \varphi_c L^2 \left(\delta \pm \frac{K}{R} \right)$$

$$\varphi_{20}(t \rightarrow \infty) = A_5$$

These are the steady state solutions in second order in ε . Again A_5 is again an unknown constant of order ε^2 . It may be only determined by considering a *fourth order* secular condition, which would in turn lead to the solutions for u and φ in third order in ε as a function of yet another unknown constant of order ε^3 . This process is repeated in all subsequent orders of ε .

Bibliography

- [Akhi] A. I. Akhiezer, V. G. Bar'yakhtar, S. V. Peletminskii; Spin Waves. North-Holland Publishing Company, Amsterdam (1968) 9, 10
- [Damo] R.W. Damon; Ferromagnetic resonance at high power. In: Magnetism, Vol.I, Editors G.T. Rado, H. Suhl, Academic Press, New York, London (1963) 5
- [deLe] F.H. de Leeuw, R. van den Doel, U. Enz; Dynamic properties of magnetic domain walls and magnetic bubbles. Rep. Prog. Phys. 43, 689 (1980) 5
- [DeBo] W.J. DeBonte; Theory of the static stability of thick-walled cylindrical domains in uniaxial platelets. AIP Conf. Proc. 5, Magnetism and Magnetic Materials (1971) 52
- [Dill] J.F. Dillon, Jr; Domains and domain walls. In: Magnetism, Vol.III, Editors G.T. Rado, H. Suhl, Academic Press, New York, London (1963) 86
- [Doet] H.Dötsch; Dynamics of magnetic domains in microwave fields. J. Mag. Mag. Materials 4, 180 (1977) 5
- [Elme] F.J. Elmer; Spatial pattern formation in FMR – an example for nonlocal dynamics. J. Phys. (Paris) 49, C8-1597 (1988) 5
- [Fles] P. Flesch; Dynamische Domänen in getriebenen Ferromagneten. Diplomarbeit Darmstadt (1997) 5, 37
- [Gara] D.A. Garanin; Generalized equation of motion for a ferromagnet. Physica A 172, 470 (1991) 8
- [Grad] I.S. Gradshteyn, I.M. Ryzhik; Table of Integrals, Series, and Products. Academic Press, New York (1980). 51

- [Helm] J.S. Helman, H.B. Braun, J.S. Broz, W. Baltensperger; General solution of the Landau-Lifshitz-Gilbert equations linearized around a Bloch wall. *Phys. Rev. B* 43, 5908 (1991) [49](#), [50](#), [64](#), [80](#), [89](#)
- [Hube] A. Hubert; *Theorie der Domänenwände in geordneten Medien*. Springer-Verlag, Berlin, Heidelberg (1974) [4](#), [50](#)
- [IvSh] B.A. Ivanov, D.D. Sheka; Two-dimensional magnetic solitons and thermodynamics of quasi-two-dimensional magnets. *Chaos, Solitons & Fractals* 5, 2605 (1995) [5](#), [52](#)
- [Kose] A.M. Kosevich, B.A. Ivanov, A.S. Kovalev; Magnetic Solitons. *Phys. Rep.* 194, 117 (1990) [5](#), [52](#)
- [Laga] M. Lagally; *Vektorrechnung*. Akakademische Verlagsgesellschaft Geest & Portig K.-G., Leipzig, 5th Edition (1956), p. 59 & 248 ff [10](#)
- [LaLi] L.D. Landau, E.M. Lifshitz; On the theory of the dispersion of magnetic permeability in ferromagnetic bodies. *Phys. Z. Sowjet.* 8, 153 (1935) [Reprint in: *Collected Papers of L.D. Landau*; D. ter Haar (editor), Pergamon Press, Oxford (1965)] [8](#)
- [MaSa] F. Matthäus, H. Sauermann; Amplitude equations near pattern forming instabilities for strongly driven ferromagnets, *Z. Phys. B* 99, 611 (1996) [5](#)
- [MaPl] F. Matthäus, T. Plefka; FPDEHBR, a program to numerically integrate the three-dimensional spin equation. Darmstadt (1994, 1996) [13](#)
- [MaSl] A.P. Malozemoff, J.C. Slonczewski; *Magnetic Domains Walls in Bubble Materials*. Academic Press, New York (1979) [4](#)
- [Plef93] T. Plefka; Nonlinear damping in spin systems: long range spin-spin interactions. *Z. Phys. B* 90, 447 (1993) [8](#)
- [Plef95] T. Plefka; Formation of dynamic domains in strongly driven ferromagnets. *Phys. Rev. Lett.* 75, 144 (1995) [5](#)
- [RaWe] G.T. Rado, J.R. Weertman; Spin-wave resonance in a ferromagnetic metal. *J. Phys. Chem. Solids* 11, 315 (1959) [13](#)
- [Rieg] A. Riegert; *Der Einfluß der Dipolarwechselwirkung auf die Nichtgleichgewichtsstrukturbi-ldung in getriebenen ferromagnetischen Filmen*, Dissertation Darmstadt (2001) [5](#)
- [ScWa] N.L. Schryer, L.R. Walker; The motion of 180° domains walls in uniform dc fields. *J. App. Phys.* 45, 5406 (1974) [5](#), [7](#), [86](#)

- [SeAn] M. Seul, D. Andelman; Domain shapes and patterns: the phenomenology of modulated phases. *Science* 267, 476 (1995) 4
- [Slon] J.C.Slonczewski; Theory of Bloch-line and Bloch-wall motion. *J. App. Phys.* 45, 2705 (1974) 5
- [Suhl] H. Suhl; Ferromagnetic resonance at high signal powers. *J. Phys. Chem. Solids* 1, 209 (1957) 5
- [Thie] A.A. Thiele; Excitation Spectrum of Magnetic Domain Walls. *Phys. Rev. B* 7, 391 (1973) 5
- [Völg] H.R. Völger; Instabilitäten und Strukturbildungsprozesse in getriebenen Ferromagneten: Bifurkationsanalyse bei Brechung der Inversionssymmetrie. Dissertation Darmstadt (1999) 5
- [Wige84] P.E. Wigen; Microwave properties of magnetic garnet thin films. *Thin Solid Films* 114, 135 (1984) 5
- [Wige94] P.E. Wigen (Ed.); Nonlinear phenomena and chaos in magnetic materials. World Scientific (1994) 5, 14
- [Wöbe98] T. Wöbbeking, H. Dötsch, A.F.Popkov; Spatial pattern formation in strongly driven ferromagnets. *J. Phys. D* 31, 2751 (1998) 5
- [Wöbe99] T. Wöbbeking; Räumliche solitonartige Strukturbildung bei inhomogener nichtlinearer Anregung der ferrimagnetischen Resonanz in Granatfilmen. Dissertation, Osnabrück (1999) 5
- [Wolf] Wolfram Research, Inc., Mathematica, Version 4, Champaign, IL (1999) 54

Acknowledgements

I wish to thank Prof. Herwig Sauermann for his encouragement and constant interest throughout my research.

The driving force behind this work has been Dr. Timm Plefka. I am extremely grateful for his vast knowledge of solid state physics, his time and his enthusiasm.

I must also thank the group I had the pleasure of working with over the last five years. In particular thank you to Jörg Kugler and Christine Just for their comments on this thesis.

Curriculum Vitae

Katherine Mayes
Liebigstraße 9
64293 Darmstadt

date of birth: 2nd August 1973
in: Dublin, Ireland
marital status: single

Education:	1977–1985	Burrow School (primary school), Dublin
	1983	Hügelschule (primary school), Tübingen
	1985–1991	St. Andrew's College, Dublin
		School Leaving Certificate Examination
	1991–1995	Theoretical Physics, Trinity College, Dublin
		B.A.(Hons.) in Theoretical Physics
	1995–1997	Mathematics, Trinity College, Dublin
		M.Sc. in Mathematics
		(Thesis: Paper Motion in Printing Machines)
	1995–1996	Erasmus Exchange, TU Darmstadt
		Institute of Fluid Mechanics
	1997–1998	DAAD Scholarship
	1998–2000	Graduate Scholarship of the State of Hesse
	from Aug. 2000	Research Assistant at the Institute of Solid State Physics, TU Darmstadt

Erklärung

Ich erkläre hiermit, dass ich die vorliegende Arbeit selbständig und nur unter Verwendung der angegebenen Hilfsmittel angefertigt habe.

Bisher habe ich noch keinen Promotionsversuch unternommen.

Darmstadt, im Dezember 2002